The Astrophysical Journal, 760:127 (36pp), 2012 December 1 doi:10.1088/0004-637X/760/2/127

DEMOGRAPHICS AND PHYSICAL PROPERTIES OF GAS OUTFLOWS/INFLOWS AT $0.4 < z < 1.4$

Crystal L. Martin[1], Alice E. Shapley[2,8], Alison L. Coil[3,9], Katherine A. Kornei[2], Kevin Bundy[4], Benjamin J. Weiner[5], Kai G. Noeske[6], and David Schiminovich[7]
[1] Department of Physics, University of California, Santa Barbara, CA 93106, USA; cmartin@physics.ucsb.edu
[2] Department of Physics and Astronomy, University of California, Los Angeles, CA 90025, USA
[3] Center for Astrophysics and Space Sciences, Department of Physics, University of California, San Diego, CA 92093, USA
[4] Kavli Institute for the Physics and Mathematics of the Universe (Kavli IPMU, WPI), Todai Institutes for Advanced Study, University of Tokyo, Kashiwa 277-8583, Japan
[5] Steward Observatory, 933 N. Cherry St., University of Arizona, Tucson, AZ 85721, USA
[6] Space Telescope Science Institute, Baltimore, MD 21218, USA
[7] Department of Astronomy, Columbia University, New York, NY 10027, USA
Received 2012 June 22; accepted 2012 October 13; published 2012 November 15

ABSTRACT

We present Keck/LRIS spectra of over 200 galaxies with well-determined redshifts between 0.4 and 1.4. We combine new measurements of near-ultraviolet, low-ionization absorption lines with previously measured masses, luminosities, colors, and star formation rates to describe the demographics and properties of galactic flows. Among star-forming galaxies with blue colors, we find a net blueshift of the Fe II absorption greater than 200 km s^{-1} (100 km s^{-1}) toward 2.5% (20%) of the galaxies. The fraction of blueshifted spectra does not vary significantly with stellar mass, color, or luminosity but does decline at specific star formation rates less than roughly 0.8 Gyr^{-1}. The insensitivity of the blueshifted fraction to galaxy properties requires collimated outflows at these redshifts, while the decline in outflow fraction with increasing blueshift might reflect the angular dependence of the outflow velocity. The low detection rate of infalling gas, 3%–6% of the spectra, suggests an origin in (enriched) streams favorably aligned with our sightline. We find that four of these nine infalling streams have projected velocities commensurate with the kinematics of an extended disk or satellite galaxy. The strength of the Mg II absorption increases with stellar mass, B-band luminosity, and $U - B$ color, trends arising from a combination of more interstellar absorption at the systemic velocity *and* less emission filling in more massive galaxies. Our results provide a new quantitative understanding of gas flows between galaxies and the circumgalactic medium over a critical period in galaxy evolution.

Key words: galaxies: evolution – galaxies: halos – ISM: structure – quasars: absorption lines – quasars: emission lines – ultraviolet: galaxies

Online-only material: color figures

1. INTRODUCTION

Key processes in the evolution of galaxies include the flow of cool gas into galaxies, the conversion of these baryons into stars, and the ejection of gas enriched with heavy elements. Determining the factors that govern the circulation of baryons remains a critical, unsolved problem in cosmology.

The measured properties of galaxies indicate strong evolution in this baryon cycle between the peak in star formation activity at redshift $z \approx 2$ and the current epoch (Lilly et al. 1996; Madau et al. 1996; Hopkins & Beacom 2006). At any redshift during this period, star-forming galaxies populate a fairly well-defined locus in the star formation rate (SFR)–stellar mass plane (Bell et al. 2005; Elbaz et al. 2007; Noeske et al. 2007a, 2007b). However, the observed SFR at a fixed stellar mass declines by about a factor of 20 from $z \sim 2$ to the present. The Tully–Fisher relation also evolves in the sense that present-day galaxies have about 2.5 times more stellar mass than do galaxies at $z \approx 2.2$ with the same circular velocity (Cresci et al. 2009). Since redshift $z \approx 1$ when roughly half the mass in present-day galaxies was assembled (Drory et al. 2005; Faber et al. 2007; Marchesini et al. 2009), the stellar mass in red-sequence galaxies has continued to grow; but the mass in blue galaxies has remained essentially constant (Faber et al. 2007). Over this period, some process quenches star formation in massive galaxies, yet observational efforts to identify this process with feedback from active galactic nuclei (AGNs) have not reached a consensus (cf. Schawinski et al. 2007; Aird et al. 2012).

The leading explanation for this drop in cosmic star formation activity is a decline in the accretion rate of cool gas onto galaxies. The simplest form of this idea, that the mean growth rate of dark matter halos regulates the gas inflow rate onto galaxies, fails; it yields too much star formation in low-mass halos at early times (Bouché et al. 2010) and does not shut down star formation in high-mass halos at later times (Somerville et al. 2008). Introducing gas physics—heating by virial shocks in massive halos *and* outflows in both low-mass and high-mass halos—effectively tilts the underlying relationship between halo accretion rate and mass (described by the simplest model) into the observed SFR–stellar mass relation and Tully–Fisher relation (Bouché et al. 2010; Davé et al. 2011a, 2012; van de Voort et al. 2011a, 2011b). The balance between gas outflow and inflow then determines the relationship between the gas-phase metallicity and stellar mass (Davé et al. 2011b). The problem with this scenario is that this baryon-driven picture of galaxy formation rests on a rather rudimentary understanding of which galaxies have outflows and inflows and how the physical properties of flows vary with fundamental galaxy properties.

Gas flows imprint resonance absorption lines on the spectra of their host galaxies that can often be kinematically distinguished from interstellar gas at the systemic velocity (Heckman et al.

[8] Packard Fellow.
[9] Alfred P. Sloan Fellow.

2000; Schwartz & Martin 2004; Martin 2005, 2006; Rupke et al. 2005; Schwartz et al. 2006; Tremonti et al. 2007; Martin et al. 2009; Rubin et al. 2010a). Thus far, studies of gas flows at $0.5 < z < 2$ have either been based on just a few individual galaxies (Sato et al. 2009; Coil et al. 2011; Rubin et al. 2011) or on *composite spectra*, i.e., the average of many low signal-to-noise (S/N) spectra (Weiner et al. 2009; Rubin et al. 2010b). The pioneering study of Weiner et al. (2009) concluded that blueshifted Mg II absorption was ubiquitous in spectra of star-forming galaxies at $z \sim 1.4$ and demonstrated that the Doppler shift and absorption equivalent width of this absorption increase (rather slowly) with both stellar mass and SFR. At lower redshift, however, Rubin et al. (2010b) did not find blueshifted Mg II absorption in a composite spectrum of galaxies with stellar masses similar to the Weiner et al. (2009) sample and speculated that the higher specific SFRs (i.e., SFR per unit stellar mass) characterizing $z \approx 1.4$ galaxies might be required to host such outflows. These two studies have demonstrated the existence of outflows and their possible evolution over a key period in the assembly of galaxies but are limited by their reliance on the *mean* spectrum of a population. Averaging many spectra together in a composite hides less common features like gas inflows (Sato et al. 2009; Rubin et al. 2012) and does not allow de-projection of the line-of-sight Doppler shift into an outflow velocity.

Here, we present the results of a survey of near-ultraviolet spectral features in 208 galaxies with redshifts between $0.4 < z < 1.4$ to provide an empirical measurement of how outflow and inflow properties change with cosmic time and galaxy properties. The galaxies were selected from the DEEP2 (Deep Extragalactic Evolutionary Probe 2) survey (Davis et al. 2003; Newman et al. 2012). This redshift survey provides a relatively unbiased sample for investigating the demographics of outflows and inflows in galaxies brighter than $R_{AB} = 24.1$ in four fields. More importantly though, selecting from the DEEP2 survey ensures that fundamental galaxy parameters—such as stellar mass, B-band luminosity, and $U - B$ color—have been measured for the sample in a systematic manner (Bundy et al. 2006; Willmer et al. 2006). The additional photometry obtained for the AEGIS (All-wavelength Extended Groth Strip International Survey) field allows us to measure SFRs for 51 of these galaxies; and these SFRs provide important information about the energy and momentum produced by supernovae, stellar winds, and radiation from massive stars and therefore available to drive outflows (Chevalier & Clegg 1985; Murray et al. 2005).

In this paper, we focus on the diagnostics provided by low-ionization, resonance absorption lines, reserving the presentation of high-ionization interstellar absorption and stellar features, resonance emission, and fluorescent emission for future papers. Low-ionization, resonance lines in near-ultraviolet (rest-frame) spectra provide an empirical bridge between the optical transitions typically observed for low-redshift galaxies and the far-UV transitions studied extensively in spectra of high-redshift galaxies (Steidel et al. 2010) because the Mg II λλ2796, 2803 doublet is accessible from the ground over the broad redshift range from roughly $0.25 < z < 2.5$ (Martin et al. 2009; Tremonti et al. 2007; Weiner et al. 2009; Rubin et al. 2010b; Coil et al. 2011). At the lower end of this redshift range, Mg II absorption properties can be cross calibrated with rest-frame optical lines such as Na I λλ5890, 96 and Ca II λ3933, 69. At $z \gtrsim 1.19$, the Mg II absorption properties can be directly compared to far-UV transitions in Si II, Al II, C II, and C IV commonly employed to study outflows in much higher redshift galaxies (Shapley et al. 2003; Steidel et al. 2010; Jones et al. 2012).

The Mg II doublet provides a very sensitive probe of outflows for several reasons: singly ionized magnesium is a dominant ionization state over a broad range of conditions, both lines have large oscillator strength, and the cosmic abundance of Mg is fairly high. Scattered Mg II emission, however, partially fills in the intrinsic absorption troughs in galaxy spectra and complicates the interpretation of the Doppler shift of the absorption trough. Spectral coverage blueward of the Mg II λλ2796, 2803 doublet provides access to a series of strong Fe II resonance lines which alleviate the concern about emission filling. The Fe II absorption troughs provide a cleaner view of the intrinsic absorption profile because fluorescence (rather than resonance emission) often follows absorption in several of these Fe II transitions (Prochaska et al. 2011; Erb et al. 2012). Another advantage of Fe II lines over the Mg II doublet arises from the large number of Fe II transitions in the near-UV (NUV). The oscillator strengths of the NUV Fe II transitions span a substantial range and therefore make it possible to place useful bounds on the column density of singly ionized iron, thereby constraining the total gas columns for an assumed (i.e., model-dependent) metallicity and ionization fraction.

The paper is organized as follows. Section 2 introduces the sample and describes our new Keck observations, including a discussion of the systemic velocity determination and absorption-line sensitivity. After providing a broad overview of the near-UV spectral features, Section 3 explains the complications caused by emission filling and how we identify and measure galactic gas flows. We then compare the line profiles of the Mg II and Fe II absorption troughs in Section 4. In Section 5, we calculate the fraction of galaxies with a Doppler shift of low-ionization absorption relative to the systemic velocity and use previously measured galaxy properties to illustrate the demographics of the galaxies showing blueshifts. We then discuss the physical properties of the outflows and show how the outflow properties scale with galaxy properties. In Section 6, we expound on our discovery of net inflows of enriched gas. Section 7 summarizes our conclusions.

Throughout this paper we assume a cosmological model with $\Omega_m = 0.3, \Omega_\Lambda = 0.7$, and $H_0 = 70\,\mathrm{km\,s^{-1}\,Mpc^{-1}}$. We adopt the atomic oscillator strengths and cosmic abundance ratios given by Morton (2003) as well as the associated vacuum wavelengths for transitions shortward of 3200 Å. We refer to optical transitions by their wavelengths in air (for ease of comparison to previously published work), but we work with their vacuum wavelengths.

2. DATA

We present rest-frame, ultraviolet spectroscopy of $z \sim 1$ galaxies drawn from the Deep Extragalactic Evolutionary Probe 2 survey (Davis et al. 2003; Newman et al. 2012) using the Low Resolution Imager and Spectrometer (LRIS) on the Keck I telescope (Oke et al. 1995). Building a sample of 208 spectra required a significant observational campaign, custom-designed masks for the focal plane, and the remarkable blue sensitivity of Keck/LRIS-B (Steidel et al. 2004). We describe the sample selection in Section 2.1 and the new observations in Section 2.2.

2.1. Sample

The DEEP2 survey obtained redshifts for approximately 38,000 galaxies spread over four fields widely separated in right

ascension (Newman et al. 2012). In three of the four fields, the galaxies were color selected to have redshifts $z > 0.7$. The fourth field, without color selection, is also the target of a deep imaging effort from the X-ray through the radio known as AEGIS (Davis et al. 2007). The panchromatic data in AEGIS provide more accurate estimates of galactic SFRs than are currently available for the other three fields (e.g., Noeske et al. 2007a, 2007b). Figure 1 summarizes the properties of the galaxies observed with LRIS.

Our primary sample of galaxies was chosen for spectroscopic follow-up based on redshift, $1.19 \leqslant z \leqslant 1.35$, and apparent magnitude $B < 24.0$. The magnitude cut ensures adequate continuum S/N for absorption-line spectroscopy. This lower bound on the redshift guarantees that the C IV λλ1548, 1550 doublet lands longward of the atmospheric cutoff in the blue; and requiring $z < 1.35$ ensures that the Mg I 2853 transition is covered by the blue spectrum. The simultaneous coverage of far-UV (FUV) and NUV resonance lines allows a direct comparison of the transitions used to measure outflow velocities in $z \geqslant 2$ galaxies (Steidel et al. 2010) and $z \sim 1$ galaxies (Weiner et al. 2009; Rubin et al. 2010b). In total, 68 galaxies meeting these criteria were observed on 6 masks. Each mask subtends a 5′.5 by 8′.0 field of view (Steidel et al. 2004). With an average of 11 primary targets per mask, we filled the masks with the following types of galaxies: (1) lower redshift ($z < 1.19$) galaxies with EW([O II]) > 10 Å and $B < 24.5$ mag, green-valley galaxies, and K+A galaxy candidates (Yan et al. 2009). In total, 145 galaxy spectra were obtained through these masks with the 400 lines mm^{-1} configuration of LRIS described below.

To utilize less-than-optimal observing conditions, a second set of masks was designed to obtain NUV spectroscopy of brighter galaxies. Spectra were obtained through three masks with galaxies prioritized as follows: (1) $B \leqslant 23.6$, $z \geqslant 0.7$, and EW([O II]) > 20 Å (41 objects); (2) $B \leqslant 23.6$, $z \geqslant 0.7$, and EW([O II]) < 20 Å (12 objects); (3) $B = 23.6$–24.0 and $z > 0.7$ (7 objects), $B \leqslant 23.6$ and $z < 0.7$(1 object), and six foreground galaxies that lie at small angular separation from another target. Among these 67 galaxies, the spectra of four foreground objects with $z < 0.4$ are not discussed further in this paper due to their much lower redshifts. Hence, the second sample includes 63 galaxies observed with the 600 lines mm^{-1} configuration of LRIS described below.

The primary sample ($z > 1.19$) includes three galaxies with colors that place them between the red sequence and blue cloud, a region of the color–magnitude diagram known as the green valley (Bell et al. 2003; Mendez et al. 2011). A total of 21 green-valley galaxies were included on the secondary (600 lines mm^{-1} backup) and primary (400 lines mm^{-1}) masks including the filler objects; most have EW([O II]) < 10 Å. The sample includes just two K+A (post-starburst) galaxies identified by Yan et al. (2009). One of these is a green-valley galaxy and the other is a K+A galaxy with colors just redward of the green valley in the color–magnitude diagram.

As illustrated in Figure 1, these targets span the redshift range from 0.4 to 1.4 have luminosities between $-17 > M_B > -22$, and sample the stellar mass function between $8.9 < \log(M/M_\odot) < 11.6$. With a few exceptions noted above, the galaxies have blue $U-B$ colors. These spectra therefore probe the properties of low-ionization gas in and around typical star-forming galaxies 4.3–9.0 Gyr ago. The broad range in stellar mass makes this an appropriate sample to compare gas outflows and inflows over about 3 dex in dark matter

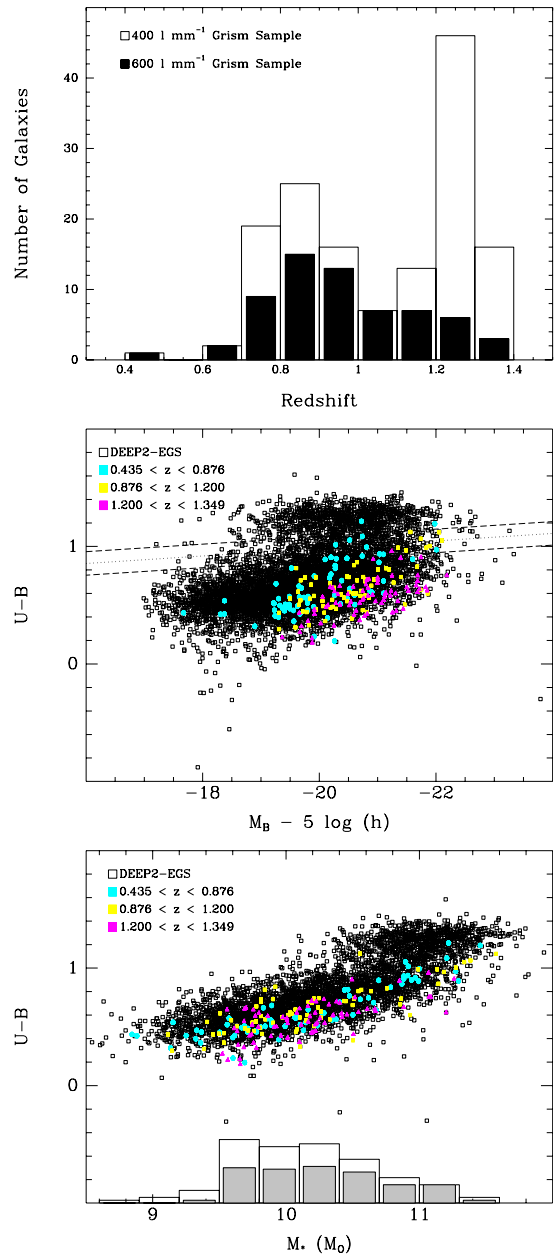

Figure 1. Properties of the galaxies observed with LRIS. Top: redshift histogram. Higher redshift galaxies were specifically targeted for the lower resolution observations in order to obtain spectral coverage of resonance lines in the FUV spectrum. The median redshifts of the galaxies observed with the 600 lines mm^{-1} (282 km s^{-1} FWHM) and 400 lines mm^{-1} (435 km s^{-1} FWHM) configurations are 0.94 and 1.12, respectively. Middle: color–magnitude diagram (Willmer et al. 2006). The diagonal dashed line marks the division between the red sequence and the blue cloud at $z \sim 1$. For the LRIS sample, galaxy color is anti-correlated with absolute magnitude, 7.8 standard deviations from the null hypothesis (i.e., no correlation) with Spearman rank correlation coefficient $r_S = -0.54$. The rest-frame optical colors of the galaxies (Willmer et al. 2006) become slightly bluer with increasing redshift due to the R-band selection of DEEP2 galaxies, and the lowest redshift tertile includes lower luminosity galaxies that would not pass our apparent magnitude cut at higher redshift. Bottom: color vs. stellar mass (Bundy et al. 2006) showing histogram of stellar mass along the bottom. Stellar mass was derived from SED fitting using a Chabrier stellar initial mass function (IMF; Chabrier 2003). The stellar masses would be 0.25 dex larger for a Salpeter IMF. The histogram distinguishes the most secure stellar masses (solid bars), obtained for 127 galaxies detected in the K band, from the full sample of 208 galaxies with LRIS spectroscopy. The median stellar mass of the K-band-detected galaxies in our sample is $1.60 \times 10^{10}\ M_\odot$, and the galaxies not detected in the K band have a median mass of $7.23 \times 10^9\ M_\odot$ as estimated from optical photometry. Color and stellar mass are strongly correlated ($r_S = 0.77$ at 11σ significance).

halo mass. The clustering of the population studied suggests that the most massive tertile of our sample resides in halos with $\log(M_h/M_\odot) > 12$ and that some of the galaxies in the lowest mass tertile populate halos with $\log(M_h/M_\odot) < 11$. In the stellar mass range $\log(M_*/M_\odot) = 9.0$–11.5, abundance matching suggests $\log(M_h/M_\odot) = 11.25$–$14.24$ at $z = 1.0$ and $\log(M_h/M_\odot) = 11.2$–14.7 at $z = 0.5$ (Behroozi et al. 2010), consistent with the halo masses measured from galaxy clustering.

2.2. LRIS Observations

Multislit spectroscopy of the fields listed in Table 1 was obtained with LRIS on the Keck I telescope between 2007 October and 2009 June. Our primary instrumental configuration used the D680 dichroic, the LRISb 400 mm^{-1} grism blazed at 3400 Å, and the 831 mm^{-1} grating blazed at 8200 Å on the red side. For the backup program, we configured LRIS with the D560 dichroic, 600 mm^{-1} grism blazed at 4000 Å, and the 600 mm^{-1} red grating blazed at 7500 Å; this setup generally provided continuous spectral coverage between the red and blue spectra. In both configurations, the red-channel wavelength coverage usually included rest-frame-optical emission lines, most commonly [O II] λλ3726, 29. For all observations, the Cassegrain Atmospheric Dispersion Corrector (ADC; Phillips et al. 2006) was enabled; and the width of the slitlets subtended 1″.2 on the sky. We observed a total of nine slitmasks, six in our primary configuration, and three in our backup configuration, as described below. Conditions during the observing runs ranged from excellent (clear with 0″.6 seeing) to variable (intermittent clouds with variable seeing up to 2″.0). Details of these observations are presented in Table 1.

The data were primarily reduced using IRAF tasks, with scripts designed for cutting up the multi-object slitmask images into individual slitlets, flat fielding using spectra of the twilight sky for the blue side and dome flats for the red side, rejecting cosmic rays, subtracting the sky background, averaging individual exposures into final stacked two-dimensional spectra, extracting to one dimension, wavelength and flux calibrating, and shifting into the vacuum frame.[10] These procedures are described in detail in Steidel et al. (2003). We also followed the procedures outlined in Shapley et al. (2006) for background subtraction of deep mask spectra. Accordingly, to avoid potential oversubtraction of the background, the object continuum location was excluded from the estimate of the background fit at each dispersion point. Along with each target science spectrum, we extracted an error spectrum from the standard deviation of the mean of the individual exposures. We paid particularly close attention to deriving accurate wavelength solutions, adjusting an initial wavelength calibration derived from arc lamp exposures such that sky lines in our spectra appeared at the correct wavelengths. Finally, spectra were flux calibrated using observations of spectrophotometric standards throughout the run. To calibrate the entire observed wavelength range, spectra of these stars were obtained through slits at multiple positions in the focal plane because the standard longslit spectral coverage is too blue relative to that of the multislit coverage.

The spectral resolution realized differed between the two configurations. In the primary configuration (400 lines mm^{-1} grism), the atmospheric seeing rather than the slit width determined the spectral resolution because the angular sizes of the galaxies (measured along the spatial direction of the slit) were slightly smaller than the slit. Scaling the width of arc lamp lines by this ratio, the average effective resolution was 435 km s^{-1} FWHM (full width at half-maximum intensity) in the grism spectra and 150 km s^{-1} in the grating spectra. In the 600 lines mm^{-1} configuration (used to observe lower redshift galaxies in non-optimal conditions), the galaxies typically filled the 1″.2 aperture; and the slit width set the spectral resolution. We measured line widths of 282 km s^{-1} FWHM in the blue spectra and 220 km s^{-1} FWHM in the red spectra.

2.2.1. Determination of the Systemic Velocity

Identifying net outflows or inflows requires accurate *relative redshifts* between the galaxy and the low-ionization gas. We derive the galaxy redshifts directly from the LRIS spectra whenever possible. The ADC used for the LRIS observations compensates for atmospheric differential refraction and eliminates systematic errors caused by the aperture subtending different regions of a spatially resolved galaxy at widely separated wavelengths. In most of our spectra, line emission in the [O II] doublet drives the determination of the galaxy redshift. Since dense, photoionized gas near star-forming regions produce this emission, we expect these redshifts to accurately describe the *systemic velocity*.

We derived LRIS redshifts for 167 galaxies using only the spectrum redward of the strong NUV Mg II and Mg I transitions ($\lambda_r > 3000$ Å). The most prominent spectral feature is usually the [O II] λλ3726, 29 doublet. However, strong [O III] λλ4959, 5007 and Balmer emission lines appear in spectra of the lower redshift galaxies; and Balmer absorption and the 4000 Å break are prominent in some spectra. Although we have attempted to avoid strong resonance lines that are blends of photospheric and interstellar lines, interstellar Ca II λ3933, 69 absorption could lower some of the LRIS redshifts relative to the purely stellar/nebular redshift in a few spectra. To estimate a redshift, each spectrum was cross-correlated with three templates—an emission-line galaxy, a quiescent galaxy, and a K+A galaxy—using the DEEP2 IDL pipeline; the best fit to a linear combination of these three templates was adopted as the LRIS redshift. How accurately we can find the centroid of spectral lines determines the statistical error on the redshift (and systemic velocity) for most galaxies. For a Gaussian line profile, the standard deviation of the mean, SDOM $\approx \sigma/\mathrm{SNR}$ describes the centroiding error. For a single line, the typical uncertainty is $\delta(v) \approx 19\,\mathrm{km\,s^{-1}}\,(\sigma/190\,\mathrm{km\,s^{-1}})(\mathrm{S/N}/10)^{-1}$, where $\sigma = \mathrm{FWHM}(\mathrm{km\,s^{-1}})/2.35$ is the spectral resolution.

For the 41 galaxies with no LRIS coverage of [O II], we adopted the DEEP2 redshift and estimated the typical error in the systemic velocity from the redshift differences measured among the 167 galaxies. A positive redshift difference, $z_{\mathrm{DEEP2}} - z_{\mathrm{LRIS}} > 0$, means that adopting the DEEP2 redshift increases the inferred outflow speed (makes it more negative) by an amount $\Delta v_{\mathrm{sys}} = c(z_{\mathrm{DEEP2}} - z_{\mathrm{LRIS}})/(1 + z_{\mathrm{LRIS}})$. The mean offset computed from 167 spectra is $\Delta v_{\mathrm{sys}} = -14 \pm 3\,\mathrm{km\,s^{-1}}$, quite small compared to typical outflow/inflow speeds. The standard deviation of 41 km s^{-1} indicates the size of the systematic error in the redshift estimate. For a spatially resolved source, uncertainties of this magnitude can result from an offset between the slit center and the brightest line emission; and although we use the same galaxy coordinates as the DEEP2 survey, the position angle of the slitlets generally differs.

[10] The typical rms error in the wavelength calibrations are 0.30 Å, 0.15 Å, 0.05 Å, and 0.05 Å, respectively, for the blue 400 lines mm^{-1}, blue 600 lines mm^{-1}, red 831 lines mm^{-1}, and red 600 lines mm^{-1} spectra.

Table 1
Keck/LRIS Observations

Field	R.A. (J2000.0)	Decl. (J2000.0)	Mask PA (°)	Grism/Grating (l mm^{-1})[a]	Dichroic	Conditions Cloud Cover & Seeing(″)	Exposure Time LRIS-B/LRIS-R (s)[b]	Number of Exposures (B/R)	Observing Run Dates
msc42_1	02 28 56.8	+00 33 39	120.0	400/831	d680	Clear to Mostly Cloudy & 0.9–1.6	11340/11100	6/6	2007 Oct 6–7
msc42_5	02 30 35.6	+00 28 17	143.0	400/831	d680	Mostly Cloudy to Light Cirrus & 0.7–0.9	26883/25400	15/14	2008 Sep 28–29
msc12_d	14 17 09.8	+52 31 18	165.0	400/831	d680	Clear to Mostly Cloudy & 0.6–2.0	18500/18000	10/10	2008 June 5–6
msc12_8	14 18 19.4	+52 34 33	5.0	400/831	d680	Clear to Partly Cloudy & 0.6–2.0	28800/26940	15/31	2009 June 18–21[c]
msc12_ee	14 18 46.8	+52 38 59	170.0	600/600	d560	Clear to Partly Cloudy & 0.6–2.0	11520/10800	6/12	2009 June 18–21[c]
msc22_bb	16 51 09.2	+34 58 15	25.0	600/600	d560	Clear to Mostly Cloudy & 0.6–2.0	18400/17950	9/9	2008 June 5–6
msc22_6	16 51 28.8	+34 48 09	60.0	400/831	d680	Clear to Partly Cloudy & 0.6–2.0	30760/23100	16/26	2009 June 18–21[c]
msc32_aa	23 29 19.5	+00 07 38	82.0	600/600	d560	Mostly Cloudy to Light Cirrus & 0.7–0.9	11070/10800	6/6	2008 Sep 28–29
msc32_1	23 30 18.9	+00 12 53	80.0	400/831	d560	Clear to Light Cirrus to Mostly Cloudy	25810/24182	14/14	2007 Oct 6–7 & 2008 Sep 28–29

Notes.

[a] After binning by 2 pixels in the dispersion direction, 400 lines mm^{-1} and 600 lines mm^{-1} blue spectra have 2.18 Å pixel^{-1} and 1.26 Å pixel^{-1}, respectively. The unbinned 831 mm^{-1} and 600 mm^{-1} red spectra have dispersions of 0.93 Å pixel^{-1} and 1.28 Å pixel^{-1}, respectively, for all runs except 2009 June.

[b] The typical exposure time per frame was 1800 s.

[c] The red spectra from 2009 June were obtained with a new detector. After binning by 2 pixels in the dispersion direction, the 831 mm^{-1} and 600 mm^{-1} red spectra have dispersions of 1.16 Å pixel^{-1} and 1.60 Å pixel^{-1}, respectively. Shorter exposure times were used for individual frames due to high cosmic ray rates.

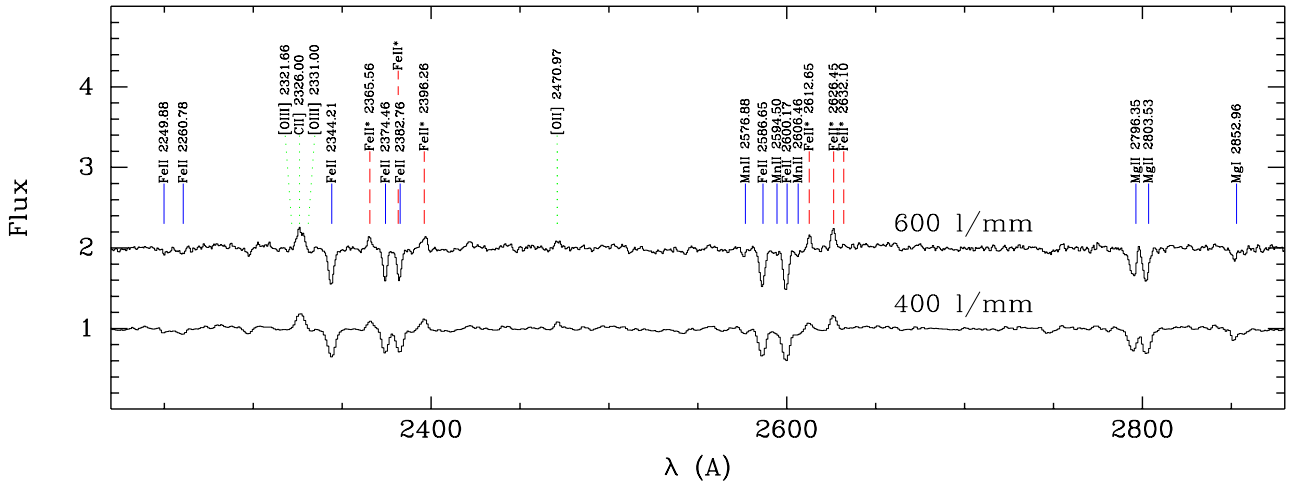

Figure 2. Composite, near-ultraviolet spectra of star-forming galaxies at $z \sim 1$. The continuum level has been normalized to unity. The lower spectrum shows the addition of all 208 continuum normalized spectra after smoothing them to a common resolution of 435 km s^{-1} FWHM. The upper spectrum is the average of 63 spectra observed at a resolution of 282 km s^{-1} FWHM. Vertical blue (solid), red (dashed), and green (dotted) lines mark, respectively, resonance absorption lines, fluorescent emission lines, and nebular emission lines. The unlabeled Fe II* transition is a weak line at λ2381.49; see C. L. Martin et al. (in preparation) for a tabular line list.

(A color version of this figure is available in the online journal.)

2.2.2. Sensitivity to Absorption Lines

Prior to making measurements, we de-redshifted the spectra to the rest frame. We fit a low-order spline to the continuum in each galaxy spectrum avoiding regions near spectral lines. We divided the spectra by the fitted continuum to produce normalized spectra. Uncertainty about the continuum level propagates into an error term in the equivalent width measurements. We found that the error term from the continuum fit could be kept small, compared the term derived from the error spectrum, by fitting the NUV continuum (approximately λ2200–2900) independently of the FUV and optical continua.

The resulting sensitivity to absorption lines is described by the minimum detectable equivalent width. Our observing strategy was designed to reach a rest-frame equivalent width $W_r(2796) \simeq 1$ Å because the distribution function of intervening absorbers presents a break here which may signal association with galaxy halos (Nestor et al. 2006). The weakest line that we detect depends on the continuum S/N at the observed wavelength of the transition as well as the intrinsic width of the absorption trough. In the 2400–2500 Å bandpass, the median S/Ns of the 400 lines mm^{-1} and 600 lines mm^{-1} spectra are 6.5 and 5.5 (per pixel), respectively. For purposes of illustration, a typical equivalent width limit can be estimated assuming S/N $\sim$ 5 and the FWHM of an unresolved line. In the near-UV Fe II series, absorption troughs with rest-frame equivalent widths stronger than

$$W_{3\sigma} = 0.92\,\text{Å}\,(6.5/\text{SNR})_{\lambda 2450} \quad (1)$$

in 400 lines mm^{-1} spectra, or larger than

$$W_{3\sigma} = 0.65\,\text{Å}\,(5.0/\text{SNR})_{\lambda 2450} \quad (2)$$

in 600 lines mm^{-1} spectra, are easily detected. Just blueward of the Mg II doublet, the median continuum S/Ns of the 400 lines mm^{-1} and 600 lines mm^{-1} spectra are, respectively, 4.6 and 6.6. The typical rest-frame sensitivities of the 400 lines mm^{-1} and 600 lines mm^{-1} spectra are, respectively,

$$W_{3\sigma} = 2.02\,\text{Å}\,(5.0/\text{SNR})_{\lambda 2790} \quad (3)$$

and

$$W_{3\sigma} = 0.58\,\text{Å}\,(5.0/\text{SNR})_{\lambda 2790}. \quad (4)$$

Farther to the red near the Mg II doublet, the continuum S/N in a particular spectrum is usually a bit lower than it is near Fe II λλ2587, 2600 due to the blue blaze of both grisms, so some of the spectra do not quite reach the target sensitivity in Mg II. Spectra with S/N adequate to detect equivalent widths of 1–2 Å in individual galaxies at $z \sim 1$ have never been previously presented however in such large numbers.

We measure the Doppler shift of resonance absorption relative to the systemic velocity. Since this systemic velocity, as well any projected gas flow, may vary slightly with slit position, the systematic error in the Doppler shift of the resonance lines could, in exceptional geometries, be as large as the systematic error of 41 km s^{-1} estimated above. Typically, however, the statistical error in centroiding the absorption lines will characterize the error on the Doppler shift. The resolution of the 400 lines mm^{-1} spectra, expressed by the standard deviation σ, is 1.54 times coarser than that of the 600 lines mm^{-1} spectra; but this lower resolution is partly offset by higher average S/N spectra of the 400 lines mm^{-1} subsample. For emission lines in our best 400 lines mm^{-1} and 600 lines mm^{-1} spectra, this statistical error is about $\delta V \approx 185/25 \approx 7$ km s^{-1} and $\delta V \approx 120/10 \approx 10$ km s^{-1}, respectively. Fitting multiple absorption lines, as described in Section 3.3, further reduces the statistical error on our best estimate of Doppler shift V_1 of the Fe II series.

3. DIAGNOSTICS OF OUTFLOWS AND INFLOWS

In this paper, we explore the diagnostics in the near-UV absorption-line spectrum longward of 2000 Å. The emission-line spectra are discussed further in two companion papers (C. L. Martin et al., in preparation; K. A. Kornei et al., in preparation). We defer the discussion of the far-UV spectral features to a future paper.

3.1. Near-UV Spectral Features

In Figure 2, we show the spectral region around the following NUV resonance lines: Fe II λ2249.88, 2260.78, 2344.21,

2374.46, 2382.77, 2586.65, and 2600.17; Mg II λλ2796.35, 2803.53; and Mg I λ2852.96. The absence of strong absorption in some individual spectra will partially fill in the absorption troughs in the composite spectra. Inspection of the individual spectra, however, shows that other factors prevent the absorption troughs from appearing completely black. Foremost, instrumental resolution smooths the spectrum and explains why the absorption troughs are slightly deeper in the 600 lines mm^{-1} composite than in the 400 lines mm^{-1} composite. In addition, the absorbing gas likely only partially covers the continuum source allowing some continuum light to leak out and fill in the absorption troughs; this partial covering has been fitted as a function of velocity using higher resolution spectra of brighter galaxies (Martin et al. 2009). All three of these factors—partial covering, instrumental resolution, and averaging spectra—imply that saturated absorption troughs need not be black.

Nebular emission lines mark dense gas near star-forming regions excited by either photoionization or shocks. The LRIS red-side spectra typically show strong [O II] λλ3726, 29 emission and cover an increasing number of rest-frame optical lines with decreasing redshift. In the NUV composite spectra, the [O II] λλ2470.97, 2471.09 lines are detected and blended. We attribute the broader width of the strong emission feature at λ2326 to a blend of various [C II] transitions; in our picture, the Fe II λ2328 feature, which Rubin et al. (2010a) suggested contributed to this emission complex, does not contribute because its upper level cannot be populated by a permitted transition from the ground state.

Line blending complicates measurements of the absorption troughs. The individual transitions of the Mg II doublet blend together in the 600 lines mm^{-1} composite in Figure 2. The Fe II λλ2587, 2600 doublet can blend with the Mn II λλλ2576.88, 2594.50, and 2606.26 triplet, recognizable in the higher resolution composite in Figure 2. Strong [C II] λ2326 emission often blends with the blue wing of λ2344. In some individual spectra, the Mn II or [C II] contamination compromises measurements of the maximum blueshift of absorption in the Fe II λ2587 and Fe II λ2344 line profiles, respectively. In contrast, the Fe II* λ2365 emission blueward of Fe II λ2374 is much weaker than the [C II] λ2326 emission, leaving λ2374 as the preferred transition for looking for highly blueshifted Fe II absorption.

The Fe II λ2374 transition has the lowest oscillator strength among the NUV Fe II transitions routinely detected in the individual spectra. The oscillator strength of Fe II λ2374 is only a tenth that of the strongest transition, Fe II λ2383. The oscillator strengths of Fe II λ2383 and Mg II λ2803, the weaker line in the Mg II doublet, are nearly equal. The shorter wavelength transition in the Mg II doublet has an oscillator strength twice that of the longer wavelength transition. The rough equality of the absorption equivalent widths in all these transitions in Figure 2 demonstrates the resonance absorption is typically optically thick. The weak Fe II λ2250 and λ2261 transitions, just barely detected in Figure 2, are optically thin and particularly useful for constraining the column density of single-ionized iron, $N(Fe^{+})$.

Among our spectra, we often find surprisingly low Fe II λ2383 equivalent widths relative to the other Fe II absorption lines. We attribute this apparent contradiction of the intrinsic line strengths to resonance emission partially filling in the deeper, intrinsic absorption profile. This *emission filling* is more significant in Fe II λ2383 than the other strong Fe II transitions because Fe II λ2383 absorption does not produce fluorescent emission; i.e., the only permitted transition from the excited state is decay to the ground state. When an absorption trough is partially filled in by emission, the centroid will generally differ from the intrinsic absorption profile because absorption samples only the gas between the observer and the galaxy, while emission may come from both the near and far sides of the galaxy.

Many of the individual spectra show prominent Mg II emission lines. In Figure 2, the longer wavelength, lower oscillator strength transition in the Mg II doublet has the larger equivalent width, an unphysical situation for the intrinsic equivalent width ratio. The inverted apparent ratio may arise from the troughs being partially filled in by resonance emission. For example, if the intrinsic absorption troughs are saturated, then the two troughs will have equal intrinsic equivalent width; and slightly stronger emission in Mg II 2796 will produce the inverted ratio of the net equivalent widths. Simple, radiative-transfer models do not produce these inverted ratios (Prochaska et al. 2011), and more detailed modeling is needed to test this idea. A non-spherical geometry, for example, allows the absorption and emission to come from physically distinct regions of the galaxy with differing optical depths. Furthermore, it may be quite important to consider multiple origins of the Mg II line photons, which are both emitted by H II regions (Erb et al. 2012) and generated by continuum absorption throughout the interstellar medium (ISM) and circumgalactic medium.

3.2. Emission Filling

In the normal situation for intervening absorption in quasar spectra, where the continuum source subtends a small angular size compared to the gas clouds, a negligible fraction of photons absorbed in the resonance transitions are re-emitted along our sightline. For extended sources like galaxies, however, the equivalent width of the emission can be comparable to the absorption equivalent width.

At low densities, every excitation from the ground state decays as either resonance emission or fluorescent emission. In the absence of dust, photon number is conserved, and the equivalent width of the resonance emission (plus any fluorescent emission from the same upper level) will be exactly equal to the absorption equivalent width. The resonance emission will generally not cancel out the absorption trough due to their velocity offset, generated for example by radial gas flow. The absorption trough reflects only the kinematics of gas in front of the continuum source while the emission-line profile probes the kinematics of both the near and far sides of the galaxy. Departure from a spherically symmetric gas distribution generates specific viewing angles for which spectra will show stronger absorption than emission (and other angles with emission stronger than absorption). In addition to dust and the geometry of the gas distribution, spectroscopic apertures smaller than the emission region will also produce unequal emission and absorption equivalent width. Hence, it is not surprising that the LRIS spectra rarely show equal absorption and emission equivalent widths.

The point is that resonance emission should be expected in galaxy spectra, and we must consider how much it fills in the intrinsic absorption profile, a phenomenon we call *emission filling*. In spectra of nearby galaxies, the near absence of emission filling in Na I λλ5890, 96 has long been attributed to the high gas densities in regions with a significant neutral sodium fraction; the large pathlength of scattered photons produces

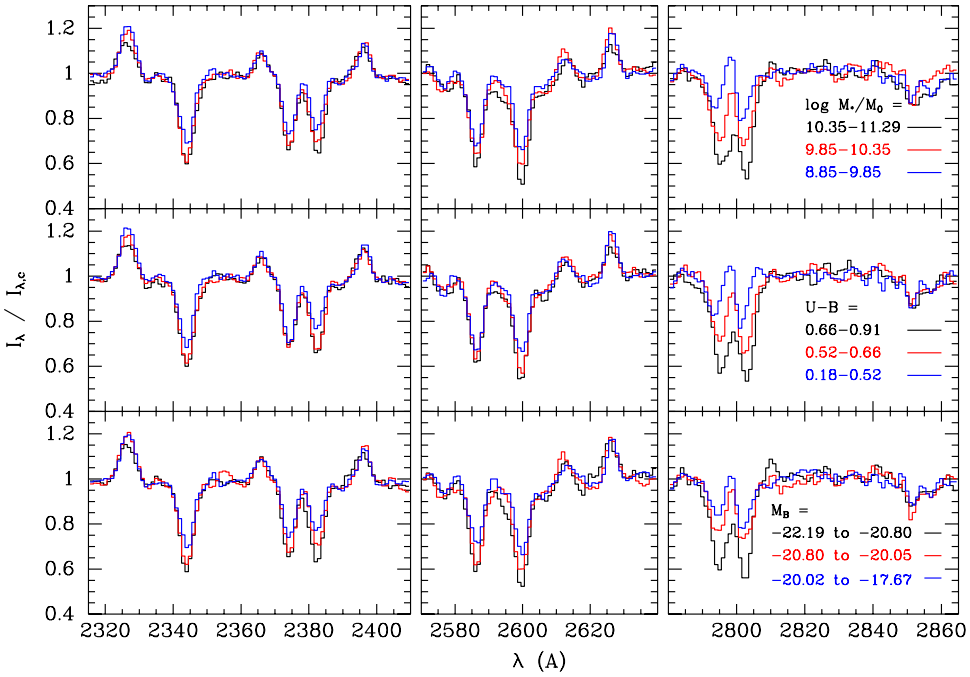

Figure 3. Comparison of the Fe II and Mg II line profiles in average spectra of galaxies with different properties. Top: toward lower mass galaxies, the Mg II absorption troughs become shallower, the Mg II emission becomes stronger, and the Fe II* emission in λ2612, 2626 increases. In the highest mass tertile, the Mg II doublet ratio is not inverted, and Fe II λ2383 has a higher equivalent width than Fe II λ2374, as it should in the absence of emission filling. Middle: we see similar trends with color because color is strongly correlated with stellar mass (redder galaxies are more massive on average). Bottom: the resonance absorption troughs become deeper in more luminous galaxies. See the text for a full explanation of why the stronger absorption in more luminous, redder, more massive galaxies is largely attributable to emission filling.

(A color version of this figure is available in the online journal.)

a high probability of absorption by a dust grain (Heckman et al. 2000; Martin 2005, 2006; Chen et al. 2010). Quite often, the Mg II regions in galaxy spectra exhibit a P Cygni profile, which clearly shows resonance emission filling in the part of the intrinsic absorption trough near the systemic velocity (Martin et al. 2009; Weiner et al. 2009; Rubin et al. 2011; Coil et al. 2011; Erb et al. 2012).

Absorption from the ground state necessarily leads to resonance emission when the ground state has a single level, such as in the cases of Na I, Mg II, and C IV ions, but can be followed by fluorescent emission when the ground state has fine structure, such as for the Fe^+ and Si^+ ions. In the composite spectra in Figure 2, we identify fluorescent Fe II* lines at λ2365.56, 2396.26, 2612.56, and 2626.45; the Fe II* λ2632.10 line may be marginally detected in a few individual spectra. Because these Fe II* emission lines all have upper levels that are populated by absorption from the ground state, we can attribute them to fluorescence. No absorption from excited levels in Fe II is detected consistent with densities well below the critical densities of the Fe II transitions.

We understand the reduction in Fe II λ2383 equivalent width relative to Fe II λ2374 in terms of emission filling. The spectroscopic selection rules for total angular momentum imply that the Fe II λ2383 photons will scatter like the common transitions (such as Mg II λλ2796, 2803) with a singlet, ground state. Absorption of Fe II λ2374 photons, however, can produce fluorescent Fe II*λ2396.26 photons that do not fill in the resonance absorption trough. The relative radiative decay rates suggest that 88% of Fe II λ2374 absorptions will decay as Fe II*λ2396.26 photons.

Fluorescent emission following Fe II λ2344 absorption in Fe II* λ2381.49 will also contribute to filling in the Fe II λ2383 absorption trough, but the resonance scattering of the latter will dominate the emission filling of the Fe II λ2383 trough. An analogous situation arises in the longer wavelength Fe II multiplet shown in the middle panel of Figure 3, where absorption in the transition with the higher oscillator strength, Fe II λ2600, usually results in emission of a photon at the same wavelength. In contrast, the excited level of the weaker transition Fe II λ2587 typically decays via a longer wavelength, and therefore fluorescent, photon. Comparison of the Einstein A coefficients among all the transitions from the excited level indicates a decay via Fe II* λ2612.65 45% of the time, through Fe II* λ2632.10 23% of the time, and in the resonance transition λ2587 the remaining 32% of the time. These fluorescent emission lines, and the Fe II* λ2626 fluorescence that follows the absorption in the Fe II λ2600 resonance transition (13% of the time), are clearly detected in the spectra shown in Figures 2–5 and will be discussed further in a forthcoming paper (K. A. Kornei et al., in preparation; C. L. Martin et al., in preparation).

Photons absorbed in the Mg I λ2853 transition will scatter (rather than fluorescence) because the ground state is again a singlet. Could emission filling also explain the decreasing equivalent width of Mg I λ2853 in the spectra of lower mass galaxies seen in Section 4. It would be premature to draw this conclusion from the equivalent widths of the Mg I λ2853 feature alone; any of a number factors—such as a decrease in the gas velocity dispersion, an increase in the Mg II ionization fraction, or a reduced covering fraction—would systematically decrease the equivalent width with decreasing stellar mass.

The presence of Mg II emission in galaxy spectra (Martin et al. 2009; Weiner et al. 2009) can often be attributed to resonant scattering (Rubin et al. 2011; Coil et al. 2011; Erb et al. 2012). Emission that fills in part of the absorption

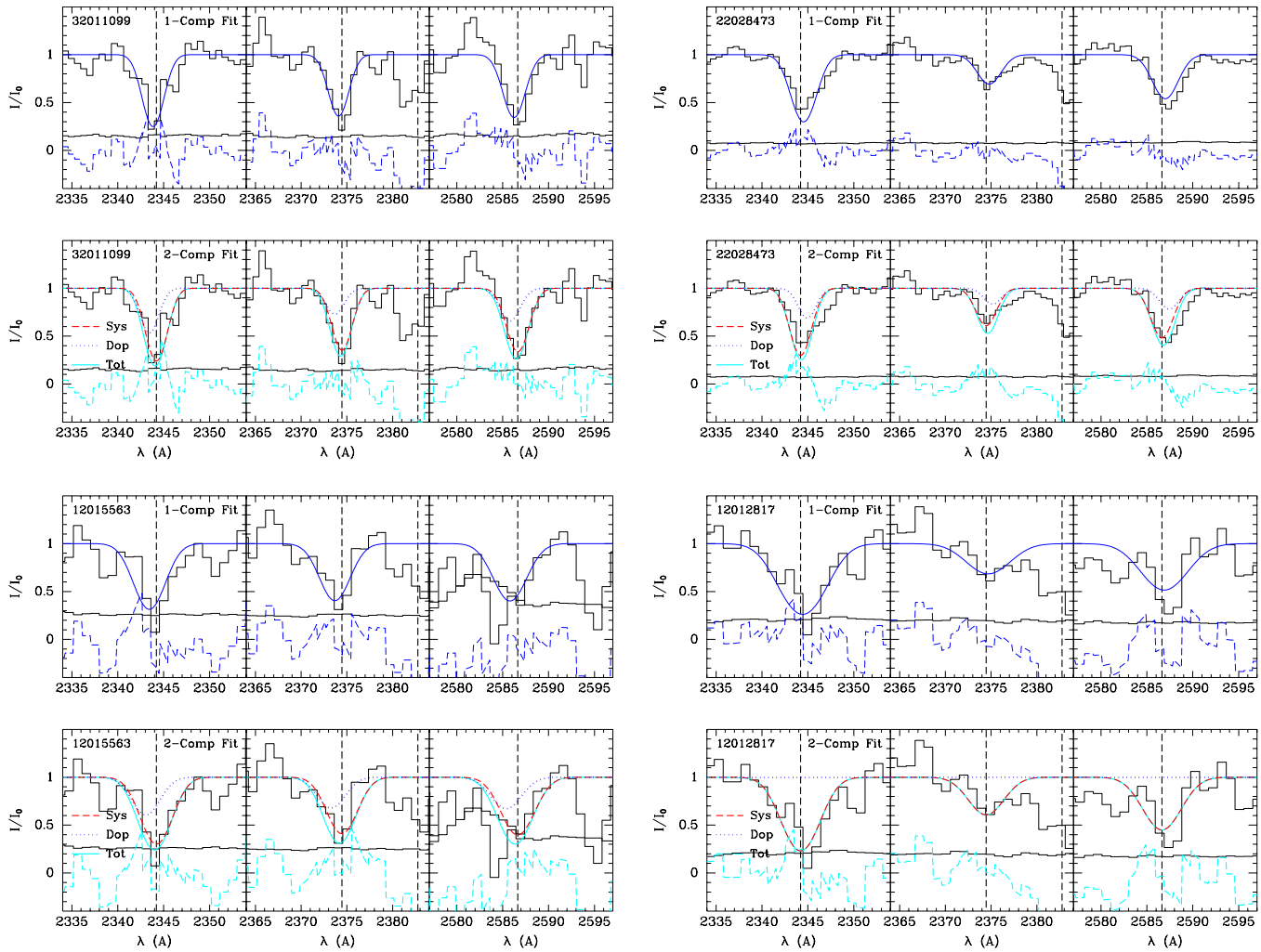

Figure 4. Four comparisons of single-component (top panels) and two-component (bottom panels) fits to the Fe II series with residuals shown at the bottom. Top left panels: the single-component fit to the 600 lines mm^{-1} spectrum of 32011099 yields an outflow velocity of -46 ± 14 km s^{-1}. In a two-component fit, a systemic component at zero velocity describes much of the total absorption equivalent width; but the fit also requires a blueshifted Doppler component ($V_{\rm Dop} = -101 \pm 25$ km s^{-1}, $W_{\rm Dop} = 1.16$ Å) to model the net blueshift of the absorption trough. Top right panels: the single-component fit to the 600 lines mm^{-1} spectrum of 22028473 yields an inflow velocity of 42 ± 10 km s^{-1}. In a two-component fit, a systemic component at zero velocity describes much of the total absorption equivalent width; but the fit also requires a redshifted Doppler component ($V_{\rm Dop} = 133 \pm 47$ km s^{-1} for the inflow and $W_{\rm Dop} = 0.46$ Å) to model the net redshift of the absorption trough. Bottom left panels: the single-component fit to the 400 lines mm^{-1} spectrum of 12015563 yields an outflow velocity of -98 ± 42 km s^{-1}. In a two-component fit, a systemic component at zero velocity describes much of the total absorption equivalent width; but the fit also requires a blueshifted Doppler component ($V_{\rm Dop} = -154 \pm 84$ km s^{-1}, $W_{\rm Dop} = 1.55$ Å) to model the net blueshift of the absorption trough. Bottom right panels: the single-component fit to the 400 lines mm^{-1} spectrum of 12012817 yields $V_1 = 29 \pm 44$ km s^{-1} and does not require a net flow. In a two-component fit, a systemic component at zero velocity describes much of the total absorption equivalent width; we classify the Doppler component as insignificant because the equivalent width is extremely low and the change in the fit statistic is tiny. In general, the two-component fits increase the estimated velocity of the flow, relative to the single-component fit.

(A color version of this figure is available in the online journal.)

trough greatly complicates the interpretation of the Doppler shift and equivalent width of Mg II absorption in galaxy spectra. Radiative-transfer models, however, predict little emission at the highest outflow speeds (Prochaska et al. 2011). The maximum blueshift of the Mg II λ2796 absorption is therefore the only property of the intrinsic absorption profile that we can routinely measure directly. The maximum blueshift of the absorbing gas has also been used previously to discuss whether outflowing gas is bound to the galaxy (e.g., Heckman et al. 2000, 2011; Martin 2005; Martin et al. 2009; Weiner et al. 2009; Coil et al. 2011).

3.3. Fitting Fe II Absorption Troughs

Examination of our spectra showed that emission filling complicates the direct measurement of intrinsic absorption properties, especially in the Mg II λλ2796, 2803, Fe II λ2383, and Fe II λ2600 transitions. First, the equivalent widths measured for transitions from a single ion do not always follow the curve of growth (Spitzer 1978). In Figure 2 spectra, the highest oscillator strength Fe II transition at λ2383 has a lower equivalent width than other Fe II transitions. Second, a partially filled absorption trough has a centroid velocity that is bluer than the centroid of the intrinsic absorption profile because the resonance line emission is closer to the systemic velocity than is the absorption. This prevents robust measurement of the Doppler shift without detailed modeling (Prochaska et al. 2011). Figures 7 and 8 in the recent work of Erb et al. (2012) further illustrate these points quantitatively.

We circumvent these problems by adopting the centroid velocity of Fe II absorption rather than Mg II as our primary indicator of the net Doppler shift of the low-ionization gas. In

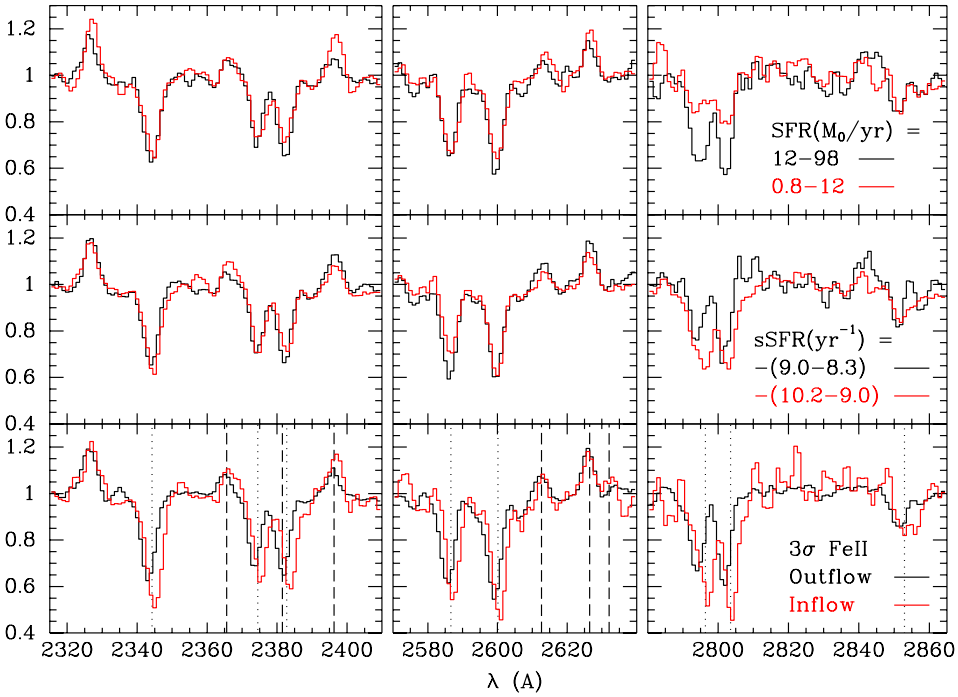

Figure 5. Composite spectra for subsets of galaxies with measured SFR or significant bulk flows. Top: the higher SFR galaxies have higher equivalent widths in Mg II, Fe II λ2600, and Fe II λ2383. Middle: these absorption equivalent widths have a weaker dependence on specific SFR. The Mg II equivalent width is slightly lower in the half of the subsample with the highest SFRs. The inverted equivalent width ratio in Mg II clearly indicates this is due to the emission filling. Bottom: the subset of galaxies with the most significant Fe II blueshifts is compared to the subset with significant Fe II redshifts. The continuum S/N is lower in the "inflow" spectrum (10 galaxies) than the "outflow" spectrum (35 galaxies). The wavelengths of the resonance absorption lines are marked with dotted lines for reference; and the Fe II* transitions are marked with dashed lines.

(A color version of this figure is available in the online journal.)

our discussion of emission filling, we explained why we expect the Fe II λ2344, 2374, and 2587 absorption troughs to reflect the outflow opacity more closely than does the Mg II profile. Absorption in these transitions usually leads to fluorescence (i.e., emission of a longer wavelength photon) rather than scattering, so the intrinsic shape of the absorption trough is much less affected by emission filling than the Mg II or Fe II λ2383 lines. We therefore fit only those transitions that have a high probability of fluorescence, i.e., decaying via a longer wavelength photon rather than scattering and thereby filling in the absorption trough.

We detect resonance absorption lines at high significance in the individual LRIS spectra. Since the spectral resolution does not fully resolve the shapes of most absorption troughs, we can only robustly measure the Doppler shifts and equivalent widths of these absorption troughs in general. Centroid velocities have been widely used to describe galactic outflows in the past, but we caution the reader that interstellar absorption near the systemic velocity blends with the absorption profile from outflowing (inflowing) gas in a low resolution spectrum. In Section 3.3.2, we will examine how interstellar absorption at the systemic velocity biases the estimates of outflow properties.

3.3.1. Single-component Fits Describing the Absorption Centroid Velocity

In Figure 4, we show examples of the Fe II absorption-line profiles from our LRIS data. The Doppler shift was jointly fit to five Fe II transitions: Fe II λ 2250, 2261, 2344, 2374, and 2587. The Fe II transitions at λ2383 and λ2600 are excluded from the fit because they show the strongest emission filling. Even though they significantly constrain the column density, the weak Fe II 2250 and 2261 transitions provide little constraint on the Doppler shift. The fitted model simply describes the net Doppler shift of the intrinsic Fe II absorption.

The shapes of the absorption troughs are strongly influenced by the instrumental response and are therefore often well described by a Gaussian line profile. We adopted a more physical description of the line profile in order to properly model the relative line strengths in the Fe II series. For each transition, j, our fitting function takes the form

$$I_j(\lambda) = I_{c,j}(\lambda)e^{-\tau_j(\lambda)}. \quad (5)$$

The optical depth distribution,

$$\tau_j(\lambda) = \tau_{0,j}e^{-(\lambda-\lambda_{0,j})^2c^2/(b^2\lambda_{0,j}^2)}, \quad (6)$$

introduces the Doppler parameter b in order to describe the location of the absorbing clouds in velocity space relative to line center. The central wavelengths of the five Fe II transitions, $\lambda_{0,j}$, are tied together to define a single Doppler shift, V_1. The optical depths of the different transitions are tied together by the ratio of their oscillator strengths (and the rest wavelengths of the transitions), so one parameter $\tau_0(\lambda 2344)$ is sufficient to define the absorption optical depth at line center for each transition. Equivalently, the product of the column density and the covering factor, $N(\mathrm{Fe}^+)C_f^{-1}$, determines the optical depth in each transition. When line profiles from multiple transitions overlap at a given wavelength, e.g., redshifted Fe II λ2374 and blueshifted Fe II λ2383, we add their respective contributions to the total optical depth at that wavelength, $\tau(\lambda)$. Provided the form of the optical depth distribution is symmetric about the centroid of the line profile, λ_0, the shape of this distribution

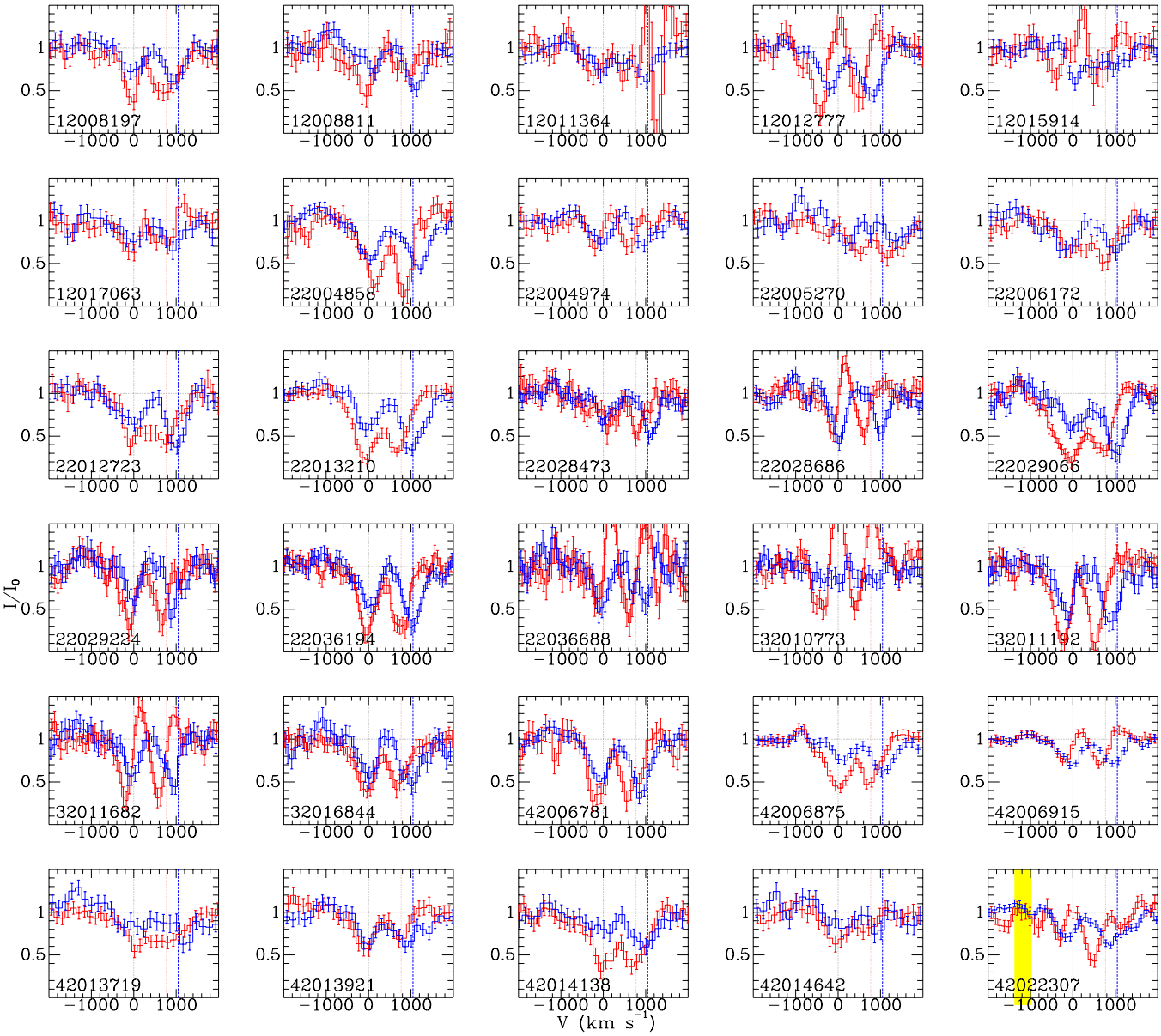

Figure 6. Comparison of the Mg II λ2796 (red spectrum) and Fe II λ2374 (blue spectrum) line profiles in spectra with continuum S/N greater than 10 at λ2450. The black, vertical line marks the systemic velocity. Near Fe II λ2374, note the location of Fe II* 2365 at $-1124\,\mathrm{km\,s^{-1}}$ (blueward) and Fe II λ2383 at $1048\,\mathrm{km\,s^{-1}}$ (vertical blue line). Near Mg II λ2796, note the Mg II 2803 line at $769\,\mathrm{km\,s^{-1}}$ (vertical red line). The location of strong telluric lines that interfere with measurement of the blue wing are noted in yellow. In the spectra of 22028686, 22036688, and 42006915, resonance emission prominently fills in the Mg II absorption troughs near systemic velocity and likely affects the shape of the Mg II absorption troughs in many spectra. Despite emission filling, however, the Mg II lines generally have higher absorption equivalent width than the Fe II λ2374 line, as can be seen from comparison of the blueshifted portions of their line profiles. A blue wing on the Mg II absorption trough is partially resolved in some spectra including 12008811, 12012777, and 42014138.

does not affect the fitted central wavelength λ_0, which defines the Doppler shift V_1.[11]

The free parameters V_1, b, and $\tau_0(\lambda 2344)$ were fitted as follows using custom software. Each galaxy spectrum was de-redshifted to the rest frame and normalized by the continuum. A model with line profiles centered at zero velocity was created assuming $b = 200\,\mathrm{km\,s^{-1}}$ and $\tau_0 = 1$. The model was convolved with a Gaussian profile of width $\sigma = 120(185)\,\mathrm{km\,s^{-1}}$, which describes the instrumental response for the 600 lines mm^{-1} (400 lines mm^{-1}) spectra. The residuals between the model and the data were minimized iteratively

[11] In our schematic picture, the angular extent of the stellar population producing the continuum emission is much larger than that of a gas cloud. This partial covering of the continuum source has often been described by a covering factor, C_f, which represents the fractional area of the continuum source covered by gas clouds. Since a fraction $(1 - C_f)$ of the galaxy continuum is observed directly without any absorption, a widely used, alternative parameterization of the line profile is $I(\lambda)/I_c(\lambda) = 1 - C_f + C_f e^{-\tau(\lambda)}$ (e.g., Rupke et al. 2005). This parameterization of the absorption trough, however, does not capture the strong velocity dependence of the covering factor found by Martin et al. (2009). For this reason, and because velocity-dependent covering factors (Arav et al. 2005) introduce structure in the line profile that cannot be observed at the resolution of our spectra, we simply fitted the three-parameter model of Equation (5). For any symmetric $C_f(v)$ distribution, partial covering will clearly not impact the fitted Doppler shift. In our simple parameterization of the line profile, Equation (5) where $C_f \equiv 1$, the width of the absorption trough depends on both b and τ_0. When we attempted to include a covering factor in the description of the line profile, we found b, C_f, and τ_0 were all strongly covariant due to the low resolution of our data.

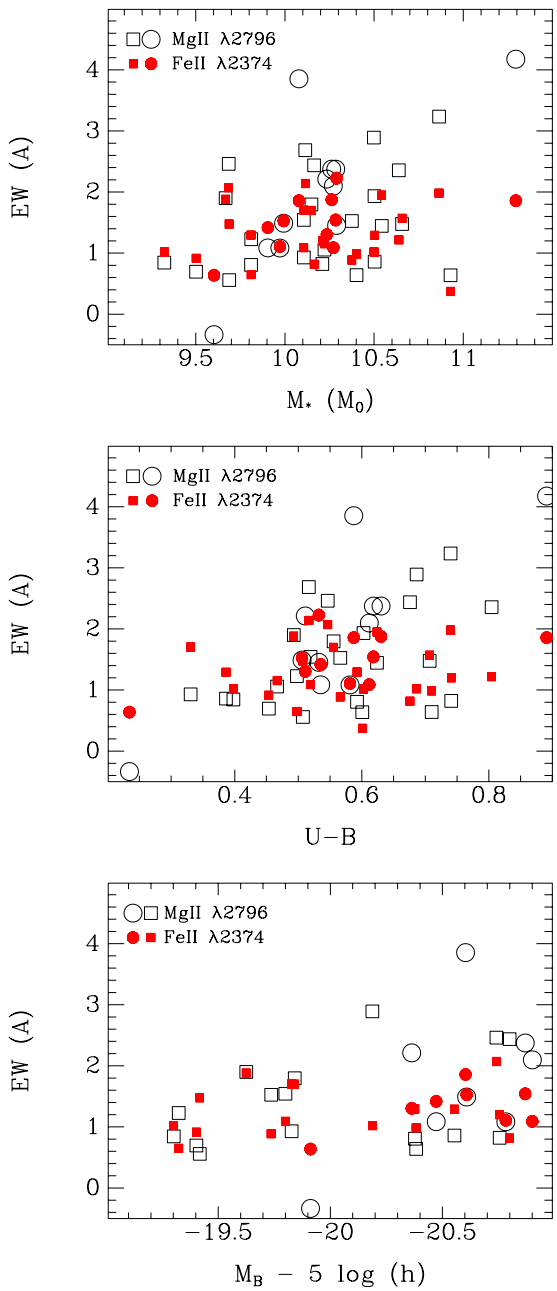

Figure 7. Equivalent widths of the Mg II λ2796 and Fe II λ2374 absorption troughs in individual, high S/N spectra. Squares and circles represent the 400 lines mm^{-1} and 600 lines mm^{-1} spectra, respectively. The Mg II equivalent width is positively correlated with stellar mass, color, and *B*-band luminosity; see Table 6. (To mitigate the impact of emission filling on the Mg II absorption measurement, we have integrated the area of the absorption from −1000 to 0 km s^{-1}.)

(A color version of this figure is available in the online journal.)

using the Levenberg–Marquardt algorithm (Press et al. 1992) to make successive parameter estimations; the median reduced χ^2 value was close to unity. The resulting covariance matrix provides a good estimate of the uncertainty in a fitted parameter when the errors are normally distributed. We tested this assumption by bootstrap resampling typical spectra. The resulting distributions of Doppler shift measurements were found to be normally distributed, so we use the corresponding element of the covariance matrix to estimate the 68% confidence interval on V_1, $\delta V_1 \equiv \sqrt{\sigma^2_{V1,V1}}$. The Doppler shifts from the joint fit, V_1,

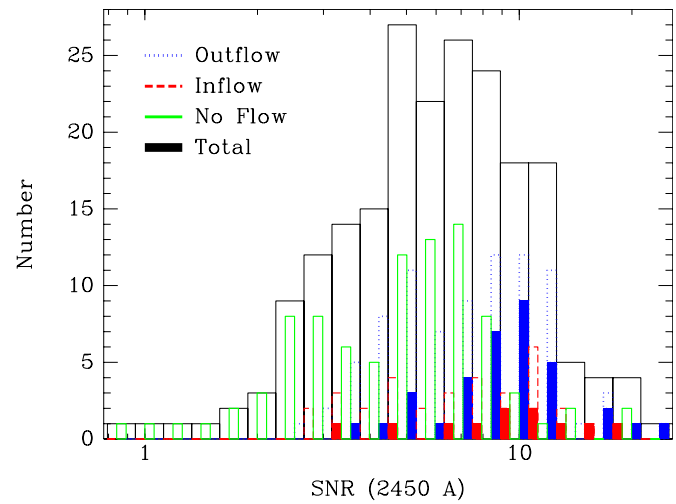

Figure 8. Histogram of continuum S/N measured between 2400 Å and 2500 Å (computed from the full sample of 208 galaxies). Outflows/inflows are selected by the sign of the Doppler shift, V_1, fitted to the Fe II absorption troughs. The more secure 3σ blueshifts/redshifts are denoted by the solid histograms, and a more generous 1σ cut denoted by the extended open histogram of the same color. Among the full sample of 208 spectra, the fraction of Fe II outflows is very sensitive to the sample's distribution of S/Ns. Net flows at the 3σ confidence level are extremely rare in spectra with SNR < 5; yet their fraction grows to about 58% at SNR ≈ 9 (36% with S/N > 9). A significant fraction of high S/N spectra present no net flow.

(A color version of this figure is available in the online journal.)

were also found to be consistent with the average of the velocities measured in the individual fits to Fe II λ2344, λ2374, and λ2587. The error distributions for τ_0 and b, in contrast, are often not normally distributed, so we do not use these fitted parameters in our analysis; we choose instead to discuss measurements of equivalent width and (in a later section) the bluest absorption velocity, $V_{\rm max}$.

These joint fits to five Fe II lines describe the Doppler shift of the entire absorption trough with one velocity, so we will refer to them as the *single-component* fits. They avoid transitions with strong emission filling and beat down statistical error by combining information from multiple transitions. Within the LRIS sample of 208 spectra, 36 had no good Fe II lines to fit due sky line residuals (5 cases) or low equivalent widths (31 spectra); and the fit failed to converge for an additional 7 spectra. Since the 43 spectra without a fit have low continuum S/N, the absence of significant absorption does not provide much information; and we drop these from the analysis of V_1 Doppler shifts. Among 165 single-component fits, we find significant blueshifts, $V_1/\delta(V_1) \leqslant -3$, for 35 spectra and significant redshifts, $V_1/\delta(V_1) \geqslant 3$, for 11 spectra.[12] When the significance of the Fe II Doppler shift is greater than 3σ, we list the properties of the galaxy in Table 2. Table 3 and Table 4, respectively, list the fitted Doppler shifts (Column 5) for these outflows and inflows as well as the Fe II λ2374 equivalent widths (Column 2) and upper limits on the Fe II λ2261 equivalent widths (column 3)

3.3.2. Two-component Fits Illustrating ISM Absorption at the Systemic Velocity

Having identified bulk outflows and inflows with the single-component fitting, we next model the contribution of the ISM (at

[12] As discussed further in Section 6, two of the inflows are not significant due to systematic errors.

Table 2
Properties of Galaxies with Net Fe II Doppler Shifts

Object (1)	Grism ($1\,\mathrm{mm}^{-1}$) (2)	SNR (3)	Redshift Source (4)	z (5)	$M_B - 5\log h$ (AB mag) (6)	$U-B$ (7)	$\log M_*$ ($M_\odot$) (8)	SFR ($M_\odot\,\mathrm{yr}^{-1}$) (9)
12008197	400	12.2	L	0.9802	−21.19	0.804	10.63†	98
12008550	400	9.86	L	1.3024	−21.22	0.620	10.08†	25
12011836	400	9.38	L	0.9270	−19.90	0.579	10.26†	14
12012777	400	11.68	L	1.2742	−21.06	0.516	10.11†	23
12013242	400	8.83	L	1.2867	−21.31	0.450	10.19	26
12011428*	400	4.6	L	1.2840	−19.87	0.180	9.65	9
12015177	600	5.3	L	0.9860	−20.23	0.487	9.69	12
12016019*	400	11.57	L	1.0846	−20.71	0.622	10.03†	19
12019542	600	3.73	D	1.2784	−21.68	0.705	10.40†	40
12019962*	400	10.1	L	0.6444	−19.22	0.458	9.77†	2
12019996*	400	7.36	L	1.2812	−21.71	0.634	10.67†	43
12100420*	400	8.60	L	1.1995	−20.63	0.601	10.01†	10
22004858*	400	15.00	L	1.2686	−21.84	0.624	10.54	...
22005216	400	9.27	L	0.9130	−19.49	0.556	9.59	...
22005270*	400	10.57	L	0.8308	−20.38	0.710	10.40	...
22006172	400	10.65	L	0.8328	−21.10	0.707	10.65	...
22006207	400	9.42	L	1.2709	−20.59	0.419	9.88	...
22029066	600	10.45	L	0.7852	−21.59	0.891	11.29†	...
22029224	600	8.66	L	0.8603	−20.90	0.611	10.27	...
22036854	600	7.29	L	0.9373	−20.85	0.564	10.32	...
22036912	600	6.66	L	0.8099	−21.02	0.864	10.86	...
32010773	600	9.23	L	0.8039	−19.91	0.234	9.60†	...
32011098	600	5.01	L	0.9561	−20.22	0.546	9.77†	...
32011099	600	6.51	L	0.8832	−20.06	0.492	9.80	...
32011192	600	9.51	L	0.8478	−20.60	0.587	10.07†	...
32011682	600	8.79	L	0.8359	−20.36	0.511	10.23†	...
32016857	600	8.32	L	0.9391	−20.81	0.440	9.81†	...
32017112	600	5.85	L	1.0084	−20.89	0.665	10.23†	...
32020468*	400	3.16	L	1.2355	−21.00	0.734	10.28†	...
32022156	600	4.60	L	1.0434	−20.70	0.580	10.10†	...
42006781	400	10.98	D	1.2859	−20.74	0.546	9.68†	...
42006915	400	25.09	L	0.8945	−20.55	0.386	10.50†	...
42014101	400	8.39	L	0.7494	−20.47	0.899	10.94†	...
42014154	400	9.75	L	0.8427	−19.40	0.465	9.77†	...
42014585	400	8.17	D	1.2705	−20.91	0.588	10.18	...
42014618	400	17.64	L	1.0130	−20.37	0.592	9.81	...
42014718	400	9.21	L	1.1904	−21.27	0.692	10.85†	...
42014732	400	16.01	L	0.7502	−19.40	0.453	9.50†	...
42021266	400	11.66	L	0.9765	−19.63	0.616	9.50	...
42022173	400	8.15	D	1.3112	−20.25	0.324	9.68	...
42022307	400	20.72	D	1.2595	−21.43	0.466	10.22	...
42026243	400	3.30	L	1.3456	−21.66	0.667	10.88†	...
42033991	400	6.48	L	0.8714	−20.13	0.392	9.94†	...
42006875*	400	19.18	L	0.8696	−21.10	0.602	10.50†	...

Notes. (1) Object identification from DEEP2. The Fe II absorption in these spectra is Doppler shifted (relative to the galaxy) at a significance level greater than 3σ. Inflows (redshifts) are denoted by *; the objects 22028473 and 22036194 have been dropped per the discussion in Section 5.1. (2) Blue grism where 400 lines mm^{-1} and 600 lines mm^{-1} imply FWHM of 435 $\mathrm{km\,s}^{-1}$ and 282 $\mathrm{km\,s}^{-1}$, respectively. (3) Continuum SNR between 2400 and 2500 Å. (4) Source of redshift. The flag L/D indicates (L)RIS (the spectra presented here) or (D)EIMOS, DEEP2 redshift, respectively. (5) Redshift. (6) DEEP2 absolute magnitude (Willmer et al. 2006). (7) DEEP2 color (Willmer et al. 2006). (8) Stellar mass from SED fitting (Bundy et al. 2006). Galaxies with an SED fit that includes *K*-band photometry (most certain) are denoted by †; the other fits are based on *BRI* photometry. (9) Star formation rate derived from dust-corrected UV continuum luminosity and converted to a Chabrier initial mass function.

the systemic velocity) to obtain an estimate of the velocity that characterizes the absorption equivalent width produced by the bulk flow. In spectra of nearby star-forming galaxies, interstellar gas is generally the primary source of absorption in resonance lines near the systemic velocity (Heckman et al. 2000; Martin 2005, 2006; Rupke et al. 2005; Sato et al. 2009). Stronger interstellar absorption at the systemic velocity is observed toward low-redshift galaxies with higher inclinations (Chen et al. 2010). In these resonance lines, the equivalent width of the interstellar absorption only becomes weaker than the stellar photospheric absorption in post-starburst galaxies, which can be recognized by the presence of absorption lines from excited states that are populated in photospheres but not in diffuse gas. For our purposes here, we will use the term *maximum interstellar*

Table 3
Outflow Properties

Object (1)	$W(2374)$ (Å) (2)	$W(2261)$ (Å) (3)	$\log[N(\mathrm{Fe}^+)C_f]$ (cm^{-2}) (4)	V_1 ($\mathrm{km\,s^{-1}}$) (5)	b_{ISM} ($\mathrm{km\,s^{-1}}$) (6)	V_{DOP} ($\mathrm{km\,s^{-1}}$) (7)	$\log[N_{\mathrm{ISM}}(\mathrm{Fe}^+)C_f]$ (cm^{-2}) (8)	$\log[N_{\mathrm{DOP}}(\mathrm{Fe}^+)C_f]$ (cm^{-2}) (9)	$V_{\max}(\lambda 2374)$ ($\mathrm{km\,s^{-1}}$) (10)	$V_{\max}(\lambda 2796)$ ($\mathrm{km\,s^{-1}}$) (11)
12008197	1.21 ± 0.23	0.21	14.89–15.75	-62 ± 19	126	-93 ± 43	14.80–15.34	14.58–15.93	...	-466 ± 120
12008550	1.05 ± 0.19	0.17	14.83–15.66	-145 ± 23	77	-322 ± 135	14.69–15.27	14.32–15.79	-547 ± 93	
12011836	2.14 ± 0.32	0.27	15.14–15.86	-128 ± 21	114	-465 ± 142	15.00–15.65	14.42–15.01	-697 ± 117	-667 ± 94
12012777	2.13 ± 0.19	0.18	15.13–15.68	-217 ± 13	95	-443 ± 70	15.07–15.89	14.79–15.59	-704 ± 122	-909 ± 146
12013242	1.14 ± 0.23	0.24	14.86–15.81	-73 ± 22	121	-97 ± 45	14.89–15.48	14.78–15.81	...	...
12015177	2.34 ± 0.32	0.33	15.17–15.94	-101 ± 18	91	-106 ± 49	14.95–15.64	14.72–15.77	-418 ± 51	...
12019542	0.72 ± 0.30	0.39	14.66–16.02	-183 ± 60^4	69	-311 ± 273	14.51–15.04	14.51–15.04	...	...
22005216	0.98 ± 0.26	0.25	14.80–15.82	-106 ± 28	59	-450 ± 146	14.90–15.76	14.20–14.66	...	-504 ± 56
22006172	1.57 ± 0.28	0.27	15.00–15.86	-112 ± 21	118	-95 ± 47	14.84–15.41	14.80–15.80	-588 ± 178	-514 ± 128
22006207	0.76 ± 0.15	0.16	14.69–15.63	-199 ± 39	76	-34 ± 35	14.57–15.11	14.68–16.06	-487 ± 84	-693 ± 94
22029066	1.85 ± 0.20	0.27	15.07–15.86	-62 ± 16	152	-209 ± 46	14.93–15.49	> 14.05	-396 ± 115	-919 ± 117
22029224	1.09 ± 0.19	0.22	14.84–15.77	-69 ± 16	117	-146 ± 53	14.81–15.37	14.37–14.94	...	-450 ± 39
22036854	2.08 ± 0.24	0.24	15.12–15.81	-91 ± 14	58	-121 ± 37	14.91–15.81	14.55–15.30	-444 ± 46	...
22036912	0.84 ± 0.21	0.34	14.73–15.96	-86 ± 16	167	-238 ± 87	14.80–15.29	14.14–14.49	-297 ± 53	-653 ± 58
32010773	0.63 ± 0.17	0.19	14.60–15.70	-197 ± 46	45	-189 ± 126	14.45–15.03	14.13–14.60	-511 ± 95	-703 ± 43
32011098	0.59 ± 0.31	0.33	14.58–15.94	-89 ± 29	87	-78 ± 101	14.54–15.04	14.56–15.57	...	...
32011099	1.79 ± 0.25	0.23	15.06–15.79	-46 ± 13	72	-97 ± 24	15.06–16.12	14.65–15.30	-356 ± 69	-463 ± 105
32011192	1.85 ± 0.19	0.22	15.07–15.77	-154 ± 9	97	-154 ± 38	14.96–15.65	14.74–15.30	-527 ± 86	-739 ± 74
32011682	1.30 ± 0.20	0.23	14.92–15.79	-85 ± 11	96	-246 ± 60	14.90–15.55	14.18–14.68	-317 ± 71	-521 ± 62
32016857	0.88 ± 0.18	0.20	14.75–15.73	-91 ± 15	97	-227 ± 82	14.75–15.32	14.42–15.53	-297 ± 84	...
32017112	1.25 ± 0.25	0.30	14.90–15.90	-80 ± 18	99	-255 ± 106	14.80–15.38	14.24–14.88	...	...
32022156	0.95 ± 0.34	0.43	14.78–16.06	-180 ± 48	74	-318 ± 182	14.82–15.49	14.41–14.98	-355 ± 42	-436 ± 27
42006781	2.07 ± 0.17	0.15	15.12–15.60	-70 ± 13	59	-143 ± 28	15.00–16.11	14.06–14.42	-565 ± 77	-495 ± 68
42006915	1.29 ± 0.10	0.097	14.92–15.41	-76 ± 10	206	-322 ± 75	14.67–15.08	13.91–14.03	-621 ± 117	-576 ± 91
42014101	1.08 ± 0.35	0.32	14.84–15.93	-150 ± 38	107	-281 ± 251	14.65–15.17	14.48–15.29	-514 ± 68	-480 ± 66
42014154	0.84 ± 0.22	0.25	14.73–15.82	-105 ± 30	63	-315 ± 163	14.77–15.46	13.93–14.42	...	...
42014585	1.63 ± 0.27	0.27	15.02–15.86	-177 ± 30	61	-297 ± 85	14.96–15.94	14.55–15.20	-579 ± 155	-456 ± 47
42014618	1.29 ± 0.14	0.15	14.92–15.60	-76 ± 13	121	-115 ± 33	14.83–15.39	14.43–15.67	-548 ± 107	...
42014718	2.06 ± 0.31	0.30	15.12–15.90	-156 ± 19	199	-219 ± 77	14.96–15.49	14.84–15.90	-712 ± 216	-651 ± 128
42014732	0.91 ± 0.17	0.16	14.76–15.63	-81 ± 26	79	-52 ± 43	14.59–15.13	14.47–15.33	-450 ± 82	...
42021266	1.06 ± 0.20	0.19	14.83–15.70	-108 ± 24	76	-388 ± 152	14.75–15.37	14.28–15.26	-590 ± 163	...
42022173	0.81 ± 0.21	0.23	14.71–15.79	-134 ± 27	106	-125 ± 85	14.67–15.20	14.70–15.85	...	...
42022307	1.15 ± 0.09	0.10	14.87–15.43	-146 ± 10	165	-381 ± 79	14.71–15.18	14.20–14.66	-554 ± 62	-529 ± 50
42026243	...	0.70	$\cdots -16.27$	-302 ± 38	93	-476 ± 201	15.17–16.22	15.03–16.29	...	-843 ± 135
42033991	1.39 ± 0.46	0.40	14.95–16.03	-139 ± 41	132	-369 ± 319	14.69–15.19	14.52–15.36	-466 ± 136	...

Notes. (1) DEEP2 survey identification. (2) Rest-frame equivalent width of Fe II 2374 absorption from direct integration of the trough. Error estimated from bootstrap resampling. (3) Upper limit (1σ) on Fe II 2261 equivalent width. Computed from an assumed line width that is twice the FWHM of the line response function and the continuum S/N. (4) Limits on Fe II column density for a fiducial covering factor of $C_f = 1$. For optically thin absorption, the linear portion of the curve of growth gives $N(\mathrm{Fe\,II}) = 6.40 \times 10^{14}\,\mathrm{cm}^{-2} W_{2374}$, which we adopt as a lower bound. We derive an upper bound, $N(\mathrm{Fe\,II}) = 9.06 \times 10^{15}\,\mathrm{cm}^{-2} W_{2261}$, by taking the 3σ upper limit on the Fe II 2261 equivalent width. (5) Doppler shift of the single velocity component model fitted to Fe II absorption as described in Section 3.3. (6) Doppler parameter of the systemic component in the two-component fits to the Fe II series. We adopt characteristic velocities of gas in the galaxy as probed by cooling radiation from H II regions. Specifically, we require the FWHM of the absorption optical depth profile match that of [O II] measured previously by Weiner et al. (2006), which gives $b_{\mathrm{sys}} = \sqrt{2}\sigma([\mathrm{O\,II}])$. (7) Doppler shift of the *Doppler component* fitted to Fe II lines in two-component model described in Section 3.3.2. (8) Limits on Fe II column density of ISM component in two-component fits. The model line profile for Fe II 2261 and 2374 was integrated and the above formulae, from table note #4, applied. (9) Limits on Fe II column density of Doppler component in two-component fits. The model line profile for Fe II 2261 and 2374 were integrated and the above formulae, from table note #4, applied. (10) Velocity of maximum Fe II 2374 absorption for $I + \delta(I) = 1$. (11) Velocity of maximum Mg II 2796 absorption for $I + \delta(I) = 1$.

component in the broadest sense to represent all absorption at the systemic velocity, possibly including some contribution from stellar photospheres.

We modeled the Fe II series, again excluding the λ2383 and λ2600 lines due to emission filling, using two velocity components—a *systemic component* with no Doppler shift and a *Doppler component* with a fitted velocity, V_{Dop}. Since the absorption troughs are not well resolved, we found that five parameter fits allow many degenerate solutions. To produce meaningful Doppler velocities, we fixed the width of the systemic component. Because the systemic component represents interstellar gas, we set its Doppler parameter to be consistent with the measured velocity dispersion of nebular gas previously fitted to the [O II] doublet. These photoionized, emission regions are believed to reside in a gaseous disk; and their velocity dispersions have been directly measured from the [O II] λλ3726, 29 doublet. The doublet is resolved in the 831 mm^{-1} (red channel) spectra, and the fitted Gaussian σ has been corrected for instrumental broadening. We choose $b_{\mathrm{sys}} = \sqrt{2}\sigma([\mathrm{O\,II}])$. We then fitted the maximum interstellar absorption to the Fe II series by varying the optical depth at line center, obtaining the deepest absorption trough at $v = 0$ consistent with the data. With the

Table 4
Inflow Properties

Object (1)	$W(2374)$ (Å) (2)	$W(2260)$ (Å) (3)	$\log[N(\mathrm{Fe}^+)C_f]$ (cm^{-2}) (4)	V_1 ($\mathrm{km\,s^{-1}}$) (5)	b_{ISM} ($\mathrm{km\,s^{-1}}$) (6)	V_{DOP} ($\mathrm{km\,s^{-1}}$) (7)	$\log[N_{\mathrm{ISM}}(\mathrm{Fe}^+)C_f]$ (cm^{-2}) (8)	$\log[N_{\mathrm{DOP}}(\mathrm{Fe}^+)C_f]$ (cm^{-2}) (9)	$V_{\max}(\lambda 2374)$ ($\mathrm{km\,s^{-1}}$) (10)	$V_{\max}(\lambda 2382)$ ($\mathrm{km\,s^{-1}}$) (11)
12011428	2.14 ± 0.48	0.44	15.1–16.0	154 ± 32	86	392 ± 124	15.14–16.19	14.71–15.49	416 ± 0.9	523 ± 0.1
12016019	2.44 ± 0.20	0.19	15.1–15.7	48 ± 14	97	258 ± 40	15.17–16.15	>13.58	655 ± 34	723 ± 0.6
12019962	1.88 ± 0.34	0.32	15.0–15.9	104 ± 31	113	122 ± 97	14.68–15.20	13.86–15.15	621 ± 9	472 ± 1
12019996	1.69 ± 0.31	0.30	15.0–15.9	117 ± 24	158	386 ± 138	14.92–15.47	14.56–15.57	510 ± 3	577 ± 5
12100420	1.86 ± 0.28	0.26	15.0–15.8	71 ± 18	109	190 ± 45	15.14–15.98	14.37–14.82	539 ± 1	641 ± 1
22004858	1.94 ± 0.14	0.14	15.0–15.6	61 ± 11	151	71 ± 18	15.03–15.63	14.76–15.53	...	737 ± 2
22005270	0.98 ± 0.23	0.25	14.8–15.8	401 ± 43	145	505 ± 588	14.39–14.71	14.37–14.81	546 ± 2	724 ± 9
32020468	2.36 ± 0.69	0.62	15.1–16.2	123 ± 39	95	164 ± 79	15.21–16.33	14.82–15.97	465 ± 1	311 ± 3
42006875	1.01 ± 0.12	0.12	14.8–15.5	51 ± 14	62	256 ± 50	14.87–15.66	13.86–14.21	...	663 ± 3

Notes. (1) DEEP2 survey identification. (2) Rest-frame equivalent width of Fe II 2374 absorption from direct integration of the trough. Error estimated from bootstrap resampling. (3) Upper limit (1σ) on Fe II 2261 equivalent width. Computed from an assumed line width that is twice the FWHM of the line response function and the continuum S/N. (4) Limits on Fe II column density for a fiducial covering factor of $C_f = 1$. For optically thin absorption, the linear portion of the curve of growth gives $N(\mathrm{Fe\,II}) = 6.40 \times 10^{14}\,\mathrm{cm}^{-2} W_{2374}$, which we adopt as a lower bound. We derive an upper bound, $N(\mathrm{Fe\,II}) = 9.06 \times 10^{15}\,\mathrm{cm}^{-2} W_{2261}$, from the 3σ upper limit on the Fe II 2261 equivalent width. (5) Doppler shift of the single velocity component model fitted to Fe II absorption as described in Section 3.3. (6) Doppler parameter of the systemic component in the two-component fits to the Fe II series. We adopt characteristic velocities of gas in the galaxy as probed by cooling radiation from H II regions. Specifically, we require the FWHM of the absorption optical depth profile match that of [O II] measured previously by Weiner et al. (2006), which gives $b_{\mathrm{sys}} = \sqrt{2}\sigma([\mathrm{O\,II}])$. (7) Doppler shift of the *Doppler component* fitted to Fe II lines in two-component model described in Section 3.3.2. (8) Limits on Fe II column density of ISM component in two-component fits. The model line profile for Fe II 2261 and 2374 was integrated and the above formulae, from table note #4, applied. (9) Limits on Fe II column density of Doppler component in two-component fits. The model line profile for Fe II 2261 and 2374 were integrated and the above formulae, from table note #4, applied. (10) Velocity of maximum Fe II 2374 absorption for $I + \delta(I) = 1$. (11) Velocity of maximum Mg II 2796 absorption for $I + \delta(I) = 1$.

interstellar component now fully specified, we next fitted the Doppler shift, Doppler parameter, and central optical depth of the Doppler component.

This two-component fitting approach has two critical advantages over simply reflecting the redshifted portion of the fitted absorption trough to create a model of the systemic absorption, as implemented for example by Weiner et al. (2009). First, it does not require fully resolved troughs because the model is convolved with the instrumental response. Second, it can be used to estimate the effect of the ISM on the inferred velocity of redshifted absorption (gas inflows) as well as blueshifted absorption (gas outflows). We only fit two components when the single-component fit indicated a significant outflow or inflow. The low resolution of our spectra does not constrain the two-component fits well enough to use them to determine whether the spectrum shows a net flow in the first place.

Figure 4 shows examples of the two-component fits relative to the single-component fits. The V_{Dop} velocity from the two-component fit is bluer than the single-component Doppler shift V_1, but the difference is typically less than the error bar δV_1. The maximum single-component blueshift is $-330\,\mathrm{km\,s^{-1}}$; but the blueshift of the Doppler component reaches $-550\,\mathrm{km\,s^{-1}}$ in the two-component fits. This trend is consistent with that shown in Coil et al. (2011), where the impact of the systemic component on the outflow velocity is quantified. While the one- and two-component fits yield consistent outflow velocities for many spectra, there is a subset for which accounting for a symmetric absorption component at the systemic velocity significantly increases the estimated outflow velocity. It is therefore of interest to understand which galaxies have this stronger interstellar absorption component.

The equivalent width of the systemic component rises strongly with increasing stellar mass. Hence modeling the systemic component results in fitted outflow velocities about 200–300 $\mathrm{km\,s^{-1}}$ bluer regardless of whether the systemic absorption is strong or weak. Only the most massive galaxies in our sample, however, exhibit exceptionally strong interstellar absorption with $W_{\mathrm{sys}} \gtrsim 2.3$ Å. In this paper, we use the V_1 values to determine whether a net flow is present; and, when it is, we use the values of V_{Dop} and W_{sys} to illustrate how the interstellar absorption at the systemic velocity may influence the conclusions drawn from the single-component fits. Columns 6 and 7 of Tables 3 and 4 compile the Doppler parameters derived for the systemic components and the fitted values of the Doppler shifts, V_{Dop}.

3.3.3. Equivalent Widths and Ionic Column Density

In general, the *intrinsic* equivalent width of each Fe II line in a spectrum is determined by a combination of the ionic column density, $N(\mathrm{Fe}^+)$, and the Doppler parameter, b, called the curve of growth (Spitzer 1978). The equivalent width of optically thin transitions is sensitive to Fe II column density, but the equivalent width of optically thick transitions depends primarily on the velocity spread of the absorbing gas. The measured equivalent widths do not necessarily follow this theoretical curve of growth, however, because emission filling reduces the intrinsic area of each absorption trough in a given spectrum by a different amount. Here we discuss the measured equivalent widths of a line not affected much by emission filling, Fe II $\lambda 2374$, and the upper limit on the equivalent width of a weak line, Fe II $\lambda 2261$, detected in composite spectra. Since the Fe II 2261 transition has an oscillator strength 12.8 times lower than that of Fe II 2374, the equivalent width measurement and upper limit together constrain the ionic column density to order-of-magnitude accuracy.

How accurately the ionic column density can be estimated from a single line depends on the optical depth of the transition. The column density at which the absorbing gas becomes optically thick, i.e., $\tau(\lambda) \equiv 1$, depends on the absorption cross section. At line center, the optical depth can be expressed as

$$\tau_0 = 1.498 \times 10^{-15} \lambda_0 f N C_f b^{-1}, \quad (7)$$

where f denotes the oscillator strength of the transition, the wavelength of the transition is in Å, the column density has units of cm^{-2}, and the Doppler parameter is in $\mathrm{km\,s}^{-1}$. To illustrate how partial covering of the continuum source affects the inferred ionic column density, we include a covering factor, $0 < C_f \leqslant 1$, which describes the fraction of the continuum light covering by the absorbing clouds.

The rough equality of the equivalent widths of Fe II λ2344, λ2374, and λ2587 in many of the LRIS spectra indicates these transitions are typically optically thick. The intrinsic equivalent widths of these transitions therefore provide lower bounds on the ionic column density. Our measurement of the equivalent width for the transition with the lowest oscillator strength, Fe II λ2374, yields the best lower limit on $N(\mathrm{Fe}^+)$. In this optically thin limit, the linear relationship between equivalent width and ionic column yields a lower limit:

$$N(\mathrm{Fe}^+) \geqslant 6.30 \times 10^{14}\,\mathrm{cm}^{-2} W_{2374}(\text{Å}) C_{f,1}^{-1}, \tag{8}$$

where $C_{f,1}$ is the covering factor in units of $C_f = 1$. The summary of the outflow and inflow properties, Tables 3 and 4, respectively, provides these lower limits on $N(\mathrm{Fe}^+)C_{f,1}$ in Column 4 for the total absorption trough, in Column 8 for the interstellar component at the systemic velocity, and in Column 9 for the Doppler component.

The Fe II λ2261 absorption trough is generally much weaker than the Fe II λ2374 line, so we can be certain that the Fe II λ2261 transition falls on the linear part of the curve of growth. In individual spectra, we measure an upper limit on the equivalent width of Fe II λ2261. We place an upper bound on the ionic column density,

$$N(\mathrm{Fe}^+) \leqslant 9.06 \times 10^{15}\,\mathrm{cm}^{-2} [3\sigma(W_{2261})] C_{f,1}^{-1}, \tag{9}$$

where the 3σ upper limit on the equivalent width has units of Å. The summary of the outflow and inflow properties, Tables 3 and 4, respectively, provides these upper limits on $N(\mathrm{Fe}^+)C_{f,1}$ in Column 4 for the total absorption trough, in Column 8 for the interstellar component at the systemic velocity, and in Column 9 for the Doppler component.

3.4. Highest Velocity Mg II Absorption

Resonance emission is not expected to fill in the high-velocity wings of the intrinsic Mg II absorption profile (e.g., Figure 5 of Prochaska et al. 2011). If the gas column is low at high velocities we expect to detect Mg II absorption even though the Fe II absorption is too weak to detect for several reasons. First, consider equal column densities of Fe^+ and Mg^+. In the optically thin limit, the Fe II λ2374 equivalent width would be a factor of 20 lower than the intrinsic Mg II λ2796 equivalent width. Next, this equivalent width ratio could be higher because the cosmic abundance ratio of Mg to Fe is a factor of 1.2, and Fe is more depleted onto grains than is Mg (Savage & Sembach 1996). Finally, since the first and second ionization potentials of iron are similar to those of magnesium, we might expect Fe II and Mg II ions to be present in the same phase of the wind.[13] The column density ratios calculated from grids of photoionization models show, however, that the relative fraction of Fe and Mg in the singly ionized state is sensitive to the ionization parameter. Over the range of likely ionization parameters near galaxies, the Fe II column density can be similar to or significantly less than the Mg II column density (Churchill et al. 2003). Hence, the relative optical depths in Fe II λ2383 and Mg II λ2803 can be similar, but the Mg II optical depth can easily be much larger for a range of physical reasons.

3.4.1. Measurement Technique

The LRIS spectra of 186 of the 208 galaxies cover the Mg II doublet. In 57 spectra, no significant absorption trough was detected at a rest wavelength of 2796 Å; some of these spectra are characterized by strong Mg II emission that fills the absorption trough. Among the most prominent Fe II outflows, i.e., the 35 with 3σ outflows, 33 spectra provide Mg II coverage. We measured the properties of the Mg II absorption for composite spectra and 104 individual spectra excluding spectra that had weak λ2796 absorption or sky-subtraction artifacts near the doublet.

Some of the individual spectra show an Mg II profile with a blue wing. To characterize the minimum (maximum) velocity of the Mg II absorption, we measure the velocity, $V_{\max}$, blueward (or redward) of the systemic velocity at which the spectral intensity is consistent with the continuum level (at the 1σ level); specifically, we define $I(\lambda_{\mathrm{vmax}}) = 1 - \delta I(\lambda_{\mathrm{vmax}})$, where $\delta I(\lambda)$ is the error spectrum. To measure $V_{\max}$, we added a Gaussian random deviate to the original value of the intensity (with standard deviation matched to the error spectrum at each wavelength), remeasured the maximum velocity of the absorption trough in this modified spectrum, and calculated the average $V_{\max}$ and standard deviation after 1000 iterations. The statistical error was taken to be the standard deviation or half a pixel width, whichever was larger.

Clearly, this definition is only meaningful when the blue wing of the line profile is well resolved. Furthermore, comparisons of $V_{\max}$ must be made at similar spectral S/N. The Mg II λ2796 absorption trough provides our most sensitive measurement of $V_{\max}$ and is not blended with another transition. When the Fe II lines have a significant redshift, i.e., the nine inflow galaxies discussed in Section 6, we measure the maximum (inflow) velocity from the red wing of Mg II 2803; but this measurement can be affected by emission filling.

The absence of blue wings on line profiles in our LRIS spectra does not rule out the presence of an outflow due to sensitivity issues caused by instrumental smoothing and the variation in S/N among spectra. The $V_{\max}$ measurements should *not* be compared among the entire sample to determine which galaxies have outflows but do serve two useful purposes. First, values of $V_{\max}$ blueward of approximately $-435\,\mathrm{km\,s}^{-1}$ in 400 lines mm^{-1} spectra identify a resolved line wing, as does absorption blueward of roughly $-282\,\mathrm{km\,s}^{-1}$ in 600 lines mm^{-1} spectra. Second, we can compare the Mg II blue wings among galaxies with different properties by measuring the $V_{\max}$ feature in composite spectra constructed to have the same S/N. Previous studies have done this type of analysis at spectral resolution higher than our LRIS spectra (Weiner et al. 2009; Rubin et al. 2010b).

3.4.2. Contamination from Stellar Absorption

The analysis of both composite and individual presented in this paper excludes galaxies with colors placing them in the green valley or red sequence or K+A spectral classification. The LRIS spectra of many of these 22 galaxies show significant stellar absorption. The stellar lines become stronger with

[13] Their first and second ionization potentials are IP(Mg I) = 7.646 eV, IP(Mg II) = 15.035 eV, IP(Fe I) = 7.870 eV, and IP(Fe II) = 16.18 eV.

Table 5
Properties of Composite Spectra

Feature Spectrum (1)	V_1 (Fe II) (km s^{-1}) (2)	EW(λ2374) (Å) (3)	$V_{\max}$(Mg II) (km s^{-1}) (4)	EW(λ2796) (Å) (5)
Lowest mass ($8.85 \leqslant \log(M_*/M_\odot) < 9.85$)	-28 ± 8	1.26	-649 ± 86	0.61 ± 0.01
Intermediate mass ($9.85 \leqslant \log(M_*/M_\odot) < 10.35$)	-32 ± 6	1.47	-770 ± 103	1.40 ± 0.03
Highest mass ($10.35 \leqslant \log(M_*/M_\odot) \leqslant 11.29$)	-23 ± 8	1.59	-713 ± 119	1.63 ± 0.05
Bluest ($0.189 \leqslant U - B < 0.519$)	-32 ± 8	1.31	-693 ± 86	0.72 ± 0.02
Bluer ($0.519 \leqslant U - B < 0.662$)	-27 ± 6	1.48	-649 ± 91	1.17 ± 0.02
Blue ($0.662 \leqslant U - B \leqslant 0.907$)	-26 ± 7	1.52	-888 ± 173	1.85 ± 0.07
Lowest luminosity ($-17.67 \geqslant M_B - 5\log h > -20.03$)	-23 ± 9	1.19	-666 ± 88	0.72 ± 0.02
Intermediate luminosity ($-20.03 \geqslant M_B - 5\log h > -20.79$)	-18 ± 7	1.56	-667 ± 88	1.08 ± 0.01
Highest luminosity ($-20.79 \geqslant M_B - 5\log h > -22.19$)	-39 ± 6	1.65	-782 ± 92	1.79 ± 0.03
Lowest SFR ($0.86 \leqslant \mathrm{SFR}(M_\odot\ \mathrm{yr}^{-1}) < 12.24$)	26 ± 10	1.48	-629 ± 104	0.81 ± 0.04
Highest SFR ($12.24 \leqslant \mathrm{SFR}(M_\odot\ \mathrm{yr}^{-1}) < 97.81$)	-38 ± 8	1.47	-755 ± 91	1.88 ± 0.02
Lowest sSFR ($1.00 < \mathrm{sSFR}^{-1}(\mathrm{Gyr}) \leqslant 15.08$)	19 ± 10	1.55	-779 ± 136	1.59 ± 0.06
Highest sSFR ($0.178 < \mathrm{sSFR}^{-1}(\mathrm{Gyr}) \leqslant 1.00$)	-24 ± 9	1.41	-610 ± 81	0.92 ± 0.02
3σ Fe II outflow	-119 ± 6	1.47	-901 ± 99	1.59 ± 0.02
3σ Fe II inflow	95 ± 8	1.89	-559 ± 113	1.25 ± 0.07

Notes. Column 1: Subsample averaged together to form composite spectrum. Column 2: Doppler shift of the Fe II absorption measured as described in Section 3.3. Column 3: Equivalent width of the Fe II λ2374 absorption trough. Column 4: Maximum blueshift, $V_{\max}$, of Mg II λ2796 absorption measured as described in Section 3.4. Column 5: Equivalent width of the Mg II λ2796 trough from 0 to $V_{\max}$.

the mass of the intermediate age stellar population, so we recognized the contamination by comparing absorption features (from excited states rather than resonance transitions) in spectra of post-starburst galaxies to our spectra. The excited absorption features are absent or weak in our spectra of blue-cloud galaxies.

This rejection affects the measurement of the maximum absorption blueshift because the stellar line profiles have broad wings. We measure high $V_{\max}$ values for several of the 22 rejected galaxies. Because these galaxies are mostly in the high mass tertile of our sample, they generate a positive correlation between $V_{\max}$ and stellar mass when we include them. Without them, the maximum blueshift of the Mg II $\lambda\lambda$2796, 2803 absorption in Figure 3 does not vary significantly with stellar mass, B-band luminosity, or color.

In principle, broad stellar line profiles could be differentiated from outflowing gas by the symmetry of the former about the systemic velocity. In practice, however, the Mg II λ2803 line is filled in by resonance emission. In Figure 6, for example, visual comparison of the maximum blueshifted Mg II λ2374 and the maximum redshifted Mg II 2803 absorption, shows that the latter is often clearly affected by emission filling (e.g., in the cases 12012777, 22013210, and 32011682) leaving a significant excess of absorption on the blue side. Exceptions to this rule include the spectra of 22004858, 22005270, and 42014138, where the symmetry might be used to argue for broad, stellar wings on the line profile. A definitive answer requires fitting the spectra with stellar population models to determine the net difference in stellar ages and is beyond the scope of this paper. However, in general, we think it would be very hard to fill in the red wing from stellar absorption with resonance emission because the emission is narrow, unresolved in the LRIS spectra, while stellar absorption lines in single stellar population models have FWHMs depth of 7–8 Å (or more at ages greater than 1.4 Gyr) and broad wings on the line profile. Hence, it seems clear that high-velocity gas is required to produce the blue wings of many Mg II absorption profiles.

4. COMPARISON OF Mg II AND Fe II ABSORPTION TROUGHS

Composite spectra allow comparisons between subsets of galaxies at equal continuum S/N. Before considering individual spectra, it is useful to establish the overall trends between absorption properties and galaxy properties in composite spectra. Table 5 gives the velocity and equivalent width measurements for the composite spectra discussed below. To make the comparison between individual spectra more meaningful, we focus on 400 lines mm^{-1} (600 lines mm^{-1}) spectra with continuum S/N greater than 10 (7.7) in this section, excluding the 22 spectra with the strongest stellar absorption (based on their classification as K+A, red-sequence, or green-valley galaxies). Table 6 summarizes the correlations between the absorption measurements for these individual spectra and the galaxy properties.

4.1. Absorption Equivalent Widths

4.1.1. Composite Spectra

In Figure 3, we show composite spectra by tertiles in stellar mass, $U-B$ color, and rest-frame B-band luminosity. The equivalent width of the Mg II absorption increases quite strongly with stellar mass, redder color, and higher B-band luminosity. The lower Mg II equivalent width in the less massive, bluer, and intrinsically fainter galaxies appears to result largely from increased resonance emission filling in the absorption troughs. First, only the composite spectrum of the highest mass quartile of galaxies has a physical ratio of the λ2796 to λ2803 equivalent widths; composite spectra of the lower mass quartiles have larger equivalent widths in the transition with the lower oscillator strength. Second, the composite spectrum of the lowest masses shows a P Cygni emission line in the Mg II λ2796 transition. Third, toward lower mass and bluer color, the absorption is more suppressed in the red wing of Mg II λ2803 than it is in the blue wing of Mg II λ2796. Since models predict the strongest emission near (and redward of) the systemic velocity, this trend

Table 6
Correlations Among Properties of Individual Galaxies

Quantity	V_1(Fe II)	$W_{\lambda 2374}$	$W_{\lambda 2796}(V < 0)$	$V_{\max}$	$W_{\rm MgII}$
M_*	0.099 (1.21)[a]	0.139 (1.70)[a]	0.320 (1.87)[b]	−0.305 (1.78)[b]	0.493 (2.9)[b]
$M_B - 5\log h$	0.048 (0.58)[a]	−0.133 (1.62)[a]	−0.338 (1.97)[b]	0.097 (0.56)[b]	−0.495 (2.9)[b]
$U - B$	0.123 (1.50)[a]	0.116 (1.42)[a]	0.443 (2.58)[b]	−0.205 (1.20)[b]	0.685 (4.0)[b]
z	−0.054 (0.66)[a]	0.180 (2.20)[a]	0.066 (0.38)[b]	0.143 (0.84)[b]	0.401 (2.34)[b]
SNR	0.021 (0.26)[a]	−0.065 (0.80)[a]	−0.165 (0.96)[b]	−0.059 (0.34)[b]	−0.050 (0.29)[b]
V_1(Fe II)	...	0.221 (2.70)[a]	−0.1421 (0.83)[b]	0.160 (0.93)[b]	0.159 (0.92)[b]
$W_{\lambda 2374}$	0.221 (2.70)[a]	...	0.451 (2.63)[b]	−0.033 (0.19)[b]	0.410 (2.39)[b]
$V_{\max}$(Mg II)	0.160 (0.93)[b]	−0.033 (0.19)[b]	−0.451 (2.63)[b]	...	−0.302 (1.76)[b]
$W_{\lambda 2796}(V < 0)$	−0.142 (0.83)[b]	0.451 (2.63)[b]	...	−0.451 (2.63)[b]	0.717 (4.2)[b]
SFR	−0.225 (1.40)[c]	−0.005 (0.03)[c]	0.086 (0.19)[d]	0.257 (0.57)[d]	0.714 (1.60)[d]
sSFR	−0.257 (1.61)[c]	−0.079 (0.49)[c]	−0.257 (0.58)[d]	0.086 (0.19)[d]	0.314 (0.70)[d]

Notes. We computed the Spearman rank-order correlation coefficient, r_S, between the continuum S/N near Fe II and various galactic properties. To determine whether a significant correlation was present, we examined the variance in the sum-squared difference of ranks, D, which is approximately normally distributed as described in chapter 14 of Press et al. (1992). The value in parentheses is the number of standard deviations from the null hypothesis (no correlation between the two quantities).
[a] Sample of 150 blue-cloud galaxies with measured Fe II Doppler shift V_1.
[b] Sample of 35 high S/N spectra with measured maximum Mg II blueshift $V_{\max}$.
[c] Sample of 40 blue-cloud galaxies with measured Fe II Doppler shift V_1 and extinction-corrected, ultraviolet SFR.
[d] Sample of six high S/N spectra with measured $V_{\max}$(Mg II) and extinction-corrected, ultraviolet SFR.

is consistent with emission filling reducing the equivalent width and maximum absorption velocity of the red wing.

The Fe II multiplets in the left and center panels of Figure 3 also show the impact of increased emission filling at lower mass, bluer color, and fainter luminosities. In spectra of lower mass, bluer, and lower luminosity galaxies, the equivalent width of Fe II λ2383 decreases much more than that of Fe II λ2374. In contrast to what we observed, decreasing the Fe II column density would reduce the equivalent width of Fe II λ2374 faster than the Fe II λ2383 equivalent width because the Fe II λ2374 transition, due to its lower oscillator strength, becomes optically thin when $\tau_0(2383) \approx 10$.

In Figure 5 and in Kornei et al. (2012), we show composite spectra for galaxies with lower and higher SFRs. Robust SFRs have only been measured for the AEGIS subset of our sample, so the S/Ns of these composites are lower than those in Figure 3. The Mg II EW increases toward higher SFR. The equivalent width evidently increases more strongly with mass than with SFR, however, because the Mg II equivalent width declines with increasing specific SFR in the middle panel of Figure 5.

4.1.2. Individual Spectra

In Figure 6, we overlay the Fe II λ2374 and Mg II λ2796 absorption profiles. When the absorption troughs are weak, these line profiles can be indistinguishable as seen in the 12011364, 12017063, and 42013921 spectra. Among the better resolved line profiles, however, the absorption trough of the weaker transition (Fe II λ2374) is often deeper near the systemic velocity than the Mg II λ2796 trough. The prominent Mg II emission in spectra like 12012777, 22028686, 22036688, and 32011682 is clearly the reason why the Fe II trough is deeper. Hence, we argue that resonance emission is filling in the Mg II absorption troughs in spectra like 22004974, 42006915, and 42022307. To summarize, the most striking difference between the Fe II and Mg II line profiles is the paucity of Mg II absorption (relative to Fe II) near the systemic velocity, which we attribute in large part to emission filling.

Figure 7 shows the absorption equivalent widths measured in these individual spectra over the full range in stellar mass, color, and luminosity. As anticipated from our inspection of the composite spectra, the Mg II equivalent width measurements for individual spectra are also positively correlated with stellar mass, color, and blue luminosity. Among these trends, the correlation with color is both the most significant (2.58 standard deviations from the null hypothesis) and strongest (Spearman rank correlation coefficient of $r_S = 0.44$). The Mg II absorption equivalent width is significantly more correlated with these galaxy properties than is the Fe II λ2374 equivalent width; i.e., comparison of Columns 3 and 4 in Table 6 quantitatively confirms the impression obtained from the composite spectra in this regard. Even though the Mg II equivalent width is correlated with the Fe II equivalent width, the ratio $W(2796)/W(2374)$ increases toward redder, more massive galaxies.

In Column 2 of Table 6, we show that the Doppler shift of the Fe II absorption has a negative correlation with specific SFR. Since our sign convention assigns negative velocities to Fe II blueshifts, the Fe II absorption is more blueshifted in galaxies that are undergoing a more significant episode of star formation. This correlation with specific SFR supports the expectation that the blueshifts mark galactic outflows.

We might expect larger blueshifts to generate broader lines and therefore have larger Fe II equivalent width; but the measured correlation is in the opposite sense. The Doppler shift V_1 (from single-component fitting) is positively correlated with the Fe II λ2374 equivalent width—a trend that may arise, for example, from a significant interstellar absorption component at the systemic velocity. It is certainly more difficult to detect a blueshifted component if the ISM absorption at the systemic velocity is strong.

4.1.3. Implications of Emission Filling

We have presented evidence for increased emission filling in lower mass, lower luminosity, bluer galaxies. These trends may be attributed to dust attenuation because, on average at least, the more massive and redder galaxies are dustier than the lower mass and bluer galaxies. Scattered photons absorbed by dust grains will not emerge from the galaxy, and we observe absorption troughs which are less affected by resonance emission in spectra of higher mass galaxies.

Dust is not required, however, to reduce emission filling. Indeed, we find examples of good agreement between the shape of the Mg II and Fe II absorption troughs (i.e., low emission filling) among individual spectra from galaxies with a wide range of properties. Viewing geometry is another way to select for (or against) emission. The line emission is weaker (and emission filling is reduced) in more collimated outflows, where the half-opening angle of the outflow cone is 45°, for example, than a spherical outflow (Prochaska et al. 2011). Adding absorption from the ISM to the radiative-transfer calculation also reduces the number of resonance-line photons in the emergent spectrum. The increased photon trapping in the ISM gives each continuum photon absorbed in an Fe II resonance transition more chances to escape the galaxy as fluorescent emission, thereby reducing the resonance emission and leaving an observed absorption trough similar to the intrinsic absorption profile.

4.2. Identifying Fast Outflows with Mg II Absorption

In some spectra, such as 22013210, 22029066, and 32011682, the Mg II absorption is detected to significantly higher blueshifts than is Fe II. At the same time, the maximum blueshifts of the Mg II and Fe II absorption are consistent in many spectra even though W(Mg II2796) $\gg$ W(Fe II2374), e.g., 12008197, 22004858, 22012723, and 42006781. Overall, we find no significant correlations between $V_{\rm max}$ and mass ($r_s = -0.31$; 1.8σ) or color ($r_s = -0.21$; 1.2σ) among the individual spectra, consistent with the lack of any trend in the composite spectra constructed by these galaxy properties. In addition, the Fe II Doppler shift is not significantly correlated with $V_{\rm max}$(Mg II); and V_1(Fe II) has the stronger correlation with SFR and specific SFR. We summarize our observations as follows: (1) nearly all of the high S/N spectra show a blue wing indicating outflowing material; and (2) spectra with a blueshifted Fe II centroid usually show Mg II absorption at highly blueshifted velocities; but (3) roughly half of the spectra with Mg II absorption at a large blueshift do not show a net blueshift of the centroid of the Fe II absorption.

Among the high S/N spectra, the equivalent widths of the Mg II absorption troughs tend to be larger when the absorption extends to higher blueshifts ($r_s = -0.45$ at 2.64σ in Table 6). We measured the Mg II λ2796 equivalent width by integrating the line profile from the systemic velocity blueward 1000 km s^{-1}. Defined this way, the equivalent width ranged from 0.25 to 1.0 times the total equivalent width integrated over the emission and absorption in both transitions. For the purpose of measuring the outflow equivalent width, and velocity range, this definition mitigates the impact of emission filling allowing a more direct comparison among spectra. For optically thick lines, the positive correlation between equivalent width and $V_{\rm max}$ requires either larger spreads in velocity along the sightline (e.g., more clouds or gas acceleration) or higher gas covering fractions when extremely blueshifted absorption is detected.

Figure 6 compares the Mg II and Fe II line profiles in spectra with high continuum S/N. Most galaxies with 3σ blueshifts of the Fe II lines show a resolved blue wing on the Mg II profile. The blue wing in these spectra is typically detected in Mg II to velocities more than twice the fitted single-component Fe II velocity. In spectra where the $V_{\rm max}$(Mg II) and V_1(Fe II) measurements differ, the Mg II λ2796 absorption is detected to larger blueshifts, as expected at low gas column densities. It is difficult to determine, however, whether the Fe II centroid fitting fails to identify some galaxies with outflowing gas. Some spectra, for example, have a well-detected blue wing of Mg II even though the centroids of their Fe II profiles do not show a significant outflow; these include seven among the nine 3σ-inflow galaxies whose spectra will be discussed in a Section 6. In the absence of broad line wings from stellar absorption, measurements of this maximum absorption velocity, $V_{\rm max}$, may be more directly related to the physical speeds in galactic outflows than the centroid of the Mg II absorption trough.

Among the composite spectra shown in Figure 3, the wavelengths where the Fe II absorption troughs meet the continuum do not vary with stellar mass, B-band luminosity, color, SFR, or specific SFR. In Table 5, the most significant change in $V_{\rm max}$(Mg II) is with the Doppler shift of the Fe II absorption. A composite spectra built from individual spectra with significant (3σ) Fe II absorption blueshifts show Mg II absorption at larger blueshifts than does the typical spectrum with redshifted Fe II absorption. In the bottom panel of Figure 5, we show the Mg II absorption at large blueshifts in the composite spectrum constructed from the individual spectra with the most significant Fe II outflows. The composite spectrum of the 3σ outflow galaxies has an Fe II Doppler shift of -119 ± 6 km s^{-1}. This outflow composite shows Mg II absorption out to -901 ± 99 km s^{-1}. The $V_{\rm max}$(Mg II) of the outflow composite is higher than that of the mass or luminosity composites, so we argue that (at least among star-forming galaxies) higher velocity outflowing gas is the most likely reason for the blue wings on the Mg II profiles. In Kornei et al. (2012), we further show that $V_{\rm max}$(Mg II) becomes more blueshifted in composite spectra as the surface density of star formation increases.

5. GAS OUTFLOWS

Resonance absorption lines from Mg II and Fe II are the primary near-UV spectral diagnostics of galactic outflows. At spectral resolutions of a 285–435 km s^{-1}, we can robustly measure the Doppler shifts and equivalent widths of the absorption troughs in nearly all spectra. A net blueshift of the transitions that decay primarily by fluorescence, V_1(Fe II), best identifies net outflows of low-ionization gas. The maximum blueshift of the absorption in the strongest line, Mg II λ2796, provides a complementary diagnostic of the outflow when spectrally resolved.

To describe the demographics of outflows in Section 5.1, we introduce a methodology for computing the fraction of spectra showing blueshifted Fe II absorption or blue absorption wing in Mg II and examine how the outflow fraction varies with galaxy properties. We then discuss the outflow properties and how they depend on galaxy parameters in Section 5.2, and Section 5.3, respectively.

5.1. Demographics of Outflow Galaxies

Since blueshifts mark gas with a net outflow relative to the stellar system, we want to compute the fraction of galaxies with Fe II blueshifts in order to determine which galaxies host outflows. The challenge is that a blueshifted line detected in a high quality spectrum is not necessarily detectable in a lower quality spectrum. We illustrate this problem in Section 5.1.1 and introduce a statistical method for quantifying the prevalence of outflows in the Appendix. We discuss the results in Section 5.1.2.

5.1.1. Fraction of Galaxies with Net Flows

Figure 8 shows a histogram of continuum S/N. As anticipated, at increased spectral S/N, a higher fraction of net

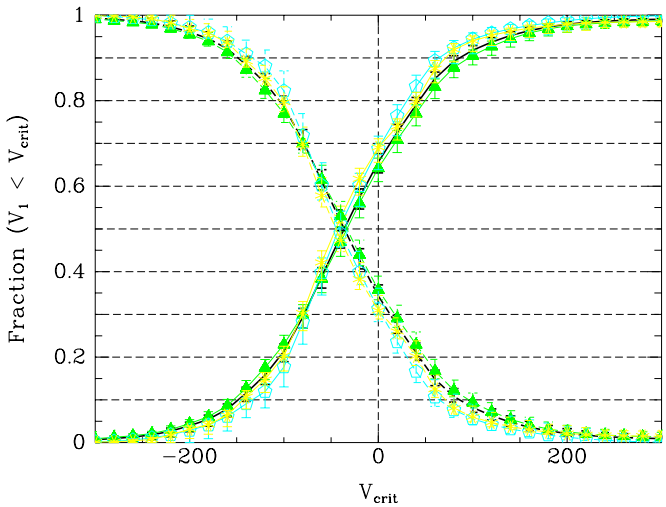

Figure 9. Fraction of spectra with a net Doppler shift of the Fe II absorption lines (relative to nebular emission lines). The solid lines show the fraction of blueshifted spectra with $V_1 < V_{\rm crit}$; and the dashed lines illustrate the complementary quantity, the fraction of galaxies with $V_1 > V_{\rm crit}$. The black, green (solid triangles), cyan (open pentagons), and yellow (asterisk) curves show the results of the calculation defined in the Appendix for the following four subsamples, respectively: all spectra, all 400 lines mm^{-1} spectra, all 600 lines mm^{-1} spectra, and the highest quality spectra defined as S/N > 8.5(6.5) for 400 lines mm^{-1} (600 lines mm^{-1}). The dominance of net blueshifts (65%) over spectra with redshifted absorption (35%) is apparent at $V_{\rm crit} = 0$; and the fraction of galaxies with $V_1 < V_{\rm crit}$ (solid line) rises steadily as the threshold speed for an outflow decreases. The curves for the four subsamples agree within the error bars showing the 68.27% confidence interval. This method of calculation does a good job of correcting for variations in spectral S/N and resolution allowing us to further examine the influence of galaxy properties on the fraction of spectra with Doppler-shifted absorption lines.

(A color version of this figure is available in the online journal.)

outflow (and inflow) galaxies are detected. The continuum S/N is not significantly correlated with *B*-band luminosity, stellar mass, color, or SFR; hence spectral sensitivity rather than galaxy properties shapes this growth in the outflow fraction. The continuum S/N is anti-correlated with the apparent *B* magnitude of the galaxy (4σ deviation from the null hypothesis), but the correlation is not very strong (correlation coefficient $r_S = -0.32$) for two reasons: the galaxies have a range of sizes, and the observations were obtained under a wide range of conditions. Since the sample selection was by apparent magnitude, the anti-correlation between S/N and redshift is not very significant.

Sensitivity to Doppler-shifted absorption also depends on spectral resolution and the strength of ISM absorption. At the same S/N (per pixel), a 600 lines mm^{-1} spectrum is more likely to yield a net Doppler shift than a 400 lines mm^{-1} spectrum because the uncertainty in the line centroid is smaller at higher resolution as described in Section 2.2.1. In addition, high equivalent width absorption at the systemic velocity will reduce the Doppler shift of the fitted, single velocity component. In practice, we cannot measure the outflow/inflow fraction at Doppler shifts less than $|V_1| < 41$ km s^{-1} due systematic errors described previously in Section 2.2.1. Focusing our analysis on these larger Doppler shifts largely removes any dependence on spectral resolution.

In the Appendix, we describe a methodology for calculating outflow fraction that takes into account the detection biases introduced by the variations in S/N and resolution among our spectra. Rather than arbitrarily picking a minimum Doppler shift to define an outflow, we consider *threshold velocities* ranging from the largest blueshift measured down to the minimum Doppler shift that we can reliably measure, roughly 41 km s^{-1}. We assign to each spectrum a probability that the Doppler shift of the low-ionization gas is larger than a threshold velocity. Finally, we obtain the outflow fraction for that threshold velocity by averaging these probabilities over the entire sample computing the uncertainty directly from the probability distribution. This definition of outflow fraction is quite general and can be applied under a broad range of circumstances. For example, the Doppler shift may represent the fitted Fe II centroid velocity V_1, the Doppler shift of the blue wing of the Mg II absorption trough $V_{\rm max}$, or the velocity derived from a more complex model. This methodology can also be applied to describe the inflow fraction if we use the net Doppler shift or velocity of the red wing of a line profile.

In Figure 9, we show the outflow and inflow fractions computed for four samples. Roughly 5%, 20%, and 45% of the spectra in our full sample (black lines) show Fe II blueshifts faster than -200 km s^{-1}, -100 km s^{-1}, and -50 km s^{-1}, respectively. In contrast, less than 8% of the spectra have redshifts higher than 90 km s^{-1}. Repeating the analysis with just the highest S/N spectra (yellow lines), we obtain the same result. Similarly, with the sample restricted to either the lower resolution (400 lines mm^{-1}) spectra or the higher resolution (600 lines mm^{-1}) spectra, the outflow fraction remains consistent with the results obtained for the full sample. This test demonstrates that our results for the outflow fraction are insensitive to S/N and spectral resolution. Because many more of the LRIS spectra have blueshifts than redshifts, the results for the outflow fraction are better constrained (than for inflow) and we describe the outflow results in Section 5.1.2.

5.1.2. Dependence of Outflow Fraction on Galaxy Properties

We apply the computational method introduced here to compare the outflow fraction among galaxies with different properties. We divide our sample into tertiles (thirds) by redshift, mass, color, luminosity, and SFR. To obtain insight about the importance of starbursts, we also normalize the SFR by the stellar mass; this specific SFR is the reciprocal of the timescale required to assemble the stellar mass at the current SFR. We present the fraction of galaxies with a blueshifted Fe II centroid velocity and then compare to the fraction of galaxies with significant blue absorption wings in Mg II. It is important to keep in mind that all the galaxies in our sample are star-forming galaxies; the post-starburst, green-valley, and red-sequence galaxies are excluded from this analysis.

The galaxy properties measured for DEEP2 galaxies were a primary motivation for our study. Stellar mass is perhaps the most fundamental property measured for the entire sample; and relative masses are determined to within a factor of two (Bundy et al. 2006). Measurements of *B*-band luminosity and $U-B$ color are described in Willmer et al. (2006) for the full sample. SFRs have been measured for 51 galaxies in our LRIS sample. In Kornei et al. (2012), we show that these extinction-corrected SFRs (derived from *GALEX* imaging of the AEGIS field) agree with the sum of the SFRs derived from uncorrected UV and 24 μm photometry.

In Figure 10, we show the fraction of spectra with V_1 bluer than $V_{\rm crit}$. The outflow fraction measured this way is clearly independent of stellar mass. The outflow fraction is enhanced among galaxies in the highest tertile by SFR (relative to the lowest tertile). The largest variation with galaxy properties, however, is seen between the tertiles with the highest and lowest specific SFRs. Outflows faster than roughly 100 km s^{-1} are

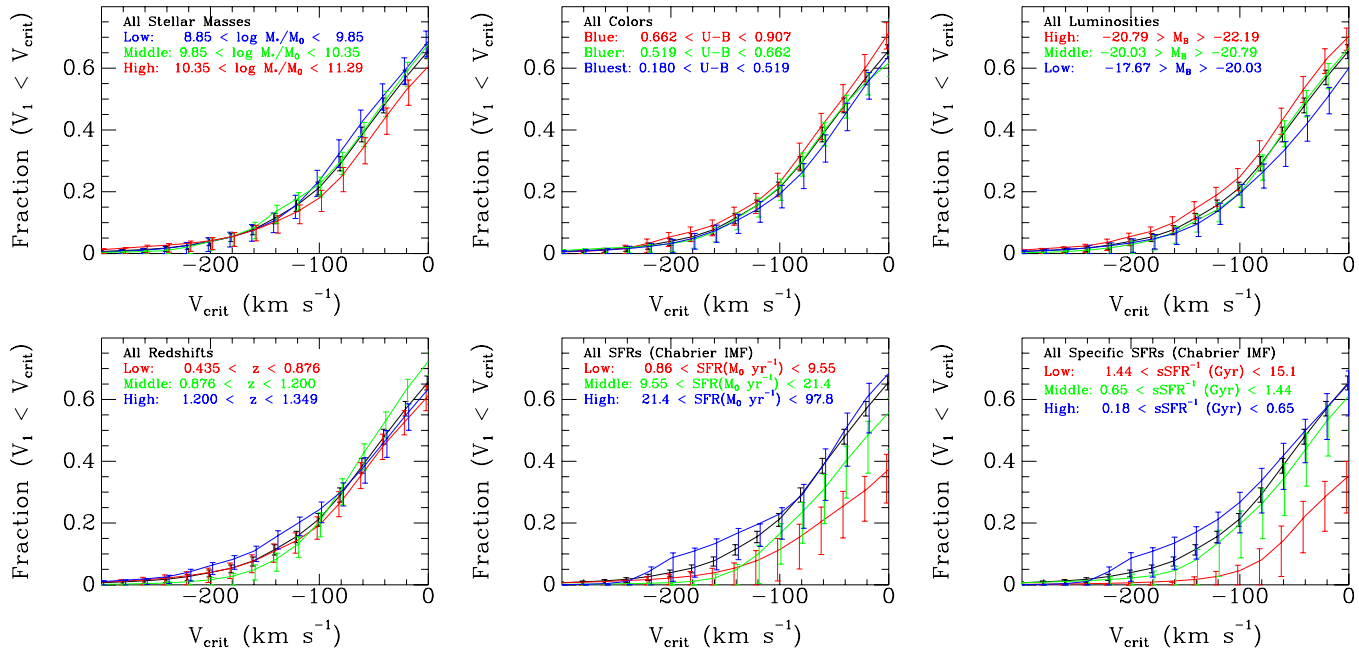

Figure 10. Fraction of galaxies with V_1 bluer than $V_{\rm crit}$. This measure of the outflow fraction shows no dependence on stellar mass (upper left) or color (upper middle). The outflow fraction is slightly higher among higher luminosity galaxies (middle left) and higher redshift galaxies (middle right). Over the velocity range $-180 < V_1(\mathrm{kms}^{-1}) < -100$, the outflow fraction among the galaxies in the highest SFR tertile ($21 < \mathrm{SFR}(M_\odot\,\mathrm{yr}^{-1}) < 98$) is about a factor of four higher than the outflow fraction measured among the galaxies in the lowest SFR tertile ($0.9 < \mathrm{SFR}(M_\odot\,\mathrm{yr}^{-1}) < 10$). Among the galaxies with the lowest specific star formation rates ($-10.2 < \log \mathrm{sSFR}(\mathrm{yr}^{-1}) < -9.16$), outflows appear to be strongly suppressed at all velocities relative to the average. The outflow fraction is enhanced by a factor of 1.8 over the average among the tertile of galaxies with the highest sSFRs ($-8.82 < \log \mathrm{sSFR}(\mathrm{yr}^{-1}) < -8.25$). The calculation of the outflow fraction follows the methods outlined in the Appendix.

nearly absent at low specific SFR, $-10 < \log \mathrm{sSFR}(\mathrm{yr}^{-1}) < -9.15$. Among galaxies with high specific SFR, $-8.8 < \log \mathrm{sSFR}(\mathrm{yr}^{-1}) < -8.2$, the fraction of galaxies with Fe II Doppler shifts (from -200 to $-100\,\mathrm{km\,s}^{-1}$) is boosted by up to a factor of 1.8 relative to the entire subsample with measured SFR.

In the LRIS sample, B-band luminosity is more significantly correlated with SFR (6.1σ from the null hypothesis, correlation coefficient $r_S = -0.87$) than is any other galaxy property.[14] Hence, within the full LRIS sample, we might expect to find the outflow fraction elevated among the more luminous galaxies. In Figure 10, the outflow fraction is indeed highest at all $V_{\rm crit}$ for the most luminous galaxies, but the significance of the distinction is hardly compelling ($\lesssim 1\sigma$).

The high specific SFR galaxies have bluer colors on average (4.1σ from the null hypothesis, $r_S = -0.58$). Since we find a higher outflow fraction among galaxies with high specific SFR, we might expect an enhanced outflow fraction among bluer galaxies in the full sample. From Figure 10, we simply note that any enhancement in outflow fraction with bluer color is weaker than the marginal one seen with B-band luminosity. These results are consistent with outflow fraction depending primarily on specific SFR, and color being strongly dependent on galaxy luminosity and mass as well as specific SFR. In light of the increasing outflow fraction with specific SFR, the absence of any variation in the outflow fraction over the redshift range from 0.4 to 1.4 deserves further inspection because galaxies have larger SFRs and specific SFRs at higher redshift.

The three redshift tertiles for the LRIS sample with *GALEX* photometry are shown in the SFR–stellar mass plane in Figure 11. We show the *SFR–M_* main sequence* (Noeske et al. 2007a, 2007b; Elbaz et al. 2007) fitted to the *GALEX*-detected subsample of 6102 DEEP2 galaxies with stellar mass measurements. The specific SFRs of the galaxies with Fe II blueshifts are 1σ larger than the average sSFR at the same stellar mass. Furthermore, the main sequence fitted to the *GALEX*-detected subsample is entirely consistent with our fit to the SFRs and stellar masses estimated for the full sample of blue-cloud galaxies in DEEP2 (Mostek et al. 2012).[15] We can therefore conclude that the galaxies with Fe II blueshifts have slightly higher sSFR than the typical blue-cloud galaxy.

Among our subsample of galaxies with measured SFRs, only galaxies with sSFR $> 0.8\ \mathrm{Gyr}^{-1}$ show secure, 3σ blueshifts. Since the slope of the main sequence is less than unity, the typical sSFR falls gradually with increasing stellar mass and this may explain why the Fe II blueshifts will be detected up to larger stellar masses at higher redshift. An sSFR threshold for Fe II blueshifts around $0.8\ \mathrm{Gyr}^{-1}$ would explain the paucity of 3σ blueshifts in the low redshift tertile. Inspection of Figure 11, however, shows that not all galaxies with high sSFRs have blueshifted Fe II absorption in their spectra. Hence, it will be important to measure SFRs for the remainder of the LRIS sample and determine whether the minimum sSFR criterion remains a necessary condition for seeing blueshifted Fe II absorption in galaxy spectra.

Given the distinct shapes of the Fe II and Mg II absorption troughs in some spectra, we compare the demographics of

[14] A weaker correlation of somewhat lower significance is found between SFR and stellar mass (4.3σ from the null hypothesis, $r_S = 0.61$).

[15] Mostek et al. (2012) use the AEGIS data to calibrate the results of SED fitting to optical photometry. Comparison of this SFR–stellar mass relation to previous work is complicated by differences in both redshift range and methods used to derive stellar mass and SFR. For example, the Noeske et al. (2007a, 2007b) relation was measured at lower redshift $0.2 < z < 0.7$, which may explain why our fit is about ~ 0.2 dex higher with similar slope. For our subsamples at $0.842 < z < 1.349$, the SFR–stellar mass relation in DEEP2 is remarkably shallower in slope than the Elbaz et al. (2007) relation fitted at $0.7 \leqslant z \leqslant 1.2$.

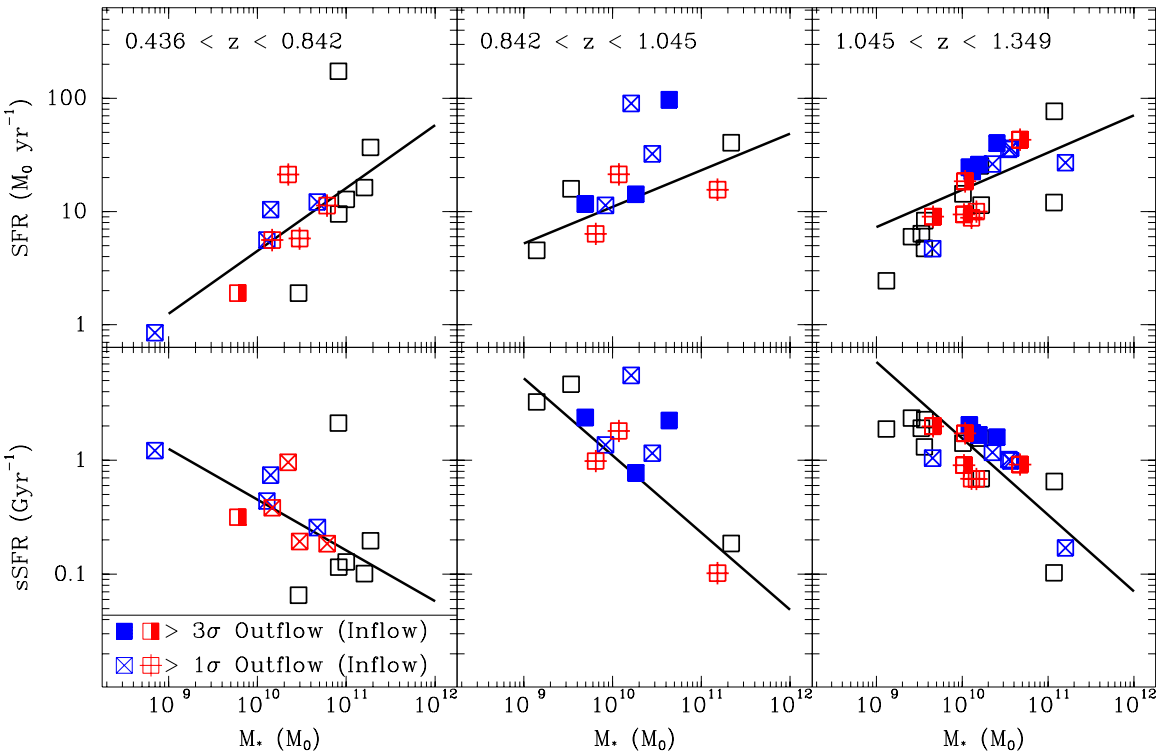

Figure 11. Location of galaxies with Fe II blueshifts in the SFR–M_* and specific SFR–stellar mass diagram. The UV-corrected SFRs have been divided by 1.8 to put both the SFR and stellar mass on a Chabrier IMF. Within each redshift tertile, the bold line marks the main sequence of star-forming galaxies fitted to the full sample of DEEP2 galaxies with *GALEX* photometry; we excluded galaxies with $U-B$ redder than the green valley, $U-B > 1.135$–$0.032(M_B+21.18)$, from the fit. The slope of the best fit flattens a bit from the lowest redshift data ($\log\langle\mathrm{SFR}\rangle = 0.5419\log\langle M_*\rangle - 4.7255$) through the middle redshift tertile ($\log\langle\mathrm{SFR}\rangle = 0.4020\log\langle M_*\rangle - 2.9337$) to the highest redshift spectra ($\log\langle\mathrm{SFR}\rangle = 0.2975\log\langle M_*\rangle - 1.7488$). The galaxies with the most robust Fe II blueshifts (solid blue squares) all lie on or above the main sequence.

(A color version of this figure is available in the online journal.)

galaxies with blueshifted Fe II absorption and those with highly blueshifted Mg II absorption. Figure 12 shows the fraction of galaxies with Mg II absorption at blueshifts larger than a threshold velocity, V_{crit}. Once again (as for Fe II blueshifts), galaxies with high specific SFR appear more likely to show highly blueshifted Mg II absorption in their spectra; the fraction of spectra with highly blueshifted Mg II absorption (as measured by V_{max}(Mg II)) shows no trend with redshift. In contrast to the case for Fe II blueshifts, however, the outflow fraction derived from the Mg II blue wing shows not even a weak dependence on SFR alone.

While the outflow fraction curves in Figure 12 are highest for galaxies with higher masses, higher luminosity, and redder color, the enhancement with each of these properties is not statistically significant. The larger error bars in Figure 12 relative to Figure 10 arise from not all spectra showing resolved Mg II absorption troughs (and therefore no V_{max} estimate). Within the measurement uncertainties, however, we conclude that the fraction of galaxies with outflows as determined by V_{max}(Mg II) appears to be less dependent on SFR than the outflow fraction determined by V_1(Fe II). Furthermore, both of these outflow indicators are remarkably insensitive to other fundamental galaxy parameters including stellar mass, B-band luminosity, color, and redshift.

5.2. Physical Properties of Outflows

The properties of winds have generally been varied in cosmological simulations in order to fit observations of fundamental galaxy properties such as stellar content, SFR, and metallicity evolution (Davé et al. 2011a, 2011b). Direct measurements of outflow velocity and mass flux are therefore of great importance for modeling galaxy formation and evolution. Here we discuss the measured Doppler shifts and the Fe II column densities. We will illustrate plausible extrapolations to the wind velocity and mass flux but emphasize that, in order to accurately model the interplay of the various gas phases, well-resolved simulations of galactic outflows need to be projected into the quantities we observe.

The escape of metals from low-mass galaxies in the local universe has been established empirically (Martin 1999; Martin et al. 2002; Tremonti et al. 2007). This enrichment of the circumgalactic medium by winds probably started very early in cosmic history based on the properties of metal-line systems at high redshift (Meyer & York 1987; Lu 1991; Songaila & Cowie 1996; Ellison et al. 2000; Schaye et al. 2003; Simcoe et al. 2006; Martin et al. 2010; Simcoe 2011). The main question is whether these outflows transport substantial mass. The winds clearly affect the chemical evolution of galaxies, but their role (if any) in creating the observed baryon deficit remains unclear (e.g., McGaugh et al. 2010).

Since we use low-ionization metal lines to identify the blueshifted absorption, our survey does not probe the hot phase of a galactic wind. The low-ionization gas is entrained in the hot wind by the breakup of supershells (Fujita et al. 2009), the shear between the free wind and the galactic ISM (Heckman et al. 2000), and pre-existing, interstellar clouds (Cooper et al. 2008,

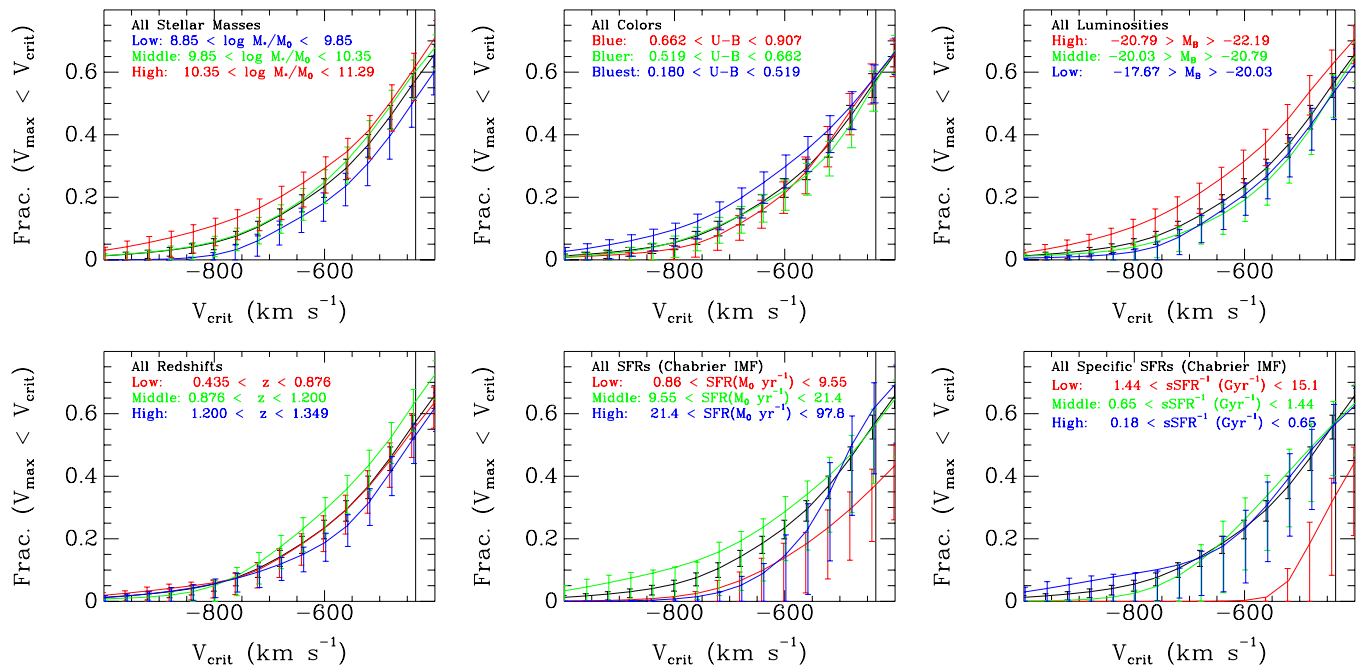

Figure 12. Fraction of galaxies with Mg II absorption detected at velocities larger (bluer) than a velocity $V_{\rm crit}$. The black curve shows the entire sample with Mg II measurements; and the colored curves break this sample into thirds by galaxy properties. The $V_{\rm max}$ measurements have not been corrected for instrumental smoothing of the spectra, so the curves are only physically meaningful at blueshifts significantly larger than the width of the instrumental profile which is $-435\,{\rm km\,s^{-1}}$ (vertical line in each panel) in the 400 lines mm^{-1} spectra. A high-velocity blue wing is most prevalent among spectra of higher mass, higher luminosity, and redder galaxies and does not appear in spectra of galaxies with the lowest sSFR.

2009). The relationship between this warm gas and hot wind fluid is critical to any extrapolation of our measurements to the wind properties. In the recent Hopkins et al. (2012) simulation of a high-redshift galaxy (which has properties typical of our sample), however, the warm, low-ionization gas carries the bulk of the outflowing gas mass; hence we may be observing the dominant phase of the wind (by mass). The mass-loss rates derived from low-ionization gas should still be viewed as lower limits on the mass flux in the multiphase wind; for example, inspection of the other types of galaxies in Figure 4 of Hopkins et al. (2012) shows that the hot wind fluid can carry most of the mass at some outflow velocities.

5.2.1. Outflow Solid Angle

The measurements presented in Section 5.1.2 provide a statistical characterization of which galaxies have spectra with blueshifted low-ionization absorption. Among the various velocity measurements discussed, we have argued that the net Doppler shift of the Fe II lines provides the most robust indication of a net outflow of gas along the sightline. The fraction of spectra with blueshifted Fe II absorption decreases toward larger Doppler shifts. Possible origins for this trend include variations in outflow velocity with galaxy properties, a velocity-dependent covering fraction, or an angular dependence in outflow velocity generated by the forces collimating the outflow.

We can distinguish among these scenarios using the demographics of the sample. For example, some galaxies with high SFR have spectra which do not show a net blueshift of the resonance absorption; and we will show in Section 5.3 that the blueshifts do not vary strongly with any galaxy property. Hence, we find no indication that the small fraction of galaxies with the largest blueshifts have unique physical properties and conclude that the outflow velocity does not vary strongly within our sample of blue galaxies. Furthermore, while gas covering fraction is likely velocity dependent as measured from resolved line profiles of lower redshift galaxies (Martin et al. 2009), gas covering fraction does not simply explain why galaxies with essentially the same physical properties differ as to whether their spectra show blueshifted absorption. Over the full range in Doppler shift, the outflow fraction varies very little in any measured galaxy parameter; the largest variations in outflow fraction are only a factor of two even though the stellar masses of the observed galaxies span more than 2 dex. We interpret this remarkable result as direct evidence for strong collimation of the outflows at $0.4 < z < 1.4$; and we predict that the spectra without Fe II blueshifts select galaxies viewed along a sightline perpendicular to the outflow direction.

Support for this interpretation comes from the inclinations of the AEGIS galaxies. In Figure 20 of Kornei et al. (2012), we show that the five spectra with 3σ blueshifts of the Fe II lines are found for galaxies viewed face-on, i.e., $i < 45^\circ$. In this scenario, the outflow fraction may be interpreted in terms of the solid angle of the outflow. For example, we consider a spherical outflow geometry. Let θ_B be the half-angle of a biconical outflow, then the outflow subtends a solid angle

$$\Omega = 4\pi(1 - \cos\theta_B), \tag{10}$$

and will be detected in a fraction $\Omega/4\pi$ of the galaxies we observe.

We also find a decrease in the outflow fraction as the Doppler shift becomes bluer, a result deserving further interpretation. We will simply note that if the covering factor of low-ionization gas decreases toward higher velocity, then the absorption troughs develop shallow blue wings as demonstrated by Martin et al. (2009) who had much higher resolution spectra of the Mg II doublet. The line profiles in the LRIS spectra lack the resolution required to directly measure the velocity dependence of partial covering. We observe a distinctly different property: a smaller

fraction of the spectra show the centroid of the absorption troughs at higher outflow velocities. Since the troughs are just as deep as the absorption lines detected at lower blueshifts (in spectra of other galaxies with similar properties), the velocity dependence of the outflow fraction in Figure 9 is not simply explained in terms of the gas covering fraction. Instead, we interpret the observation as evidence that outflows have a smaller opening angle at higher velocity. Smaller opening angle at higher velocity is qualitatively consistent with dynamical simulations of outflows where the opening angle is determined by the scale height of the ISM (De Young & Heckman 1994).

Our study provides this first evidence for highly collimated outflows at $z \sim 1$. In Figure 9, we show that the fraction of spectra with blueshifts increases as $V_{\rm crit}$ decreases. Specifically, we measure an outflow fraction of 0.025, 0.20, 0.45, and 0.65 at $V_{\rm crit} = 200, 100, 50,$ and $0\,{\rm km\,s^{-1}}$, respectively. The half-angle of the outflow cone would be 13°, 37°, 57°, and 70° at velocities of 200, 100, 50, and $0\,{\rm km\,s^{-1}}$. Hence our results indicate that the outflows subtend a larger (smaller) solid angle at slower (faster) speeds. Also, at all speeds, the outflow solid angle is much less than 4π steradians. While bipolar outflows are well documented at lower redshift (e.g., Heckman et al. 1990; Chen et al. 2010; Bouché et al. 2012), only recently has evidence for outflow collimation emerged at redshifts from $0.09 < z < 0.9$ (Bordoloi et al. 2011; Kacprzak et al. 2011).

The polar angle of $\theta_B \approx 37°$ for the outflow at $100\,{\rm km\,s^{-1}}$ derived from our results appears to be consistent with the distribution of outflowing gas in galactic halos. Bordoloi et al. (2011) mapped the Mg II absorption at impact parameters (to background galaxies) within 40 kpc of star-forming galaxies at $0.5 < z < 0.9$. Around blue, star-forming galaxies, the Mg II absorption equivalent widths are significantly higher at small polar angles, near the minor axis, than those measured closer to the major axis. Their results suggest the outflow cone makes an angle of 45° or less with the minor axis of the galaxy.

5.2.2. Mass Outflow Rates

We have nearly enough information to measure the mass flux in the low-ionization outflow. As described in Section 3.3.3, our measurements bound the Fe II column density on both sides; this is a significant improvement over previous studies that detected outflows only in saturated lines, which yield only lower bounds. We have also shown that the largest Doppler shifts in Fe II are roughly $200\,{\rm km\,s^{-1}}$ and provided some evidence that slower outflows may be simply viewed at higher inclinations (Kornei et al. 2012); this result constrains the outflow solid angle, Ω. The ionization correction for Fe II is uncertain but seems likely to lie in the range $\chi({\rm Fe^+}) \equiv n({\rm Fe^+})/n({\rm Fe}) = 0.1$–1 based on photoionization modeling (Churchill et al. 2003; Murray et al. 2007). In the halo gas of the Milky Way, the measured depletion of iron onto grains is much lower than its value in the cold disk; hence we conservatively take $\log d({\rm Fe}) \equiv [{\rm Fe/H}] = -0.69$ from Table 6 of Savage & Sembach (1996) as our best estimate of the depletion. For a spherical flow launched at radius R_0, the mass flux is

$$\dot{M} = \Omega v R_0 N({\rm H}) \bar{m}, \tag{11}$$

where the average mass per hydrogen atom is $\bar{m} = 1.4$ amu, Ω represents the solid angle subtended by an outflow with spherical geometry, v is the radial velocity of the outflow, and $N({\rm H})$ is the total hydrogen column density. The mass flux is independent of the covering factor because covering factors less than unity increase the inferred column density and decrease the solid angle Ω by the same factor.

The galaxy spectra do not uniquely constrain the location of the gas along the sightline. In a radially diverging flow, the column density integral "down the barrel" will be dominated by the densest gas near the launch radius; hence, the linear dependence of the mass flux on the launch radius in Equation (11). Simple models relate R_0 to the size of the starburst region (Chevalier & Clegg 1985) and/or several pressure scale heights in a gaseous disk (De Young & Heckman 1994). We therefore assume that $R_0 \lesssim 1$ kpc in order to illustrate the mass fluxes. Some of the absorbing gas is clearly at much larger radii based on the detection of spatially extended Mg II emission (Rubin et al. 2011; Erb et al. 2012; C. L. Martin et al., in preparation) and intervening Mg II absorption at impact parameters $b \leqslant 70$ kpc (Bordoloi et al. 2011).

Using the bounds on the Fe II column from Table 3, we note that the total "ISM plus outflow" column is less than $\log N({\rm Fe^+})C_f \lesssim 15.8$ in half the outflow galaxies, and the highest upper limit is 16.27. Expressing Equation (11) in terms of values consistent with the observations yields

$$\dot{M} = 23\,M_\odot\,{\rm yr^{-1}} \left(\frac{\Omega}{\pi}\right)\left(\frac{v}{200\,{\rm km\,s^{-1}}}\right)\left(\frac{R_0}{1\,{\rm kpc}}\right) \times \left(\frac{N({\rm Fe^+})}{10^{16}\,{\rm cm^{-2}}}\right)\left(\frac{3.16\times10^{-5}}{n({\rm Fe})/n({\rm H})}\right)\left(\frac{0.5}{\chi({\rm Fe^+})}\right)\left(\frac{0.20}{d({\rm Fe})}\right), \tag{12}$$

independent of the covering factor. For comparison, the median SFR in the AEGIS subsample is 12.3 $M_\odot\,{\rm yr^{-1}}$ for a Chabrier initial mass function (IMF; or, 21.9 $M_\odot\,{\rm yr^{-1}}$ for a Salpeter IMF), indicating a mass loading factor $\eta \equiv \dot{M}/{\rm SFR} \approx 1.9(1.1)$. A lower ionization fraction would clearly increase our mass flux estimate. Taking $\chi({\rm Fe^+}) \approx 0.1$, for example, raises the implied mass loading factor by a factor of five. We will estimate lower mass fluxes, however, when a correction is made for the contribution of interstellar gas to the absorption equivalent width.

In Section 3.3.2, we introduced a model that describes absorption at the systemic velocity with a maximum ISM component. We fit the typical properties of this ISM component and those of the Doppler component to the Fe II absorption. From Table 3, the column density in the Doppler component is typically in the range $14.47 < \log N({\rm Fe^+})C_f < 15.30$, where the limits are the median values $\log N_{\rm DOP}({\rm Fe^+})C_f$. In the mass flux estimate, the lower column density of the Doppler component is partially offset by its larger blueshift (relative to the single-component fit). De-projecting the line-of-sight velocity based on the collimation discussed in Section 5.2.1, a typical outflow velocity for the Doppler component is $V_{\rm Dop} = -476\,{\rm km\,s^{-1}}$. From Equation (12), we estimate a mass flux in the Doppler component of $\dot{M} = 2$–11 $M_\odot\,{\rm yr^{-1}}$. For a Chabrier IMF, we obtain $\eta \approx 0.2$–0.9, where η would be 1.8 times lower for a Salpeter IMF.

Since previous mass-loss rates were derived from lower limits on gas column density (from saturated lines), these new results show, for the first time, that the mass fluxes in the low-ionization gas are not orders of magnitude higher than the typical SFR in these $z \sim 1$ galaxies. Future work should be able to combine our constraint from "down-the-barrel" observations, absorption detections toward background quasars and galaxies, and the extent of scattered resonance emission to improve the accuracy of the mass flux in the metal ions.

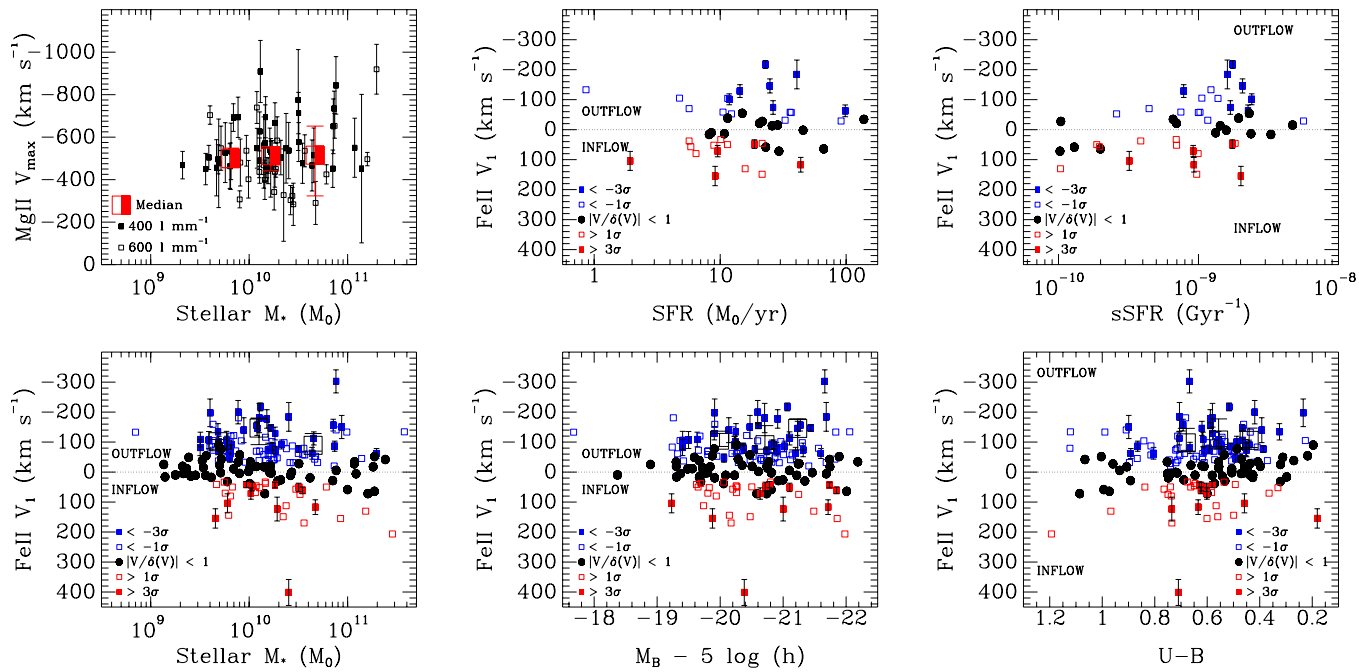

Figure 13. Range of Doppler shifts measured vs. galaxy properties. The outflow velocities projected along our sightline show no correlation with stellar mass, SFR, specific SFR, B-band luminosity, or $U-B$ color. Top left: maximum blueshift of Mg II λ2796 absorption trough vs. stellar mass. Large symbols mark the median values and the $\pm$34% range. Bottom left: Doppler shift of Fe II absorption troughs vs. stellar mass. Large symbols denote the median values of the spectra with significant ($>3\sigma$) blueshifts. Top center: Doppler shift of Fe II absorption troughs vs. star formation rate. Bottom center: Doppler shift of Fe II absorption troughs vs. B-band luminosity. Large symbols denote the median values of the spectra with significant ($>3\sigma$) blueshifts. Top right: Doppler shift of Fe II absorption troughs vs. specific SFR. Bottom right: Doppler shift of Fe II absorption troughs vs. $U-B$ color. Large symbols denote the median values of the spectra with significant ($>3\sigma$) blueshifts.

5.3. Outflow Scaling Relations

Empirical scaling relations for outflows help us to understand which physical processes shape outflows. For example, for local starbursts, the nearly linear increase in the blueshift of Na I absorption with increasing rotation velocity (Martin 2005) motivated outflow models in which radiation pressure accelerates the low-ionization gas (Murray et al. 2005). Momentum-driven outflows, in general, also predict an inverse scaling between the mass loading parameter and galaxy velocity dispersion, $\eta \equiv \dot{M}/\mathrm{SFR} \propto \sigma^{-1}$ (Murray et al. 2005; Oppenheimer et al. 2010).

The evidence presented in this paper for collimated outflows complicates testing the momentum-drive wind conjecture. The measured Doppler shifts cannot be de-projected into the outflow velocities without knowledge of the galaxy inclination. At this time, the best we can do is to look for trends of the median Doppler shift with galaxy properties. We emphasize, however, that high-resolution images of the sample would allow us to improve our interpretation of the spectral measurements.

In contrast to studies of resolved galaxies at much lower redshifts, we have good statistical constraints on the halo masses of the galaxies in the LRIS sample. The halo masses are of interest because galaxy evolution models invoke feedback to suppress star formation in halos less massive than a *mass floor* at $\log M_h/M_\odot \lesssim 11$ (e.g., Bouché et al. 2010) and predict that halo gas is mostly virialized (and therefore cold accretion and star formation suppressed) when $\log M_h/M_\odot \gtrsim 12$, the *mass ceiling*. The observed clustering (of star-forming DEEP2 at $z \sim 1$) galaxies with $M_B - 5\log(h) < -20$, brighter than the faintest tertile of the LRIS sample, indicate a bias of 1.28 (Coil et al. 2008). If 15%–20% of those galaxies are satellites, the minimum halo mass is $\log M_h/M_\odot \gtrsim 11.3$ (Zheng et al. 2007), and the mean halo mass is $\log M_h/M_\odot \approx 12.0$. Roughly one-third of the galaxies populate halos where gas accretion should occur primarily by hot-mode accretion. Our survey is sensitive to changes in outflow properties below the mass floor and above the mass ceiling.

5.3.1. Outflow Velocity versus Stellar Mass

In their study of composite spectra, Weiner et al. (2009) found that the Doppler shift of the most blueshifted Mg II absorption increased with stellar mass to the power 0.17. They measured the Doppler shift $V_{10\%}$ at 90% of the continuum intensity, which corresponds closely to our $V_{\max}$ measurement for the median continuum S/N of the LRIS spectra. The $V_{\max}$(Mg II) values measured for the LRIS sample, however, do not increase with M_*, as illustrated in Figure 13. We found that $V_{\max}$(Mg II) does increase with M_* when our analysis includes the K+A and green-valley galaxies, which have high stellar masses and older stars (contributing broad, stellar Mg II absorption). One reason our results may differ is that our 400 lines mm^{-1} spectra do not resolve the absorption troughs at blueshifts less than 435 km s^{-1}, so we will overestimate the median velocity when a large fraction of spectra have blue wings just below that resolution limit. To test this idea, we identify the 600 lines mm^{-1} spectra by open squares and see that these $V_{\max}$ values become less blueshifted with increasing M_* in Figure 13. Furthermore, our measurements for the Fe II centroid velocity V_1, which are not affected much by the resolution, do not vary strongly with stellar mass either in Figure 13. The centroid velocities systematically underestimate the outflow velocity in more massive galaxies because the interstellar absorption at V_{sys} is stronger; but when we estimated the velocity corrections with two-component fitting, the median blueshifts of the Doppler component did not reveal a significant trend with stellar mass. Spectral resolution is therefore not an obvious explanation for the discrepant result,

yet it remains unclear whether stellar absorption significantly biases the Weiner et al. (2009) composite spectrum for high stellar mass.

5.3.2. Do Outflows Escape?

We follow Weiner et al. (2009) and use [O II] velocity dispersions, $\sigma_{[\mathrm{O\,II}]}$ (Weiner et al. 2006), to estimate the depths of the gravitational potentials for galaxies in the LRIS sample.[16] The relationship between the local escape velocity and $\sigma_{[\mathrm{O\,II}]}$ is sensitive to the location of the absorbing gas along the sightline to each galaxy. For a spherical outflow geometry (of any solid angle), much of the column density of an outflow viewed down the barrel is necessarily contributed by the gas near the launch radius due to the inverse-square dilution of the gas density. The most conservative assumption is therefore that the gas lies a few pressure scale heights above the disk at radius $R = 1$ kpc. For an isothermal halo of radius 100 kpc, the escape velocity at $R = 1$ kpc is $V_{\mathrm{esc}} = 6.1\sigma_{[\mathrm{O\,II}]}$. The median values of V_{esc} computed this way are 281, 406, and 643 km s^{-1} for the low, middle, and high stellar mass tertiles; but the escape speeds are lower if the gas is further away. We detect absorption at V_{max} values higher than these V_{esc} estimates, see the upper left panel of Figure 13, and therefore support the conclusion of Weiner et al. (2009) that outflowing gas detected in Mg II may not return to the galaxy.

The absence of observed growth in V_{max} with stellar mass implies that a higher fraction of outflowing gas is recycled in more massive galaxies. In light of the significant uncertainties inherent in interpreting V_{max}—including projection, sensitivity to S/N, dependence on spectra resolution, and possible stellar contamination—the results presented here are probably not the final word on this scaling. In particular, we would not discount models that predict $V_{\mathrm{max}} \propto V_{\mathrm{esc}}$ (Murray et al. 2005; Zhang & Thompson 2012); their results are supported by observations of small samples of local starbursts observed at much higher resolution and S/N (Martin 2005; Rupke et al. 2005).

The Fe II Doppler shifts and the V_{max}(Mg II) values suggest that outflows reach the circumgalactic medium. For example, we have measured Mg II absorption at blueshifts as high as 700 km s^{-1}; and, these outflows would coast to 70 kpc in 100 Myr, a short enough time period for the host galaxy to remain blue even if the SFR declines due to the outflow. Bouché et al. (2006) found an anti-correlation between intervening absorber equivalent width and host halo mass. In contrast, we find the largest Mg II equivalent widths in the more massive galaxies. Hence, the strengths of intervening Mg II absorption and the total Mg II equivalent width in galaxy spectra scale differently with galaxy mass. This apparent contradiction may be resolved by appealing to two of our results: (1) from two-component fitting (see Section 3.3.2), the equivalent width of ISM absorption (at the systemic velocity) grows with increasing stellar mass and (2) emission filling is stronger in lower mass galaxies (see Section 4.2). Since the resonance emission in halo sightlines is negligible, and many halo sightlines intersect little ISM, the physical effects driving the equivalent width–stellar mass trend in galaxy spectra largely do not apply to intervening absorption.

[16] To the extent that the line-of-sight velocity dispersion measured from the line width reflects the gravitational potential, the 3D velocity dispersion will be approximately $\sqrt{3}$ times larger. Averaging over the variation in the relation between the line-of-sight velocity dispersion, $\sigma_{[\mathrm{O\,II}]}$, and the rotation velocity at different disk inclinations (Rix et al. 1997; Kobulnicky & Gebhardt 2000; Weiner et al. 2006), Weiner et al. (2009) argue that $V_c \sim 1.67$–$2\sigma_{[\mathrm{O\,II}]}$ with scatter of $\sim 25\%$.

Since our results indicate that outflows from $z \sim 1$ galaxies subtend a solid angle much less than 4π, we expect the intervening absorption from outflows to show a dependence on azimuthal angle, specifically the location of the sightline relative to the gas disk and outflow axis. Simple dynamical arguments show that the "blowout" will be perpendicular to the gaseous disk (De Young & Heckman 1994), so a distinguishing property of outflows is that they would be detected in sightlines passing near the minor axis of a galaxy. New evidence for a bimodal distribution of azimuthal angles among strong Mg II systems (Bouché et al. 2012; Kacprzak et al. 2011) supports our conclusions that outflows (minor axis absorption) make a substantial contribution to the population of intervening absorbers. The average minor axis sightline within 60 kpc of a blue galaxy (at $0.5 < z < 0.9$) shows more absorption than a typical sightline at the equivalent impact parameter along the major axis (Bordoloi et al. 2011). This excess absorption provides the best constraint to date on the distance to which the Mg II clouds survive in the galactic outflows.

5.3.3. Scaling with SFR, sSFR, and M_B

In Figure 13, the Fe II centroid velocities are shown against SFR, sSFR, absolute B-band magnitude, and color. The median velocities of both the 3σ outflows and the 1σ outflows show no systematic trend with any of these galaxy properties. We examined similar plots using the velocities of the Doppler component and found no correlations with the Doppler component. In the SFR and sSFR plots, the error bars on the median are quite large owing to the small number of galaxies in each bin. This large uncertainty combined with the relatively small range in SFR ($\sim$1 dex) could hide any underlying correlation between V_1 and SFR.

To increase the SFR baseline, we compare V_{max} measurements to nearby dwarf galaxies and extremely luminous starbursts in Figure 14. First, we note that our median V_{max}(Mg II) measurements are consistent with the Weiner et al. (2009) measurements at slightly higher redshift. Second, when lower mass galaxies are included, the envelope describing the maximum outflow velocity increases with SFR. Excluding the galaxies with dominant central objects (DCOs), because their high velocities may be related to AGN (Heckman et al. 2011), the slope is consistent with the $V \propto \mathrm{SFR}^{0.35}$ relation measured previously for local starbursts (Martin 2005).

The true scatter in the $V_{\mathrm{max}} - \mathrm{SFR}$ scaling may be even larger than it appears in Figure 14. Small Doppler shifts would go undetected unless the spectral resolution is very high, and echelle resolution has only been obtained for the nearby dwarf galaxies. Hence, the absence of data in the lower right corner of this plot is in part a selection effect. Moreover, projection effects only make the measured Doppler shifts lower than the outflow velocity, so the upper limit rather than the median is most interesting. The low-redshift galaxies shown in these plots are all starburst galaxies, and their SFR surface densities are typically higher than the outflow threshold (Heckman 2002, 2003; Kornei et al. 2012). From this viewpoint, we argue that the absence of large Doppler shifts in dwarf galaxies—i.e., the paucity of points in the upper left of Figure 14—is the most important feature of this scaling relation. Considering the multiphase nature of winds, however, the apparent lack of high-velocity outflow in dwarf galaxies may be limited to warm, low-ionization gas. Based on Figure 4 of Hopkins et al. (2012), we suspect that most of the mass in a dwarf starburst outflow may be in the hot phase where the flow is moving at more

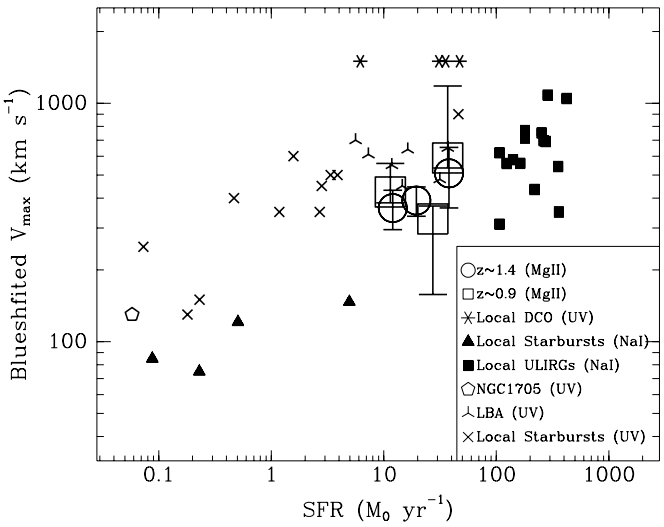

Figure 14. Maximum blueshift of low-ionization absorption vs. SFR. Large symbols show the median values among the LRIS galaxies and the Weiner et al. (2009) measurement of composite spectra. The legend denotes the sample and the lines used to measure the maximum blueshift of the absorption trough. Measurements for local galaxies from Heckman et al. (2011; asterisk), Schwartz & Martin (2004; filled triangle), Martin (2005; filled square), Grimes et al. (2009; crosses), Heckman et al. (2011; trefoil), and Vázquez et al. (2004; NGC 1705 with SFR from Marlowe et al. 1997). Over the relatively small range in SFR covered by our LRIS sample, the median V_{max}(Mg II) values measured among individual galaxies at $z \sim 1$ are comparable to the maximum blueshifts of resonance lines in local samples of galaxies with the notable exception of the larger blueshifts among the galaxies with a dominant central object (DCO). Starbursts in dwarf galaxies only show low-ionization absorption at significantly smaller Doppler shifts.

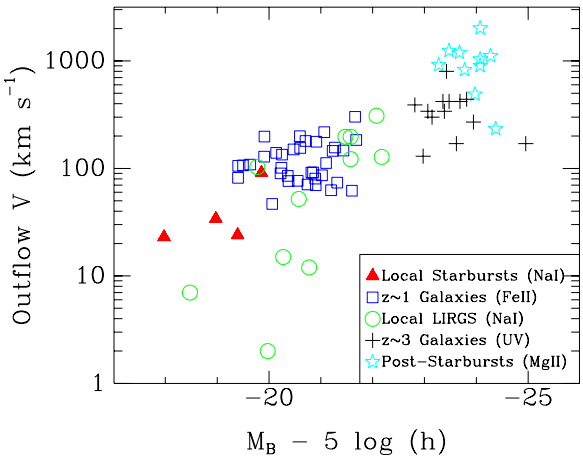

Figure 15. Outflow velocity of individual galaxies vs. absolute *B*-band magnitude. The legend identifies the samples and the transition(s) used to measure Doppler shift. The 3σ outflows in the LRIS sample have velocities intermediate to local starburst galaxies (Schwartz & Martin 2004) and local luminous infrared galaxies (Heckman et al. 2000). Local post-starburst galaxies (Tremonti et al. 2007) and high-redshift galaxies (Pettini et al. 2001) show larger outflow velocities but also have significantly larger luminosities.

(A color version of this figure is available in the online journal.)

than a few hundred km s^{-1}. If the highest velocity gas is in fact unobservable in low-ionization lines, then outflow velocity may not increase appreciably with SFR as argued, for example, based on the measured temperatures of the X-ray emitting gas (Martin 1999).

Figure 15 compares our V_1(Fe II) measurements for the outflow sample to other populations with starburst-driven outflows. Each of these samples includes spectra in which the resonance absorption lines show no significant blueshift relative to the galaxy, but we plot only the outflow galaxies. Since the different surveys have different criterion for the minimum detectable Doppler shift, the absence of points in the lower right corner is not significant; but the maximum outflow speeds of each population likely represent the "down-the-barrel" view of their outflows. Taken together, these measurements show outflow speed increases with *B*-band luminosity. Since *B*-band luminosity is correlated with SFR, this result provides evidence for higher outflow velocities in galaxies with higher SFRs.

6. GAS INFLOWS

In Section 1 we discussed gas inflows in the context of a popular model whereby the gas accretion rate regulates the galactic SFR (Dekel & Birnboim 2006; Kereš et al. 2009a, 2009b; Bouché et al. 2010; Davé et al. 2012). Testing this theory requires observations of the gas inflows that reach galactic disks. Cosmological simulations agree that the infalling gas which fuels star formation is *cold*, in the sense that its temperature never exceeded $10^{5.5}$ K, and that these cold flows gradually disappear at halo masses exceeding 10^{12} $M_\odot$ due to the formation of virial shocks which increase the gas cooling time (Kereš et al. 2005, 2009a; Dekel & Birnboim 2006; Ocvirk et al. 2008; Brooks et al. 2009; van de Voort et al. 2011b). The densest gas in these cold flows has a low covering factor but threads filaments of lower density gas with cross sections much larger than a galaxy (Kimm et al. 2011; Faucher-Giguère & Kereš 2011; Fumagalli et al. 2011). These inflowing streams carry significant angular momentum that cause them to corotate with the galaxy and form a warped, extended disk; hence cold flows may be recognized kinematically by a velocity offset in the same direction as the rotation of the central disk (Stewart et al. 2011a, 2011b).

In contrast to the accretion rate onto *halos*, which is robustly predicted, the rate of gas accretion onto *galaxies* depends sensitively on feedback processes (van de Voort et al. 2011a). Winds transport supernova ejecta into the circumgalactic medium (Martin et al. 2002), so these metals mark gas that was once in a galaxy. The mixing between these metals and cold flows is challenging to resolve in numerical simulations, so the metallicity of accreting gas near galaxies remains quite uncertain. At least in some models, however, recycling of the metals carried to large distances by winds substantially increases the metallicity of the infalling gas (Oppenheimer et al. 2008; Davé et al. 2011a). In other simulations, in contrast, the cold flows are not even detectable in metal lines owing to their low metallicity (Kimm et al. 2011; Fumagalli et al. 2011; Goerdt et al. 2012).

The obvious difference between galactic outflows and inflows is the kinematics of the absorption lines they imprint on galaxy spectra. Blueshifted (redshifted) lines in galaxy spectra necessarily mark outflowing (inflowing) gas because the absorbing material must lie on the near side of the galaxy. Near-UV spectra are equally sensitive to redshifted and blueshifted Fe II absorption. Because blueshifts turn out to be more common, composite spectra miss the redshifted absorption, and spectra of individual galaxies turn out to be critical for identifying inflows (Sato et al. 2009; Rubin et al. 2012). Inflow detections apparently require surveys of roughly a hundred or more galaxies. Both the measurements presented here (9 spectra out of 208) and recent work by Rubin et al. (2012) identify inflowing metals toward a few percent of $z \sim 1$ galaxies.

These infalling streams may not arise from cold flows; the metals may mark gas recycled through galactic winds, tidally

stripped gas, and/or material condensing out of hot halo gas. To provide some basis for distinguishing among these processes, in Sections 6.2 and 6.3 we individually examine the spectra of 3σ inflow galaxies and estimate physical properties of the inflowing gas. In particular, we find evidence that the infalling gas detected in front of the galaxies marks an inflowing stream which subtends a larger solid angle than the galaxy on the sky. We then return to the discussion of the source of the inflow in Section 6.4 focusing primarily on the cold inflow model due to recent interest in, and theoretical predictions for, this particular scenario.

6.1. Inflow Confirmation

We identify a net inflow of low-ionization gas by a statistically significant redshift of the Fe II absorption troughs, $V_1(\text{Fe II}) \geqslant 3\sigma(V_1)$. The uncertainty in this fitted centroid velocity does not take errors in the galaxy redshift determination into account. We reviewed the redshift determination and other sources of systematic error individually for the 11 galaxies with 3σ inflows and identified possible systematic errors in two of the three cases described here.

All but one (22028473) of the inflow galaxies have strong emission lines in our LRIS spectrum; and, as described in Section 2.2, we measure the centroids of the emission lines to within $\pm 19\,\text{km s}^{-1}$. Among these inflow galaxies, the average difference between this LRIS redshift and the DEIMOS redshift from DEEP2 is $45\,\text{km s}^{-1}$ with neither survey yielding systematically higher (or lower) redshifts. The magnitude of this discrepancy is consistent with the internal error of $41\,\text{km s}^{-1}$ reported by DEEP2 from multiple observations of galaxies and presumably arises from velocity gradients across galaxies. For the inflow galaxy 22028473, however, the galaxy redshift comes from the [O II] emission in the DEEP2 DEIMOS spectrum because our LRIS spectrum does not cover optical, nebular lines. The fitted Doppler shift of the Fe II absorption, $41 \pm 10\,\text{km s}^{-1}$ in Table 4, is comparable in magnitude to the systematic error in the redshift determination. Although correcting this error is equally likely to (a) double the inflow speed or (b) negate the inflow detection, we drop this object from the inflow sample because it is not a significant ($>3\sigma$) detection when the error in the galaxy redshift is considered.

Our adopted LRIS redshift for 22005270 exhibits one of the largest discrepancies from the DEEP2 redshift, $69\,\text{km s}^{-1}$. The velocity gradient between apertures 2 and 4 exceeds this discrepancy, so systematic differences in slit placement may well be the cause. The Hβ emission line in our spectrum of 22005270 appears very slightly redshifted, but we attribute this shift to residuals from a sky line $93\,\text{km s}^{-1}$ redward of Hβ. We keep this object in the inflow sample. The LRIS redshift accurately determines the systemic velocity for the purposes of comparing the velocities of the galaxy and the resonance absorption. Even if we adopted the extremely conservative viewpoint that the redshift uncertainty was $60\,\text{km s}^{-1}$, the projected infall velocity of $401 \pm 43\,\text{km s}^{-1}$ still yields a 3σ inflow detection.

We do remove 22036194 from the inflow sample because of the systematic error introduced in our Fe II series fit by intervening absorption. Our 22036194 spectrum was recorded at a position angle of 25°, so the slit passes near the $z = 0.913$ galaxy 22035919 at an angular separation of 7″.1. Intervening Mg II absorption from a foreground galaxy near this redshift appears slightly redward of the interstellar Fe II λ2344 absorption trough in our 22036194 spectrum. The net, blended absorption trough is stronger and redder than the other lines in the Fe II series and therefore systematically biased the fit. Rejection of the Fe II λ2344 transition yields a fitted Fe II absorption velocity consistent with the interstellar gas in 22036194. We note, however, that 22035919 is unlikely the source of the intervening absorption due to the strength of the line and the $\gtrsim$50 kpc impact parameter. We detect prominent emission lines (near $z \sim 0.831$), in fact, from another galaxy closer to the 22036194 sightline in our 2D spectrum and suggest this object is the source of the intervening Mg II absorption.

With 22028473 and 22036194 rejected, the 3σ inflow sample contains nine galaxies. Figures 16 and 17 illustrate the 3σ redshifts of the Fe II absorption troughs relative to the nebular emission. The joint fits to the Fe II series find a significant redshift because the absorption troughs of multiple transitions show a net redshift. The redshifted absorption does not appear to be unique to the Fe II lines; the Mg II 2803 absorption trough (row 7 of these figures) often has a net redshift as well. Table 4 provides the measured properties of the redshifted absorption troughs. Table 2 summarizes the quality of the individual spectra and galaxy redshift, *B*-band luminosity, color, stellar mass, and (when available) SFR.

6.2. Spatial Extent of Infalling Gas

We examined the two-dimensional spectra for velocity gradients along each slitlet. For illustration, Figure 18 shows the positions of the slitlets and selected regions of the two-dimensional spectra for the four galaxies with large velocity gradients. The [O II] emission lines are clearly tilted along the slits crossing 12011428, 12019996, and 42006875 as is the [O III] λ5007 emission along the 22005270 slit. We obtain additional insight about the inflows by investigating whether the emission or absorption anywhere along the slit is at the same velocity as the redshifted Fe II absorption discovered in the galaxy spectra (i.e., extracted from apertures centered on the galaxy). We now consider the two-dimensional spectra of each of these galaxies in further detail.

12011428. Along the slit that crosses 12011428, the line emission is not continuous. To the north of 12011428, a second blob of [O II] emission is detected 1″.14 (9.6 kpc) away along the slit. The image shows a hint of faint, extended *R*-band emission in this direction. An [O II] emission-line spectrum extracted at this location exhibits a redshift of $125 \pm 15\,\text{km s}^{-1}$. The emission redshift on this side of the galaxy is remarkable because resonance absorption is seen at a similar velocity, $154 \pm 32\,\text{km s}^{-1}$, in the galaxy spectrum (extracted from an aperture centered on the galaxy continuum). This coincidence in velocity space may indicate that the infalling stream crossing the center of the galaxy reaches the galaxy near the star-forming knot 9.6 kpc away. Further evidence supporting a structural connection between the redshifted emission and absorption is found in the grism (blue) spectrum extracted on the northern side of the galaxy (aperture marked in green in Figure 18). The Fe II resonance absorption remains redshifted in the off-center spectrum, and we find no spatial gradient in the absorption velocity across the 12011428 slit. The infalling gas apparently covers 12011428, and one side of the galactic disk shares the redshift of this infalling stream.

22005270. Along the slit that crosses 22005270, the line emission is not continuous in the two-dimensional spectrum shown in Figure 18. Roughly 3″.5 southwest of 22005270, where the slit passes near galaxy 22005066, we detect a spatially extended blob of [O III] emission (1″.6 or 12.2 kpc across). Further along

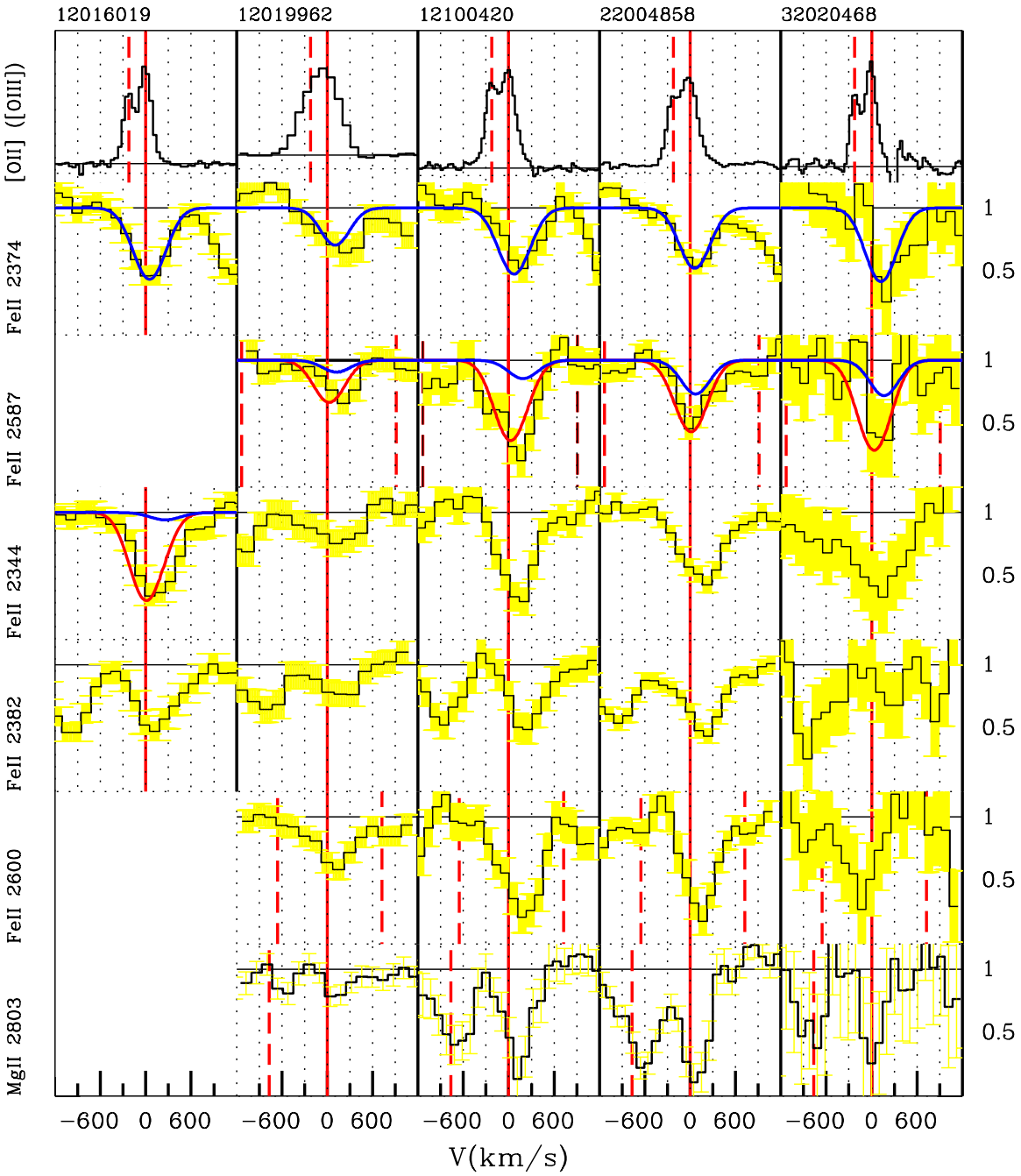

Figure 16. Spectra with resonance absorption lines (bottom six rows) significantly redshifted with respect to nebular emission lines (top row); see also Figure 17. The solid (red) vertical line marks the systemic velocity. Dashed vertical lines denote the wavelengths of nearby transitions; note the airglow line at $-735\,\mathrm{km\,s^{-1}}$ blueward of the Mg II λ2796 line in 12019996, which affects the wing of λ2796 blueward of $-359\,\mathrm{km\,s^{-1}}$. The single-component fit to the Fe II series is superposed on the Fe II λ2374 profile; and the two-component fit to the Fe II series is plotted on the Fe II 2587 profile (with Doppler component shown by the dashed blue line). These inflow galaxies were selected based on the significance of their Fe II redshift, but their spectra typically show redshifted Mg II as well. Two-component fits to the Fe II absorption troughs yield slightly higher inflow velocities than the one-component fits.

(A color version of this figure is available in the online journal.)

this slit, we extracted another spectrum 4″.3 (33 kpc) southwest of 22005270 because the [O III] emission-line profile is double peaked; the stronger, longer wavelength maximum at $346\,\mathrm{km\,s^{-1}}$ and a weaker component at $-158\,\mathrm{km\,s^{-1}}$. The large emission redshift near 22005066 is remarkable because Fe II resonance absorption is seen at a similar velocity in the spectrum of 22005270. In fact, the spectrum of 22005270 shows the largest Fe II redshift at $401 \pm 43\,\mathrm{km\,s^{-1}}$. Within the uncertainties, this absorption velocity is marginally consistent with the emission component at $346 \pm 19\,\mathrm{km\,s^{-1}}$. Further evidence for a connection between the redshifted [O III] emission near 22005066 and the redshifted absorption in the 22005270 spectrum is apparent upon re-inspection of the primary spectrum toward 22005270. In both Figures 17 and 18, the bright [O III] emission in the 22005270 spectrum falls at zero velocity by definition, but a weak redshifted emission component is detected at $341\,\mathrm{km\,s^{-1}}$, a redshift similar to the centroid velocity of the Fe II absorption. We show the extracted blue spectrum where the slit passes near

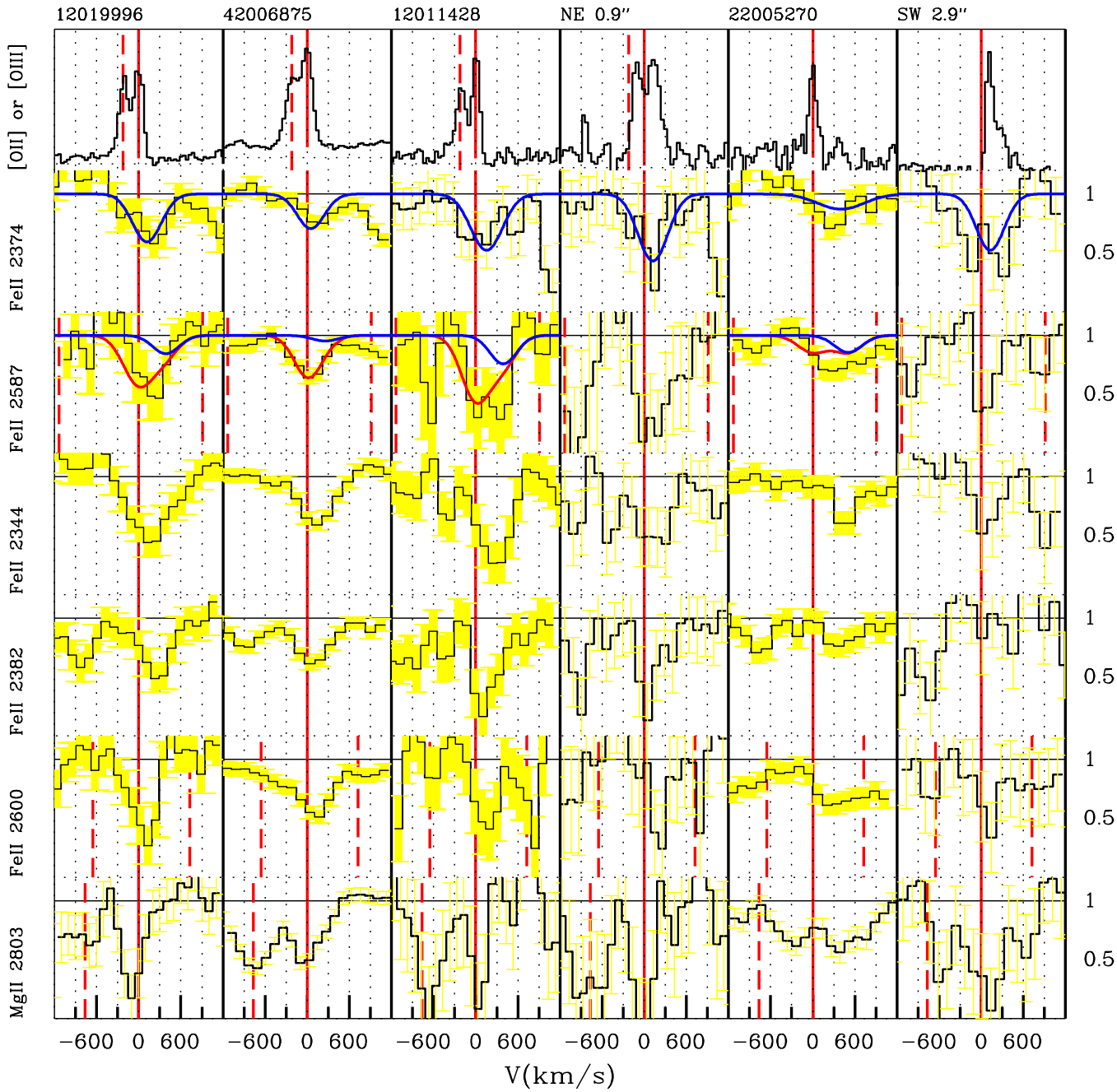

Figure 17. Spectra of the other galaxies with redshifted resonance absorption. Colored lines have the same meanings as defined in the caption to Figure 16. In addition to the *down-the-barrel* spectra, i.e., a spectrum extracted from the aperture centered on a galaxy), spectra extracted off-center are shown for the two galaxies with spatially extended continuum emission. At locations 0.″85 northeast of 12011428 and 2.″94 SW of 22005270, the Fe II Doppler shifts are 123 ± 47 and 129 ± 62 km s^{-1}, respectively, consistent with the redshifts measured down the barrel (toward the centers) of those two galaxies. In contrast, the nebular emission lines, which are by definition at zero velocity in the down-the-barrel spectra, are prominently redshifted in the spectra extracted off-center. Off the center of each galaxy, the redshift of the nebular emission and the Fe II absorption are very similar, consistent with a common physical location along the sightline.

(A color version of this figure is available in the online journal.)

22005066 in Figure 17. The continuum S/N in this spectrum is low relative to the blue spectrum of 22005270; but we see a net redshift of the Fe II and Mg II absorption. These coincidences in velocity space indicate that the infalling gas seen in absorption toward 22005270 is part of a physical structure covering both 22005270 and 22005066 and therefore at least 33 kpc across.

12019996. The tilt of the [O II] emission in the 12019996 spectrogram shows the usual signature of a rotating disk. The emission extends 0.″68 (5.6 kpc) to the south where the Doppler shift reaches 102 ± 10 km s^{-1}. The velocity gradient between the central aperture and the receding side is nearly as large as the 117 ± 25 km s^{-1} redshift of the Fe II absorption in the central aperture. The infalling gas marked by the redshifted resonance absorption may therefore extend all the way across the 12019996 disk.

42006875. In the 42006875 spectrum, the tilt of the [O II] emission shows the usual signature of a rotating disk. Across the 42006875 slit, the relative redshift of the emission reaches 68 km s^{-1} 1.″4 (10 kpc) to the northwest of the center of the galaxy. The velocity gradient between the center of the

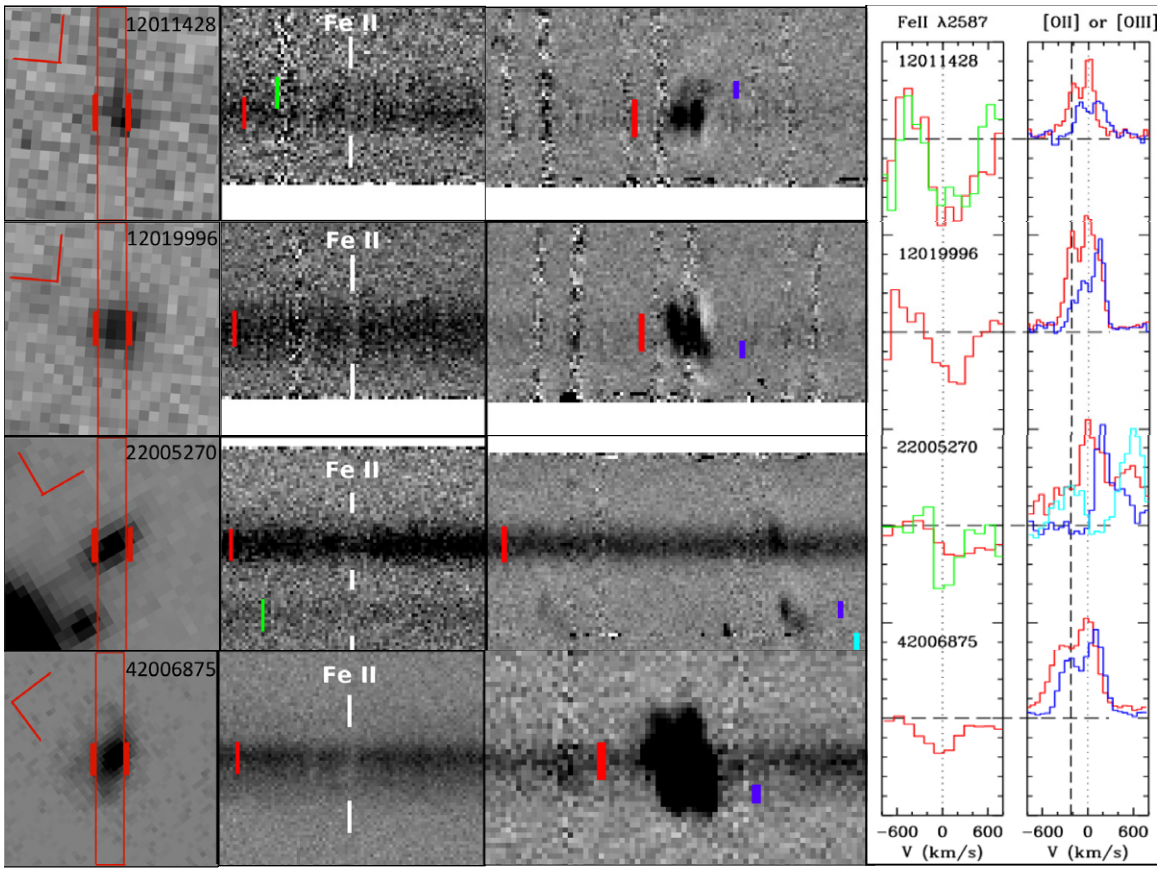

Figure 18. Velocity gradients in the two-dimensional LRIS spectra of inflow galaxies. Column 1: DEEP2 (CFHT, *R*-band) image with the 1″.2 by 9″.0 slitlet and central extraction aperture marked. The compass rose marks north and (90° counterclockwise) east. The slit across 22005270 passes near a galaxy identified as 22005066 in the DEEP2 photometric catalog. Column 2: two-dimensional LRIS spectra near Fe II λ2600 (white tic marks). Wavelength increases from left to right, and the width of the region shown is approximately 183 Å. We denote the central apertures and the apertures used for the off-center spectra shown in Column 4 and Figure 17. Column 3: two-dimensional LRIS spectra near the [O II] λλ3726, 3729 doublet (or, in the case of 22005270, near [O III] λ5007). Wavelength increases from left to right, and the width of the region shown is approximately 81 Å. We mark the central apertures and the off-center apertures where we extracted the emission-line profiles shown in Column 5. the tilt of the emission lines reflects the rotation of dense gas in these galaxies; and a satellite galaxy is clearly detected in the 22005270 spectrum. Columns 4 and 5: extracted spectra zoomed in on the Fe II λ2587 and [O II] (or [O III]) lines. In all four spectra, the gradient in the emission velocity along the slit is as large as the redshift of the Fe II absorption down the barrel (central aperture). The infalling gas detected toward the center of each galaxy has a redshift that matches the Doppler shift of either that galaxy's outer disk or a satellite galaxy.

galaxy and the receding side is as large as the $51 \pm 14\,\mathrm{km\,s^{-1}}$ redshift of the Fe II absorption in the galaxy spectrum. The comparable redshifts of the spatially extended emission and the Fe II absorption toward the center of the galaxy suggest to us that the infalling gas is part of a spatially extended structure, and this structure meets the disk roughly 10 kpc southeast of the galactic center. The Mg II absorption trough exhibits a red wing in the λ2803 consistent with the infalling structure contributing to the line profile.

How do the emission-line kinematics compare to the redshift of the Fe II absorption in the galaxy spectrum in the other five spectra? The two-dimensional spectra of 32020468 and 12100420 do not resolve the line emission spatially. The absence of spatially extended emission is not surprising in light of their compact morphology in ground-based images, and 12100420 also looks compact in an *Hubble Space Telescope* image. Yet, as illustrated in the spectra shown in Figure 16, the Fe II absorption is redshifted $123 \pm 40\,\mathrm{km\,s^{-1}}$ in 32020468 and 71 ± 18 in 12100420. In 12100420, the Mg II absorption also displays a net redshift; but in 32020468, the Mg II absorption is detected a low significance near the systemic velocity. In the remaining three galaxies—12016019, 12019962, and 22004858—the [O II] emission along the slitlets is spatially resolved and very slightly tilted. Despite the small gradient in the velocity of the emission, however, the spectra of these galaxies exhibit significantly redshifted resonance absorption. The Mg II absorption trough also exhibits a net redshift in 22004858. Hence, none of these five spectra show line emission at redshifts near the Fe II absorption redshift. It would be valuable to obtain spectra at other position angles and determine whether or not these galaxies have any extended emission at the redshift of the Fe II absorption as in the case of the four objects in Figure 18.

To summarize, the LRIS spectra cover nebular emission lines in all nine inflow galaxies. We have described the discovery of line emission near the redshift of the Fe II resonance absorption in four of these: 12011428, 12019996, 22005270, and 42006875. Since the velocity of the spatially offset, redshifted emission is comparable to the Doppler shift of the absorption measured directly toward the galaxy, the inflow may mark a spatially extended infalling structure. To assess the probability of a random coincidence in velocity, we also looked for emission features with blueshifts similar to the blueshifted absorption. For 33 of the 35 spectra with 3σ Fe II blueshifts, we could inspect the velocity gradient of the nebular emission along the slit. We found four spectra with extended emission reaching the blueshift of the Fe II absorption and one spectrum with emission

significantly more blueshifted than the Fe II emission. Among the spectra showing outflow detections, the fraction of coincidences between emission and absorption velocities (5 out of 33 spectra) is lower than the fraction of inflow spectra showing extended emission near the velocity of the redshifted absorption (four matches among the nine inflow galaxies). This result supports our suggestion of a physical association between extended disks and satellite galaxies (the source of the spatially extended emission in the inflow spectra) and the redshifted Fe II absorption component. We also note that the absence of nebular emission (anywhere along the slit) at the velocity of the Fe II blueshifts further strengthens our interpretation of those blueshifts as evidence of outflowing gas.

6.3. Properties of Infalling Gas

6.3.1. Which Galaxies Have Infalling Metals?

Of the 208 spectra, nine show very significant (3σ) redshifts of the Fe II absorption relative to the host galaxy. The low fraction of unambiguous inflows appears to be consistent with the six inflows identified recently by Rubin et al. (2012) among approximately 100 objects. Here, we examine the properties of these nine galaxies and their enriched infall. We cannot exclude a higher inflow fraction at lower velocities and less significant equivalent widths; however, the results presented for inflows in Figure 9 indicate not more than 20% of the spectra show inflows with Doppler shifts larger than the systematic error of 41 km s^{-1} in the determination of the systemic velocity.

In the SFR–stellar mass plane shown in Figure 11, the masses of four of these five inflow galaxies fall in the high mass tertile. Given the small number of objects, however, this excess is hardly significant and not supported by the full sample in which four of the nine inflow galaxies have stellar masses less than $\log M/M_{\odot} = 10.20$, the median stellar mass of the LRIS sample. We have only measured the SFRs for five of the galaxies with Fe II redshifts (that lie in the AEGIS field). Three (two) of these five galaxies have specific SFRs lower (higher) than the average shown in Figure 11, and hence inflows do not depend strongly on specific SFR. We found 3/69, 2/68, and 4/71 galaxies with redshifted Fe II absorption, respectively, in the low, middle, and high redshift tertiles of the LRIS sample. In spite of the limited sample size, we therefore conclude that inflow galaxies may sample the full range of SFR, specific SFR, stellar mass, and redshift.

The galaxies with spectra showing redshifted Fe II absorption do not have unusual properties in any way, aside from having infalling gas along the sightline to them. Since the galaxies with detected inflows do not share some physical property, we argue that most galaxies may have inflows and attribute the low incidence of measured redshifts to the geometry of the infalling streams. Specifically, we find 3%–6% sightlines toward $z \sim 1$ galaxies show redshifted Fe II, so the covering fraction of the inflows is quite small.

6.3.2. Velocity

In Table 4, we summarize the inflow speeds fitted to centroids of the Fe II absorption troughs. Except for the extreme case of 22005270, the fitted one-component velocities are less than 200 km s^{-1} and therefore consistent with Rubin et al. (2012). The gas moves at speeds of material bound to galaxies. Evidence for high-velocity gas can be seen in the absorption-line profiles shown in Figures 16–18. The largest inflow velocity is detected via the Mg II absorption trough in 22005270. In the red wings of the Fe II line profiles, absorption at velocities exceeding 600 km s^{-1} is detected in 12016019, 12019962, 12100420, 22004858, 22005270, and 42006875. Modeling the contribution of the ISM via two-component fitting increases the estimated inflow velocity. The median inflow velocity increases from 71 km s^{-1} in the single-component fits to 191 km s^{-1} in the two-component fits.

6.3.3. Inclination

Rubin et al. (2012) found that five of their six inflow galaxies have highly inclined ($i > 55°$), disk-like morphologies. They interpreted the high inclinations as evidence that rotation dominates the kinematics of the infalling gas but pointed out a paradox—i.e., that the absorbing gas must be located on only the receding side of these galaxies. Kornei et al. (2012) show the morphologies of five of the LRIS inflow galaxies. The axis ratio was not well measured for 12011428. The measurements for 12100420, 12019962, and 12019996 indicate $i < 55°$ however, and only 12016019 is consistent with a large inclination of $\sim 61°$. Hence, it remains unclear whether high inclination is a necessary condition for the detection of enriched infall.

6.3.4. Infalling Mass

The (median) equivalent widths of the Fe II λ2374 and 2261 lines suggest the total Fe II column density, ISM plus inflow, typically lies in the range $15.08 \leqslant \log N(\mathrm{Fe}^{+})(\mathrm{cm}^{-2}) \leqslant 15.85$. For purposes of illustration, we conservatively choose solar metallicity gas, no depletion of Fe onto grains, and an ionization fraction of 100% singly ionized iron. The total hydrogen column density is then

$$\log N(\mathrm{H})(\mathrm{cm}^{-2}) \approx 19.58 + (\log N(\mathrm{Fe}^{+}) - 15.08) - \log(Z/Z_{\odot}). \quad (13)$$

The implied column is $\log N(\mathrm{H}) = 19.58$ for solar metallicity infall, but lower metallicities are plausible and raise the inferred hydrogen column.

The galactic ISM clearly produces some of the Fe II equivalent width since our sightline directly intersects a galaxy. Although a true measurement of the inflowing column in ionized iron requires much higher spectral resolution, the potential impact of the ISM on the equivalent width of the inflowing component can be illustrated with two-component fits to the absorption trough as outlined in Section 3.3.2. For the Doppler component fitted to the Fe II absorption, we integrated the equivalent widths of the λ2374 and λ2261 profiles to obtain the lower and upper bounds, respectively, on $N_{\mathrm{Dop}}(\mathrm{Fe}^{+})$ in Table 4. The median bounds provide a very rough estimate of typical inflow column $14.4 \leqslant \log N_{\mathrm{Dop}}(\mathrm{Fe}^{+})C_f \leqslant 15.15$. The total hydrogen column of the infalling column is therefore typically larger than

$$\log N(\mathrm{H})(\mathrm{cm}^{-2}) \approx 18.90 + (\log N(\mathrm{Fe}^{+}) - 14.40) - \log(Z/Z_{\odot}). \quad (14)$$

Gas columns larger than those associated with galactic disks and damped Lyα (DLA) systems, $\log N_{\mathrm{H}}(\mathrm{cm}^{-2}) \approx 20.3$, seem unlikely. Hence, we expect the metallicity of the redshifted gas is greater than roughly 0.04 $Z_{\odot}$.

6.4. Comparison of Inflow Properties to Models

Many properties of the infalling gas are consistent with the cold flow scenario. The velocity components along our

sightlines are largely consistent with virial motion, the exception being the extremely large redshift toward 22005270, which is associated with the satellite galaxy 22005066. The two-dimensional spectra provide spatial information about the inflow in three other objects, and in those the redshift of the infalling gas matches the projected velocity on one side of a rotating, gas disk. This association could reflect a stream crossing in front of each galaxy and connecting to the outer disk in the manner predicted by Stewart et al. (2011a, 2011b). The low incidence of redshifted Fe II absorption in spectra of $z \sim 1$ galaxies would also be expected for cold flows.

To have any chance of detecting a cold flow in a metal line, the sightline must run along the filament (e.g., see Figure 2 in Kimm et al. 2011), and the chance of such a favorable orientation is small. While differences in the radiative-transfer calculations produce some variation in the average covering fraction among these models, galaxies with covering fractions of more than a few percent, as originally suggested by Dekel et al. (2009), are now thought to be quite rare (Kimm et al. 2011). Numerical simulations suggest that only a few percent of the sightlines passing within 100 kpc of a massive galaxy at $z \sim 2$ intersect dense ($\log N_{\rm H}({\rm cm}^{-2}) > 20.3$), infalling gas (Kimm et al. 2011; Faucher-Giguère & Kereš 2011; Fumagalli et al. 2011). It must be acknowledged, however, that these high columns represent the cool gas threading the filaments rather than the smooth component of the cold streams, which dominates the cross section of neutral hydrogen absorption below $\log N_{\rm H\,I}({\rm cm}^{-2}) = 18$ within $R_{\rm vir}$ (Fumagalli et al. 2011). At $z < 2$, less than half the cross section in the range $19 < \log N_{\rm H\,I}({\rm cm}^{-2}) < 20$, and less at higher columns, is likely due to streams (Fumagalli et al. 2011).

Theory predicts the disappearance of cold flows in halos more massive than roughly $10^{12}\,M_\odot$. The halo masses of many of the galaxies in the high stellar mass tertile of the LRIS sample are likely above $10^{12}\,M_\odot$ based on either their clustering properties (Coil et al. 2008) or halo abundance matching (Behroozi et al. 2010). In the LRIS sample, we did not find any change in the inflow fraction with increasing stellar mass; however, this sample excludes red-sequence galaxies. As can be seen by comparing the density of red-sequence and blue-cloud galaxies in Figure 1, the fraction of red galaxies increases quite quickly among galaxies with stellar masses $\log M/M_\odot > 10.3$, the typical stellar mass in a $10^{12}\,M_\odot$ halo at $z \sim 1$ indicated by abundance matching (Behroozi et al. 2010). Whether or not the fraction of inflow galaxies declines with mass in an unbiased sample cannot be determined from our data since we do not measure the inflow fraction toward red galaxies. Likewise, the lack of any evolution with redshift might be limited to blue-cloud galaxies which compose the LRIS sample.

According to some models (Kimm et al. 2011; Fumagalli et al. 2011), detection of the inflows via a metal line definitely implies that these are not cold accretion flows. From our perspective, however, the metallicity of the cold inflows near galaxies remains a highly uncertain quantity in the models due to the unrealistic treatment of metal recycling via galactic winds. The circulation of metals might significantly enrich the cold flows before the infalling gas is incorporated into the galactic disk.

In this recycling scenario, the distinction between cold flows and infalling relic outflows may become blurred. Numerical simulations including outflows have suggested that the covering factor of high column density (DLA-like) gas increases with halo mass, due in large part to the kinematics of outflowing gas (Hong et al. 2010; Faucher-Giguère & Kereš 2011). Given the lack of a strong scaling relation between outflow velocity and stellar mass, we expect a larger fraction of the outflowing material to fall back onto the more massive galaxies. Hence, the recycling of outflows should produce an increasing inflow column as stellar mass increases.

The distinction between the increasing (decreasing) inflow column with stellar mass due to wind recycling (cold flows) may provide a means to discriminate the primary origin of infalling metal-enriched gas. This proposal further emphasizes that inflow fraction measurements should include red-sequence galaxies. Although we expect only star-forming galaxies to drive outflows, the galaxies may migrate across the color–magnitude diagram (due to the cessation of star formation) before the bulk of the outflow slows down and turns around (due to the gravitational attraction of the galaxy). The first inflow galaxies identified appeared to support this scenario; their optical colors placed them on the red sequence, but their UV–optical colors indicated that they were forming stars a few 100 Myr prior (Sato et al. 2009). A subsequent study of 13 K+A galaxies, however, discovered 2 inflow galaxies (Coil et al. 2011) suggesting an inflow fraction similar to our result for blue-cloud galaxies.[17] Finally, mergers also bring gas into galaxies. The association of the galaxy 22005066 with the redshifted Fe II absorption in 22005270 may reflect this scenario. Because 22005066 is the less luminous of the two galaxies, we would expect a tidal stream to pull gas out of 22005066 onto 22005270.

In summary, cold flows, mergers, and wind recycling are all expected to contribute to gas infall. The low incidence of infall suggests that whichever process dominates, the covering fraction of the infalling streams is low. Much larger samples of individual spectra will be needed to further distinguish among these mechanisms on a statistical basis.

7. SUMMARY AND IMPLICATIONS

Our understanding of galaxies will be greatly improved once we understood what controls the flow of matter between galaxies and the circumgalactic medium. Empirical constraints are essential in this regard because there are many physical processes that may be important and these processes can be nonlinear—e.g., the cooling rate or the interplay between mechanical and radiative feedback.

In this paper, we used unusually deep spectroscopy of galaxies at $0.4 < z < 1.4$ to investigate which galaxies have low-ionization outflows. The blue sensitivity of LRIS and collecting power of the Keck I telescope made it possible to detect NUV absorption lines in spectra of individual galaxies. These galaxies are typical blue-cloud galaxies and have higher SFRs than do most galaxies today. We have fit a series of Fe II absorption lines to describe the bulk flow (to within $\pm 40\,{\rm km\,s^{-1}}$) and constrain the Fe II column density (to within an order of magnitude). These Doppler shifts have been compared to the most sensitive tracer of high-velocity gas in the spectra, the Mg II $\lambda\lambda$2796, 2803 doublet, which is frequently detected out to impact parameters of 70 kpc in galaxy halos.

We measure Fe II blueshifts of -50, -100, and $-200\,{\rm km\,s^{-1}}$ or more in spectra of, respectively, 45%, 20%, and 2.5% of blue-cloud galaxies at $z \sim 1$. This outflow fraction is roughly three

[17] The galaxies in our LRIS sample that show redshifted Fe II absorption do not have the spectral signatures of K+A galaxies nor the colors of green-valley galaxies. They are normal blue-cloud galaxies and are not post-starburst galaxies.

times higher in galaxies with $21 < \mathrm{SFR}(M_\odot\,\mathrm{yr}^{-1}) < 98$ than in galaxies with $0.9 < \mathrm{SFR}(M_\odot\,\mathrm{yr}^{-1}) < 10$. Comparing the average spectra of the sample divided at the median SFR, the Fe II absorption is significantly blueshifted ($-38 \pm 8\,\mathrm{km\,s^{-1}}$) in the higher SFR, but not the lower SFR, composite spectrum. Among the individual spectra, however, the correlation between Fe II Doppler shift and SFR, while in the direction of larger blueshifts at higher SFR (Spearman rank-order correlation coefficient $r_S = -0.225$), deviates by only 1.6σ from the null hypothesis of no correlation. We find the most significant outflows in spectra of individual galaxies with specific SFR larger than $0.8\,\mathrm{Gyr}^{-1}$. Galaxies with $1.6 < \mathrm{sSFR}(\mathrm{Gyr}^{-1}) < 5.6$ are roughly five times more likely to show blueshifted Fe II absorption than those with $0.07 < \mathrm{sSFR}(\mathrm{Gyr}^{-1}) < 0.7$. These results for the outflow fraction and outflow velocity confirm the expectation that the blueshifts of the Fe II lines identify outflows powered by massive stars. When combined with the measured cosmic SFR history, they also predict an increase in the fraction of galaxies with blueshifted absorption toward higher redshift. Among just blue galaxies (our LRIS sample), however, we do not detect a statistically significant increase in the blueshifted fraction with redshift.

While we find no variation of Fe II Doppler shift with stellar mass, blue luminosity, or $U-B$ color, the Mg II equivalent width does increase toward higher stellar mass, B-band luminosity, and redder color in both composite and individual spectra. Fitting the ISM absorption explicitly shows that the increase in the Mg II equivalent width can be attributed in part to a stronger interstellar gas component in the more massive galaxies. An associated increase in the dust mass is consistent with the redder color of the more massive galaxies and reduces their emission in resonance lines. This reduction of emission filling in the spectra of massive galaxies (relative to lower mass galaxies) amplifies the positive correlation between the Mg II absorption equivalent width and stellar mass.

We have described gas flows over a range in stellar mass spanning the halo mass floor and mass ceiling required by equilibrium SFR models. As the mass on the red sequence grows with cosmic time, the fraction of massive ($\log M_*/M_\odot \gtrsim 10.3$) galaxies having blue colors decreases. It follows that although we find no change in the outflow properties of blue-cloud galaxies between redshift 0.4 and 1.4, the decline in the fraction of galaxies with blue galaxies may render outflows less prevalent among massive galaxies at lower redshift.

We demonstrate that the fraction of spectra with blueshifted Fe II absorption is much less than 100%. While blueshifted absorption is found more often in spectra of galaxies with high SFRs, particularly high specific SFRs, the blueshifted fraction is remarkably insensitive to galaxy properties overall. We conclude that the detection of blueshifted resonance absorption depends strongly on viewing angle and the outflows must subtend solid angles much less than 4π steradians. This geometry is reminiscent of the bipolar outflows emanating from nearby starbursts (Heckman et al. 1990). Because outflows breakout of the ISM in the direction of least resistance, their collimation indicates the presence and prevalence of gas disks in blue galaxies at $z \sim 1$. The higher rotation speeds of these disks in more massive galaxies may be the physical reason for the higher absorption equivalent widths observed at the systemic velocity in more massive galaxies.

Based on this geometrical consideration, we can describe the typical outflow properties. The de-projected outflow velocity is measured directly when our sightline is parallel to the outflow axis. If most of the galaxies have similar outflow properties, then the largest blueshifts we measure, roughly $200\,\mathrm{km\,s^{-1}}$ (line centroids) and $500\,\mathrm{km\,s^{-1}}$ (Doppler components), characterize the typical outflow speed. Using bounds on the column density of outflowing Fe II, the mass-loss rates in the warm phase are comparable to the average SFR for plausible assumptions about the launch radius, ionization fraction, and depletion. If the outflows persist at the observed rates for $\sim$1 Gyr, then the low-ionization outflows would remove roughly $10^{10}\,M_\odot$ of warm gas, a significant baryonic mass.

The most surprising aspect of this work was the discovery of nine galaxies with robust redshifts of low-ionization metals lines. Since these galaxies do not have unusual properties, inflows of low-ionization gas at velocities up to 100–200 $\mathrm{km\,s^{-1}}$ (based on two-component fits) appear to be a common property of blue galaxies at $z \sim 1$. We do not measure the hydrogen column density of these infalling streams directly; but for metallicities in the range of 1–0.1 $Z_\odot$ the streams would have total hydrogen gas columns of $\log N(\mathrm{H})C_f > 18.9$. At these columns, the inflows subtend a small solid angle and escape detection in all but the largest surveys. We find some evidence that the inflows are kinematically associated with satellite galaxies and extended disks, which if confirmed would help isolate the origin of the infalling gas. The inflows may originate, for example, from tidal forces generated by galaxy interactions or multiphase cooling of hot halo gas. We emphasize that aside from their metallicity, the properties of these inflows are consistent with recent predictions for cold flows of accreting gas. Since future modeling of the mixing between primordial inflow and recycled wind material may well increase the expected metallicity of cold flows within a few tens of kiloparsec of a galaxy, the detection of the infall in metal lines does not obviously rule out a cold flow origin

This research was supported by the National Science Foundation through grants AST-0808161 and AST-1109288 (C.L.M.) and CAREER award AST-1055081 (A.L.C.), the David & Lucile Packard Foundation (A.E.S. and C.L.M.), the Alfred P. Sloan Foundation (A.L.C.), and a Dissertation Year Fellowship at UCLA (K.K.). We are grateful to the DEEP2 and AEGIS teams for providing both the galaxy sample and ancillary data on galaxy properties. We thank Donald Marolf, Andrey Kravtzov, Norman Murray, Dawn Erb, and Nicolas Bouché for discussions that improved this work. The Aspen Center for Physics provided a stimulating environment for completing much of the writing; and this research was partially supported by the National Science Foundation under grant No. NSF PHY05-51164. We also wish to recognize and acknowledge the highly significant cultural role that the summit of Mauna Kea has always had within the indigenous Hawaiian community. It is a privilege to be given the opportunity to conduct observations from this mountain.

Facility: Keck:I (LRIS)

APPENDIX

OUTFLOW FRACTION CALCULATION

As an example of how to calculate the outflow fraction, or more precisely the fraction of spectra with blueshifted resonance absorption, from data, we will use the results of our single-component fitting to the Fe II series of absorption lines. For each spectrum, the fitted Doppler shift, V_1, and its uncertainty, δV_1, provide the best estimate of the distribution of Doppler

shifts (i.e., its mean and standard deviation) which would be obtained after many observations. Equivalently, in the special case of a symmetric probability distribution, we can describe the probability of measuring a Doppler shift V_1 when the true velocity is equal to or past $V_{\rm crit}$.

Let $P_i(V \leqslant V_{\rm crit})$ represent the probability that the absorption lines in a particular spectrum have a Doppler shift bluer than $V_{\rm crit}$. The probability, $P_i(V \leqslant V_{\rm crit})$, is the fractional area of this distribution with Doppler shifts $V \leqslant V_{\rm crit}$. Since this distribution is well described by a Gaussian function of width $\sigma \equiv \delta V_1$ (Section 3.1), we simply compute $P_i(V \leqslant V_{\rm crit})$ from an expression closely related to the normal error integral.

The expression for the entire integral depends on the relation of $V_{\rm crit}$ and V. We adopt a sign convention that outflow velocities are negative. When a spectrum has a low Doppler shift relative to the outflow threshold, $V_{\rm crit} \leqslant V_1$, the chance that the true value of the Doppler shift is faster than $V_{\rm crit}$ is small and given by

$$P_i(V \leqslant V_{\rm crit}|V_1, \delta V_1) = 0.5 - Q. \quad \text{(A1)}$$

When the fitted Doppler shift is bluer than the outflow threshold, $V_{\rm crit} \geqslant V_1$, the chance that the true Doppler shift is faster than $V_{\rm crit}$ is much more significant; and the total integral is

$$P_i(V \leqslant V_{\rm crit}|V_1, \delta V_1) = 0.5 + Q. \quad \text{(A2)}$$

The function

$$Q(t) = \frac{1}{\sqrt{2\pi}} \int_0^t e^{-z^2/2} dz = \frac{1}{2} erf(t) \quad \text{(A3)}$$

describes the integral over a portion of a Gaussian distribution, where we have defined the dimensionless variable t as

$$t \equiv |V_{\rm crit} - V_1|/\delta V_1. \quad \text{(A4)}$$

For each discrete value of the threshold velocity, we compute the outflow fraction by adding the outflow probabilities $P_i(V \leqslant V_{\rm crit})$ of all the spectra. We normalize this sum by the number of spectra $N_{\rm spec}$ to obtain the outflow fraction:

$$P_{\rm out}(V_{\rm crit}) = N_{\rm spec}^{-1} \Sigma_{i=1}^{N_{\rm spec}} P_i(V \leqslant V_{\rm crit}). \quad \text{(A5)}$$

The probability of finding a Doppler shift redder than $V_{\rm crit}$ is $1 - P_{\rm out}$. For positive values of $V_{\rm crit}$, the fraction of spectra with $V > V_{\rm crit}$ obtained from $1 - P_{\rm out}$ describes the frequency of redshifted velocities in the sample.

Error bars are calculated directly from the probability distribution. For a sample of $N_{\rm spec}$ objects, we compute the probability of finding 0, 1, 2, ..., $N_{\rm spec} - 1$, $N_{\rm spec}$ objects with $V \leqslant V_{\rm crit}$. In practice, our code uses a subroutine that starts with the first spectrum in the list, calculates the probability of finding 0 or 1 objects with $V_1 \leqslant V_{\rm crit}$, and then proceeds to calculate probabilities for larger samples in an iterative fashion advancing through lists of 2, 3, 4, ... objects until the probabilities are obtained for the full list of $N_{\rm spec}$ objects. The sum of the first $i + 1$ values in this sequence yields the cumulative probability that the number of outflows with $V_1 \leqslant V_{\rm crit}$ is less than or equal to N_i, where $i = 0$ to $N_{\rm spec}$. The boundaries of the 68.27% confidence interval are found by interpolating between the N_i values to estimate the number of spectra where the cumulative probability that $V_1 \leqslant V_{\rm crit}$ is 0.1587 (lower bound) and 0.8413 (upper bound).

REFERENCES

Aird, J., Coil, A. L., Moustakas, J., et al. 2012, ApJ, 746, 90
Arav, N., Kaastra, J., Kriss, G. A., et al. 2005, ApJ, 620, 665
Behroozi, P. S., Conroy, C., & Wechsler, R. H. 2010, ApJ, 717, 379
Bell, E. F., McIntosh, D. H., Katz, N., & Weinberg, M. D. 2003, ApJS, 149, 289
Bell, E. F., Papovich, C., Wolf, C., et al. 2005, ApJ, 625, 23
Bordoloi, R., Lilly, S. J., Knobel, C., et al. 2011, ApJ, 743, 10
Bouché, N., Dekel, A., Genzel, R., et al. 2010, ApJ, 718, 10001
Bouché, N., Hohensee, W., Vargas, R, et al. 2012, MNRAS, 426, 801
Bouché, N., Murphy, M. T., Proux, C., Csabai, I., & Wild, V. 2006, MNRAS, 371, 495
Brooks, A. M., Governato, F., Quinn, T., Brook, C. B., & Wadsley, J. 2009, ApJ, 694, 396
Bundy, K., Ellis, R. S., Conselice, C. J., et al. 2006, ApJ, 651, 120
Chabrier, G. 2003, PASP, 115, 763
Chen, Y.-M., Tremonti, C. A., Heckman, T. M., et al. 2010, AJ, 140, 445
Chevalier, R. A., & Clegg, A. W. 1985, Nature, 317, 44
Churchill, C., Vogt, S. S., & Charlton, J. C. 2003, AJ, 125, 98
Coil, A. L., Newman, J. A., Croton, D., et al. 2008, ApJ, 672, 153
Coil, A. L., Weiner, B. J., Holz, D. E., et al. 2011, ApJ, 743, 46
Cooper, J., Bicknell, G. V., Sutherland, R. S., & Bland-Hawthorn, J. 2008, ApJ, 674, 157
Cooper, J., Bicknell, G. V., Sutherland, R. S., & Bland-Hawthorn, J. 2009, ApJ, 703, 330
Cresci, G., Hicks, E. K. S., Genzel, R., et al. 2009, ApJ, 697, 115
Davé, R., Finlator, K., & Oppenheimer, B. D. 2011b, MNRAS, 416, 1354
Davé, R., Finlator, K., & Oppenheimer, B. D. 2012, MNRAS, 421, 98
Davé, R., Oppenheimer, B. D., & Finlator, K. 2011a, MNRAS, 415, 11
Davis, M., Faber, S. M., Newman, J., et al. 2003, Proc. SPIE, 4834, 161
Davis, M., Guhathakurta, P., Konidaris, N. P., et al. 2007, ApJ, 660, L1
Dekel, A., & Birnboim, Y. 2006, MNRAS, 368, 2
Dekel, A., Birnboim, Y., Engel, G., et al. 2009, Nature, 457, 451
De Young, D. S., & Heckman, T. M. 1994, ApJ, 431, 598
Drory, N., Salvato, M., Gabasch, A., et al. 2005, ApJ, 619, L131
Elbaz, D., Daddi, E., Le Borgne, D., et al. 2007, A&A, 468, 33
Ellison, S., Songaila, A., Schaye, J., & Pettini, M. 2000, AJ, 120, 1175
Erb, D. K., Quider, A. M., Henry, A. L., & Martin, C. L. 2012, ApJ, 759, 26
Faber, S. M., Willmer, C. N. A., Wolf, C., et al. 2007, ApJ, 665, 265
Faucher-Giguère, C.-A., & Kereš, D. 2011, MNRAS, 412, L118
Fujita, A., Martin, C. L., Mac Low, M.-M., et al. 2009, ApJ, 698, 693
Fumagalli, M., Prochaska, J. X., Kasen, D., et al. 2011, MNRAS, 418, 1796
Goerdt, T., Dekel, A., Sternberg, A., Gnat, O., & Ceverino, D. 2012, MNRAS, 424, 2292
Grimes, J. P., Heckman, T., Aloisi, A., et al. 2009, ApJS, 181, 272
Heckman, T. M. 2002, in ASP Conf. Ser. 254, Extragalactic Gas at Low Redshift, ed. J. S. Mulchaey & J. Stocke (San Francisco, CA: ASP), 292
Heckman, T. M. 2003, RMxAC, 17, 47
Heckman, T. M., Armus, L., & Miley, G. K. 1990, ApJS, 74, 833
Heckman, T. M., Borthakur, S., Overzier, R., et al. 2011, ApJ, 730, 5
Heckman, T. M., Lehnert, M. D., Strickland, D. K., & Armus, L. 2000, ApJS, 129, 493
Hong, S., Katz, N., Davé, R., et al. 2010, arXiv:1008.4242
Hopkins, A. M., & Beacom, J. F. 2006, ApJ, 651, 142
Hopkins, P. F., Quataert, E., & Murray, N. 2012, MNRAS, 421, 3522
Jones, T., Stark, D. P., & Ellis, R. S. 2012, ApJ, 751, 51
Kacprzak, G. G., Churchill, C. W., Evans, J. L., Murphy, M. T., & Steidel, C. C. 2011, MNRAS, 416, 3118
Kereš, D., Katz, N., Davé, R., Fardal, M., & Weinberg, D. H. 2009b, MNRAS, 396, 2332
Kereš, D., Katz, N., Fardal, M., Dave, R., & Weinberg, D. H. 2009a, MNRAS, 395, 160
Kereš, D., Katz, N., Weinberg, D. H., & Davé, R. 2005, MNRAS, 363, 2
Kimm, T., Slyz, A., Devriendt, J., & Pichon, C. 2011, MNRAS, 413, 51
Kobulnicky, H. A., & Gebhardt, K. 2000, AJ, 119, 1608
Kornei, K. A., Shapley, A. E., Martin, C. L., et al. 2012, ApJ, 758, 135
Lilly, S. J., Le Fevre, O., Hammer, F., & Crampton, D. 1996, ApJ, 460, L1
Lu, L. 1991, ApJ, 379, 99
Madau, P., Ferguson, H. C., Dickinson, M. E., et al. 1996, MNRAS, 283, 1388
Marchesini, D., van Dokkum, P. G., Förster Schreiber, N. M., et al. 2009, ApJ, 701, 1765
Marlowe, A., Meurer, G. R., Heckman, T. M., & Schommer, R. 1997, ApJS, 112, 285
Martin, C. L. 1999, ApJ, 513, 156
Martin, C. L. 2005, ApJ, 621, 227
Martin, C. L. 2006, ApJ, 647, 222
Martin, C. L., Kobulnicky, H. A., & Heckman, T. M. 2002, ApJ, 574, 663

Martin, C. L., Scannapieco, E., Ellison, S. L., et al. 2009, ApJ, 721, 174
Martin, C. L., Scannapieco, E., Ellison, S. L., et al. 2010, ApJ, 721, 174
McGaugh, S. S., Schombert, J. M., de Blok, W. J. G., & Zagursky, M. J. 2010, ApJ, 708, 14
Mendez, A. J., Coil, A. L., Lotz, J., et al. 2011, ApJ, 736, 110
Meyer, D. M., & York, D. G. 1987, ApJ, 315, 5
Morton, D. C. 2003, ApJS, 149, 205
Mostek, N., Coil, A. L., Moustakas, J., Salim, S., & Weiner, B. J. 2012, ApJ, 746, 124
Murray, N., Martin, C. L., Quataert, E., & Thompson, T. A. 2007, ApJ, 660, 211
Murray, N., Quataert, E., & Thompson, T. A. 2005, ApJ, 618, 569
Nestor, D., Turnshek, D. A., & Rao, S. M. 2006, ApJ, 643, 75
Newman, J. A., Cooper, M. C., Davis, M., et al. 2012, arXiv:1203.3192
Noeske, K. G., Faber, S. M., Weiner, B. J., et al. 2007a, ApJ, 660, L47
Noeske, K. G., Weiner, B. J., Faber, S. M., et al. 2007b, ApJ, 660, L43
Ocvirk, P., Pichon, C., & Teyssier, R. 2008, MNRAS, 390, 1326
Oke, J. B., et al. 1995, PASP, 107, 375
Oppenheimer, B., Brenner, D., Hinkley, S., et al. 2008, ApJ, 679, 1574
Oppenheimer, B., Davé, R., Kereš, D., et al. 2010, MNRAS, 406, 2325
Pettini, M., Shapley, A. E., Steidel, C. C., et al. 2001, ApJ, 554, 981
Phillips, A. C., Miller, J., Cowley, D., & Wallace, V. 2006, Proc. SPIE, 6269, 56
Press, W. H., Teukolsky, S. A., Vetterling, W. T., & Flannery, B. P. 1992, Numerical Recipes (New York: Press Syndicate of the Cambridge University)
Prochaska, J. X., Kasen, D., & Rubin, K. 2011, ApJ, 734, 24
Rix, H.-W., Guhathakurta, P., Colless, M., & Ing, K. 1997, MNRAS, 285, 779
Rubin, K. H. R., Prochaska, J. X., Koo, D. C., & Phillips, A. C. 2012, ApJ, 747, 26
Rubin, K. H. R., Prochaska, J. X., Koo, D. C., Phillips, A. C., & Weiner, B. J. 2010a, ApJ, 712, 574
Rubin, K. H. R., Prochaska, J. X., Mnard, B., et al. 2011, ApJ, 728, 55
Rubin, K. H. R., Weiner, B. J., Koo, D. C., et al. 2010b, ApJ, 719, 1503
Rupke, D., Veilleux, S., & Sanders, D. B. 2005, ApJS, 160, 115
Sato, T., Martin, C. L., Noeske, K. G., Koo, D. C., & Lotz, J. M. 2009, ApJ, 696, 214
Savage, B. D., & Sembach, K. R. 1996, ARA&A, 34, 279
Schawinski, K., Thomas, D., Sarzi, M., et al. 2007, MNRAS, 382, 1415
Schaye, Y., Aguirre, A., Kim, T.-S., et al. 2003, ApJ, 596, 768
Schwartz, C. M., & Martin, C. L. 2004, ApJ, 610, 201
Schwartz, C. M., Martin, C. L., Chandar, R., et al. 2006, ApJ, 646, 858
Shapley, A. E., Steidel, C. C., Pettini, M., & Adelberger, K. L. 2003, ApJ, 588, 65
Shapley, A. E., Steidel, C. C., Pettini, M., Adelberger, K. L., & Erb, D. K. 2006, ApJ, 651, 688
Simcoe, R. A. 2011, ApJ, 738, 159
Simcoe, R. A., Sargent, W. L. W., Rauch, M., & Becker, G. 2006, ApJ, 637, 648
Somerville, R. S., Hopkins, P. F., Cox, T. J., Robertson, B. E., & Hernquist, L. 2008, MNRAS, 391, 481
Songaila, A., & Cowie, L. L. 1996, AJ, 112, 335
Spitzer, L., Jr. 1978, Physical Processes in the Interstellar Medium (New York: Wiley)
Steidel, C. S., Adelberger, K. L., Shapley, A. E., et al. 2003, ApJ, 592, 728
Steidel, C. S., Erb, D. K., Shapley, A. E., et al. 2010, ApJ, 717, 289
Steidel, C. S., Shapley, A. E., Pettini, M., et al. 2004, ApJ, 604, 534
Stewart, K. R., Kaufmann, T., Bullock, J. S., et al. 2011a, ApJ, 738, 39
Stewart, K. R., Kaufmann, T., Bullock, J. S., et al. 2011b, ApJ, 735, 1
Tremonti, C., Moustakas, J., & Diamond-Stanic, A. M. 2007, ApJ, 663, 77
van de Voort, F., Schaye, J., Booth, C. M., & Dalla Vecchia, C. 2011a, MNRAS, 415, 2782
van de Voort, F., Schaye, J., Booth, C. M., Haas, M. R., & Dalla Vecchia, C. 2011b, MNRAS, 414, 2458
Vázquez, G. A., Leitherer, C., Heckman, T. M., et al. 2004, ApJ, 600, 162
Weiner, B. J., Coil, A. L., Prochaska, J. X., et al. 2009, ApJ, 692, 187
Weiner, B. J., Willmer, C. N. A., Faber, S. M., et al. 2006, ApJ, 653, 1027
Willmer, C. N., Faber, S. M., Koo, D. C., et al. 2006, ApJ, 647, 853
Yan, R., Newman, J. A., Faber, S. M., et al. 2009, MNRAS, 398, 735
Zhang, D., & Thompson, T. A. 2012, MNRAS, 424, 1170